bioRxiv preprint doi: https://doi.org/10.1101/330209; this version posted March 8, 2019. The copyright holder for this preprint (which was not certified by peer review) is the author/funder, who has granted bioRxiv a license to display the preprint in perpetuity. It is made available under aCC-BY-NC-ND 4.0 International license.

The NetrinG1/NGL-1 Axis promotes pancreatic tumorigenesis through cancer associated fibroblast driven nutritional support and immunosuppression

Ralph Francescone[1,8, *], Débora Barbosa Vendramini-Costa[1,8, *], Janusz Franco-Barraza[1,8], Jessica Wagner[2], Alexander Muir[9], Allison N. Lau[9], Linara Gabitova[2,8], Tatiana Pazina[3], Sapna Gupta[1], Tiffany Luong[1,8], Neelima Shah[1,8], Dustin Rollins[1], Ruchi Malik[1,8], Roshan Thapa[3], Diana Restifo[2,8], Yan Zhou[2,4], Kathy Q. Cai[1,5], Harvey H. Hensley[2,6], Yinfei Tan[1,7], Warren D. Kruger[1], Karthik Devarajan[4], Siddharth Balachandran[3], Wafik S. El-Deiry[2], Matthew G. Vander Heiden[9,10], Suraj Peri[4], Kerry S. Campbell[3,8], Igor Astsaturov[2,8], Edna Cukierman[1,8, +]

[1]Cancer Biology Program
[2]Molecular Therapeutics Program
[3]Blood Cell and Development and Function Program
[4]Bioinformatics and Bioinformatics Facility
[5]Histopatholgy Facility
[6]Small Animal Imaging Facility
[7]Genomics
[8]Marvin and Concetta Greenberg Pancreatic Cancer Institute
Institute for Cancer Research, Fox Chase Cancer Center, 333 Cottman Avenue, Philadelphia, PA, 19111, USA
[9]Koch Institute for Integrative Cancer Research and the Department of Biology, Massachusetts Institute of Technology, Cambridge MA, 02139, USA
[10]Dana-Farber Cancer Institute, Boston, MA, 02115, USA
*These authors contributed equally
[+]Correspondence: edna.cukierman@fccc.edu (ORCID 0000-0002-1452-9576)

Summary

Pancreatic ductal adenocarcinoma (PDAC) has a poor 5-year survival rate and lacks effective therapeutics. Therefore, it is of paramount importance to identify new targets. Using multi-plex data from patient tissue, three-dimensional co-culturing *in vitro* assays, and orthotopic murine models, we identified Netrin G1 (NetG1) and Netrin G1 ligand (NGL-1) as promoters of PDAC tumorigenesis. NetG1$^+$ cancer-associated fibroblasts (CAFs) supported PDAC survival, through a NetG1/NGL-1 mediated effect on glutamate/glutamine metabolism. NetG1$^+$ CAFs were intrinsically immunosuppressive and inhibited NK cell mediated killing of tumor cells. These functions were partially mediated by vesicular glutamate transporter 1 and glutamine synthetase. This study uncovered a link between CAF driven metabolism and its immunosuppressive capacity, suggesting NetG1 and NGL-1 as potential targets in PDAC.

Keywords

Cancer associated fibroblasts; Netrin G1; Netrin G1 ligand; pancreatic cancer; tumor microenvironment; extracellular matrix; glutamate; natural killer (NK) cells; metabolism; immunosuppression.

bioRxiv preprint doi: https://doi.org/10.1101/330209; this version posted March 8, 2019. The copyright holder for this preprint (which was not certified by peer review) is the author/funder, who has granted bioRxiv a license to display the preprint in perpetuity. It is made available under aCC-BY-NC-ND 4.0 International license.

Significance

PDAC is a devastating disease lacking effective therapies. A major hallmark of PDAC is desmoplasia, characterized by the expansion of CAFs and their extracellular matrix, creating a unique microenvironment that limits blood-supplied nutrition and is highly immunosuppressive. Nevertheless, the role of CAFs in PDAC is incompletely understood and new targets in PDAC are needed. Here, we uncovered two potential targets, NetG1 in CAFs and its binding partner NGL-1 in tumor cells. NetG1 in CAFs was important for the metabolic support of PDAC cells and for the intrinsic immunosuppressive capacity of CAFs, while NGL-1 in PDAC cells drove tumorigenesis. Our results helped clarify the role that CAFs play in PDAC, by defining CAF phenotypes through NetG1 expression. Finally, we established a link between CAF driven metabolism and their intrinsic immunosuppressive capacity. Thus, NetG1/NGL-1 axis drove cell reciprocal and cell autonomous functions in PDAC, representing new attractive targets for this aggressive disease.

Introduction

Pancreatic cancer is projected to become the 2nd leading cause of cancer related deaths by 2030 (Rahib et al., 2014), due to its abysmal 5 year survival rate (Siegel et al., 2019). The most common form of pancreatic cancer is pancreatic ductal adenocarcinoma (PDAC), to which treatments are often refractory, and where symptoms only appear in advanced stages of the disease (Ryan et al., 2014), making few patients eligible for surgical interventions (Hidalgo, 2010). Therefore, there is an urgent need to develop new diagnostic and better therapeutic approaches.

PDAC has a unique microenvironment that consists of a fibrous expansion reaction known as desmoplasia, characterized by the deposition of an abundant extracellular matrix (ECM) by cancer associated fibroblasts (CAFs). Studies have demonstrated that CAFs limit the efficacy of chemotherapies (Chan et al., 2016; McCarroll et al., 2014; Olive et al., 2009), promote PDAC progression (Djurec et al., 2018; Hwang et al., 2008), and correlate with poor prognosis (Erkan et al., 2008). While there is a clear role for CAFs in facilitating PDAC progression, there is also evidence that CAFs can be tumor restrictive, as complete ablation of fibroblasts from the tumor microenvironment accelerated PDAC progression (Özdemir BC, 2014; Rhim et al., 2014) and provided no added patient benefit (Kim et al., 2014). Thus, the role of CAFs in PDAC development and progression is incompletely understood.

An important consequence of desmoplasia is the generation of substantial interstitial pressure that contributes to the collapse of blood vessels (Provenzano et al., 2012), resulting in a nutrient deprived (Kamphorst et al., 2015) and hypoxic microenvironment (Erkan et al., 2016). Further, *Kras* driven cancers like PDAC, where ~90% of tumors have mutant *Kras*, have been suggested to become “addicted” to exogenous sources of glutamine as a main carbon supply (Son et al., 2013). As such, PDAC cells have been shown to exploit some metabolic pathways to promote their growth and survival (Jin et al., 2016; Seo et al., 2016; Son et al., 2013) and CAFs have emerged as a potential source of nutrients for PDAC cells (von Ahrens et al., 2017), taking advantage of CAF driven metabolic support (Lyssiotis and Kimmelman, 2017). Therefore, further exploration of these mechanisms, aiming to disrupt tumor-stromal crosstalk, is warranted.

bioRxiv preprint doi: https://doi.org/10.1101/330209; this version posted March 8, 2019. The copyright holder for this preprint (which was not certified by peer review) is the author/funder, who has granted bioRxiv a license to display the preprint in perpetuity. It is made available under aCC-BY-NC-ND 4.0 International license.

In addition to the metabolic roles, CAFs are also at the center of the immunosuppressive PDAC microenvironment (Basso et al., 2014; Clark et al., 2007; Fu et al., 2018; Harper and Sainson, 2014). CAFs exert immunosuppressive effects through direct modulation of immune cell function via cytokine secretion (Wu et al., 2017), exclusion of anti-tumor immune cells from the tumor (Ene-Obong et al., 2013), and/or recruitment of immunosuppressive immune cells to the tumor (Kumar et al., 2017). Intriguingly, recent studies have reported a functional link between metabolism and immune cell function, which has suggested that anti-tumor immune cells rely on a constant supply of nutrients to perform their functions (Buck et al., 2017; Kouidhi et al., 2018). In the cancer context, key metabolites—glucose, arginine, glutamine, and tryptophan—are depleted, with a concomitant increase of immunosuppressive waste products, such as lactate, inhibiting anti-tumor immune cell function (Buck et al., 2017; Gardiner and Finlay, 2017; Renner et al., 2017). In PDAC, the immunosuppressive environment created by CAFs, combined with the nutrient poor milieu, create the hostile environment that inhibits anti-tumor immune cell function. Thus, means to simultaneously revert these linked features of the PDAC microenvironment would be therapeutically beneficial.

In this study we sought to clarify the roles of CAFs in PDAC tumorigenesis. We uncovered up-regulation of the glutamatergic pre-synaptic protein, Netrin G1 (NetG1) (Nakashiba et al., 2000; Song et al., 2013), in CAFs. Surprisingly, we also found up-regulation of Netrin G1 Ligand (NGL-1), the post-synaptic binding partner of NetG1 (Lin et al., 2003) in PDAC cells, and that both NetG1 and NGL-1 were overexpressed in PDAC human tissue compared to samples from normal human pancreas. We demonstrated that the NetG1/NGL-1 axis stimulates CAF-PDAC cell interactions, facilitates nutrient flow from CAFs to PDAC cells, and prevents anti-tumor NK cells from eliminating PDAC cells. Deletion of NetG1 in CAFs simultaneously decreased glutamate/glutamine (Glu/Gln) and cytokine release by CAFs, in a mechanism involving glutamine synthetase (GS) and vesicular glutamate transporter 1 (VGlut1). Finally, in orthotopic mouse models, deletion of NGL-1 in murine PDAC cells resulted in lower tumor incidence and stunted tumor growth *in vivo*. Our findings unveil a previously undiscovered axis in PDAC that define tumor cell autonomous and non-autonomous roles for NetG1/NGL-1 in tumor development, as well as offer novel stromal and tumoral targets aiming to reverse the tumor promoting effects of CAFs in the PDAC microenvironment.

Results

Netrin G1 is upregulated in CAFs compared to patient matched normal pancreatic stellate cells.

To gain insight into the mechanism by which pancreatic stellate cells (PSCs) are activated into cancer associated fibroblasts (CAFs), we performed a transcriptomic analysis comparing two sets of patient matched PSCs and CAFs. Interestingly, we observed upregulation of several neural related genes in CAFs, including a top hit, Netrin G1 (NetG1), a synapse stabilizing protein involved in axonal communication (**Fig 1A).** To identify the underlying molecular pathways and biological processes, we performed Gene Set Enrichment Analysis (GSEA) and identified significant enrichment (Benjamini-Hochberg False Discovery Rate < 0.25) of several pathways previously found to be associated with the transition from PSCs to CAFs, including upregulation of integrin signaling, focal adhesions, actin cytoskeleton, and extracellular matrix (ECM) organization (**Fig 1B, C**). Additionally, we observed positive enrichment of pathways associated

bioRxiv preprint doi: https://doi.org/10.1101/330209; this version posted March 8, 2019. The copyright holder for this preprint (which was not certified by peer review) is the author/funder, who has granted bioRxiv a license to display the preprint in perpetuity. It is made available under aCC-BY-NC-ND 4.0 International license.

with axon guidance and neurite outgrowth, where NetG1 was among those upregulated in CAFs (**Fig 1A-C**). We also noticed in CAFs a negative enrichment of pathways associated with antigen presentation (KEGG Systemic Lupus Erythematosus; FDR < .25, Normalized Enrichment Score -2.66) and interferon signaling (Reactome Interferon Signaling; FDR < .25; NES = -2.66) (**Fig 1D**). Overall, this transcriptomic data confirmed that our CAFs did indeed upregulate known pathways previously linked to fibroblast activation in cancer, as well as unveil a novel association with neuronal gene expression.

NetG1 is upregulated in CAFs, and its binding partner NGL-1 is expressed in tumor cells.

NetG1 is present on pre-synaptic neurons, and it stabilizes excitatory glutamatergic synapses by interacting with its only known binding partner on post-synaptic cells, Netrin G1 Ligand (NGL-1) (Lin et al., 2003; Song et al., 2013). To assess the clinical relevance of NetG1/NGL-1, we performed Simultaneous Multichannel Immunofluorescence (SMI) (Franco-Barraza et al., 2017) on 6 normal, 4 tumor adjacent and 15 tumor pancreatic tissue samples to discern NetG1 and NGL-1 expression patterns in distinct subsets of cells. NetG1 was upregulated in the stromal compartment (pan-cytokeratin$^-$/Epcam$^-$, vimentin$^+$ areas) in tumor tissue compared to tumor adjacent normal tissue and normal pancreatic tissue from individuals without cancer (**Fig 2A, B**). Moreover, stromal tyrosine 397 phosphorylated focal adhesion kinase (pFAK) expression followed a similar pattern of increased expression in tumor tissue compared to normal and tumor adjacent normal tissue, in line with our established pro-tumor CAF signature (Franco-Barraza et al., 2017). We also observed a strong correlation between stromal NetG1 expression and stromal pFAK expression in all tissues combined (R^2 = 0.8046, P< 0.0001) (**Fig 2C**). Interestingly, NGL-1 was upregulated in the epithelial compartment (pan-cytokeratin$^+$/Epcam$^+$) of both tumor adjacent and tumor tissue (**Fig 2A, B**), but there was a weak correlation between stromal NetG1 and epithelial NGL-1 expressions in all tissues combined (R^2 = 0.2359, P< 0.0001) (**Fig 2C**), suggesting that having ectopic expression of NetG1 and NGL-1 may be more important than the levels of these proteins in the tumor. Comparing 4 PSCs and 5 CAFs isolated from patient tissue, we confirmed that CAFs upregulated NetG1 protein expression (~2.5 fold increase) (**Fig 2D**). Additionally, we observed the expression of NGL-1 in 5 patient derived cell lines from PDX models (**Fig 2E**), as well upregulated expression in tumor cell lines derived from an isogenic cell line model, hTERT-HPNE E6/E7 (referred to as E6/E7) and hTERT-HPNE E6/E7/K-RasG12D (referred to as PDACc), compared to their immortalized epithelial cell counterpart (hTERT-HPNE; referred to as hTERT) (Campbell et al., 2007) (**Fig 2F**). Collectively, NetG1 and its binding partner NGL-1 were upregulated in cancer compared to normal tissue in the pancreas, and segregated into distinct cellular compartments (stromal vs. epithelial).

Using the cBioportal database (Cerami et al., 2012; Gao et al., 2013), we queried both NetG1 (*NTNG1)* and NGL-1 (*LRRC4C*) mRNA expression across 31 cancer types and found that PDAC was among the highest expressors of both *NTNG1* and *LRRC4C* (**S1A)**. Additionally, we stratified *NTNG1* and *LRRC4C* by clinical subtype according to three independent datasets (Moffitt et al., 2015; Puleo et al., 2018); (TCGA, (Cancer Genome Atlas Research Network. Electronic address and Cancer Genome Atlas Research, 2017)) (**S1B-D**). We found that there was a trend towards elevated *NTNG1* and *LRRC4C* in the basal classification in two out of three datasets, and the basal subtype tends to have the worst prognosis of all PDAC subtypes (Moffitt et al., 2015). Thus, taken together with our observation that stromal NetG1 and epithelial NGL-1 are upregulated in

bioRxiv preprint doi: https://doi.org/10.1101/330209; this version posted March 8, 2019. The copyright holder for this preprint (which was not certified by peer review) is the author/funder, who has granted bioRxiv a license to display the preprint in perpetuity. It is made available under aCC-BY-NC-ND 4.0 International license.

PDAC tissue, the data suggested that NetG1 and NGL-1 may play a pro-tumorigenic role in PDAC.

Ablation of NetG1 does not influence myofibroblastic features of CAFs, but reverses pro-tumorigenic CAF traits

We next sought to understand the function of NetG1 in CAFs, using our well-established cell-derived extracellular matrix (CDM) based 3D culturing system for fibroblasts, which simulates the PDAC microenvironment (Amatangelo et al., 2005; Cukierman et al., 2001; Franco-Barraza et al., 2017), referred to as "3D" for simplicity. Interestingly, NetG1 protein expression in CAFs was significantly elevated in 3D compared to 2D culturing conditions (**S2A**). In order to characterize NetG1 expression during ECM production, one of our patient-derived CAF lines was chosen, in which NetG1 was upregulated at the mRNA and protein levels compared to patient matched tumor adjacent normal PSCs (referred to as PSCs) **(Fig 2D, S2B)**. Next, we followed NetG1 expression during ECM production *in vitro*, a major function of CAFs in the *in vivo* tumor microenvironment. NetG1 expression was maintained throughout ECM production (**S2C**). To better understand the functional role of NetG1, we performed CRISPR mediated deletion of NetG1 in CAFs (**S2D**) and assessed their desmoplastic phenotype during ECM production, according to our previous study (Franco-Barraza et al., 2017). Interestingly, NetG1 knockout (KO) CAFs did not have an altered ECM production or topography, as determined by fibronectin alignment and levels/localization of alpha smooth muscle actin, a marker of myofibroblastic activation (**S2E, F**). However, NetG1 KO CAFs displayed reduced levels of active $\alpha_5\beta_1$ integrin and pFAK, indicative of a CAF phenotype that correlated with delayed recurrence following surgery in PDAC patients (**S2G, H**) (Franco-Barraza et al., 2017), consistent with the correlation seen in human tissue samples (**Fig 2C**). Thus, deletion of NetG1 does not alter myofibroblastic features of CAFs, but reverses known pro-tumor CAF markers.

NetG1 increase heterotypic cell contacts between CAFs and PDAC cells

Because of NetG1's known role in cell-cell adhesion in the brain, namely through its binding partner NGL-1, we next knocked out NGL-1 in PDACc (**S2I)** to test the potential function of NetG1/NGL-1 in CAF-PDAC cell-cell interactions. Interestingly, ablation of NetG1 in CAFs reduced cell engagement with control (CON) or NGL-1 KO PDACc by 72% and 79%, respectively (identified by the yellow regions resulted from the interaction between GFP+ CAFs and RFP+ PDACc) (**S3A-C)**. Accordingly, CON or NGL-1 KO PDACc had increased motility (81% and 74%, respectively) when co-cultured with NetG1 KO CAFs in 3D (**S3D, E**). Unexpectedly, deletion of NGL-1 from PDACc was not sufficient to alter PDACc-CAF cell engagement or PDACc motility, signifying that NetG1 in CAFs is the driver of PDAC-CAF heterotypic interactions and that there may be a redundant mechanism controlling PDAC-CAF engagement in the absence of NGL-1 in tumor cells.

CAFs transfer material to PDAC cells, in a NetG1/NGL-1 dependent manner

Because NetG1 in CAFs mediated PDAC-CAF interactions, we questioned if there was a further functional consequence of the increased heterotypic cell-cell interactions observed during co-culture. Since PDAC cells have been suggested to use numerous extracellular macromolecules as a source of energy (Kamphorst et al., 2015; Muranen et al., 2017), and receive nutrients from

bioRxiv preprint doi: https://doi.org/10.1101/330209; this version posted March 8, 2019. The copyright holder for this preprint (which was not certified by peer review) is the author/funder, who has granted bioRxiv a license to display the preprint in perpetuity. It is made available under aCC-BY-NC-ND 4.0 International license.

CAFs (Sousa et al., 2016; Zhao et al., 2016), we hypothesized that CAFs may provide resources to PDAC cells in a NetG1 dependent manner. To test this, we followed the exchange of GFP from GFP^+ CAFs and RFP from RFP^+ PDACc. Indeed, after 36 hours of co-culture, GFP was detected intracellularly in PDACc (**S3F**), demonstrating that PDACc received CAF derived material. Knockout of NetG1 in CAFs, or NGL-1 in PDACc, resulted in a 49%-61% reduction in GFP transfer to PDACc, compared to CON PDACc/CON CAF group (**S3G**). Therefore, while NGL-1 was dispensable for CAF-PDAC engagement (**S3A-B**), both NGL-1 and NetG1 were necessary for the ability of PDACc to receive material from CAFs, and for CAFs to provide material to PDACc, respectively.

NetG1/NGL-1 Axis Protects PDAC cells from death under nutrient restriction

Since the PDAC microenvironment contains limited nutrients and CAFs can transfer material in a NetG1/NGL-1 dependent manner (**S3**), we hypothesized that CAFs serve as a critical nutrient conduit and could rescue PDAC cells from nutrient deprivation. To this end, we co-cultured GFP^+ CAFs with RFP^+ PDACc in 3D under serum free/Gln free conditions and measured the survival of RFP^+ PDACc over a 4 day time span. We observed that disruption of the NetG1/NGL-1 axis, by deletion of either NetG1 in CAFs or NGL-1 in PDAC cells, resulted in 30-37% decrease in PDACc survival, compared to CON PDACc/CON CAF group, similar to PDACc cultured alone (**Fig 3A**). These results were replicated using the pancreatic cancer cell line PANC-1, with a 40-59% reduction in PANC-1 survival compared to CON/CON group (**Fig 3B**). To determine if CAF secreted factors alone were important for tumor cell survival, PDACc were cultured in 3D with conditioned media (CM) obtained from CON and NetG1 KO CAFs. We found that NetG1 KO CAF CM was 76-82% less efficient at supporting PDACc survival when compared to CON CAF CM, similarly to the CM from PSCs (81-83% of CON CM) (**Fig 3C**). To further assess the effect of NetG1 on the microenvironment generated by CAFs, we performed survival assays using ECMs produced by CON and NetG1 KO CAFs, and compared them to the ECM produced by PSCs, which express less NetG1 than CAFs (**Fig 3D**). Accordingly, the microenvironment generated by NetG1 KO CAFs was less supportive compared to the CON ECM, with a 30% decrease in PDACc survival. The PSC ECM was even less supportive, resulting in a decrease in PDACc survival of 65%. Collectively, these results suggest that both direct physical contact with CAFs, and the factors secreted by CAFs, including their CM and ECM, support PDAC survival in a NetG1/NGL-1 dependent fashion.

Alterations in Glutamate/Glutamine generation in NetG1 KO CAFs reduce PDAC cell survival

In an effort to gain insight into key factors that could be supporting PDAC survival under nutritional deprivation, we performed an amino acid screen comparing PSCs, CON CAFs, and NetG1 KO CAFs, during ECM production (**Sup. Tables 1-3**). The greatest net change in amino acid secretion between PSCs and CAFs was found to be in Glu and Gln, as CAFs secreted 2-fold more of these amino acids (**Fig 3E**). These results are in line with recent studies that suggest that the catabolism of Glu plays a role in PDAC and other cancers (Jin et al., 2016; Son et al., 2013; Xiang et al., 2015; Yang et al., 2016). Strikingly, we found that NetG1 KO CAF CM contained 64% less Glu and 81% less Gln, compared to CON CAFs (**Fig 3E**). In order to determine the relative contributions of Glu and Gln to PDAC survival conferred by CON CAFs CM, we performed a Glu/Gln rescue assay, where the amounts of Glu/Gln produced by CON CAFs (150 µM and 25

bioRxiv preprint doi: https://doi.org/10.1101/330209; this version posted March 8, 2019. The copyright holder for this preprint (which was not certified by peer review) is the author/funder, who has granted bioRxiv a license to display the preprint in perpetuity. It is made available under aCC-BY-NC-ND 4.0 International license.

µM respectively) were added to the depleted media and compared to the rescue provided by CON CAFs CM. Interestingly, while Glu or Gln alone or in combination promoted 40%, 49% or 55% more survival compared to deprived media alone, CON CAFs CM increased CON PDACc survival by 2.5 fold, indicating that there are additional factors in the CM, besides Glu and Gln, contributing to PDAC survival (**Fig 3F**). Importantly, Glu/Gln were not able to rescue NGL-1 KO PDACc survival, suggesting a potential defect in Glu/Gln utilization in PDAC cells lacking NGL-1 (**Fig 3F**). The later results suggested the possibility that NGL-1 could also have cell autonomous functions in PDAC cells.

To check if changes in the mRNA expression of NGL-1 in PDAC cells was associated with differences molecular pathways that regulate nutrient homeostasis and other cellular systems, we compared TCGA cases with high and low NGL-1 expressors. We found gene signatures and processes including those associated, glutamate receptor binding, synaptic assembly, and EMT (**S4**), supporting our *in vitro* results.

Guided by the clear differences in Glu/Gln levels upon KO of NetG1 in CAFs, we explored if glutaminase (GLS) and glutamine synthetase (GS) protein levels were altered in these cells. We detected expression of GLS and GS in PSCs and CAFs (**Fig 4A**). While GLS levels were generally higher in CON and NetG1 KO CAFs than PSCs, GS was significantly reduced in NetG1 KO CAFs, suggesting that NetG1 KO CAFs are compromised in their ability to produce Gln from Glu. Interestingly, NetG1 KO CAFs had reduced levels of VGlut1, a major protein responsible for loading presynaptic vesicles with Glu during neuronal communication (Liguz-Lecznar and Skangiel-Kramska, 2007) (**Fig 4A**). Thus, while CON and NetG1 KO CAFs expressed similar levels of GLS, NetG1 KO CAFs displayed decreased levels of VGlut1 and GS, which could account for the reduced amounts of Gln produced and Glu released by NetG1 KO CAFs. As expected from KRAS mutant cells, PDACc expressed lower levels of GS compared to CON CAFs, while maintaining GLS expression (**Fig 4B**). Interestingly, knockout of NGL-1 in PDACc resulted in a reduction in GLS protein levels, suggesting an even greater metabolic dependence on CAFs or extracellular nutrients in the KO cells compared to CON PDACc. Collectively, these results suggest that Gln and Glu derived from CAFs help support PDAC survival in nutrient deprived conditions, and that this support depends on NetG1 expression in CAFs. Additionally, NGL-1 expression in PDAC cells appears to be critical for the utilization of some extracellular factors, such as Glu and Glu, akin to downregulation of glutamate receptor binding pathways, as suggested by TCGA NGL-1 stratification (**S4**). Thus, modulation of the NetG1/NGL-1 axis disrupts the flux of Gln and Glu from CAFs to tumor cells, thereby affecting their survival.

GS and VGlut1 inhibition in CAFs leads to a decrease in PDAC survival, in a manner similar to NetG1 ablation.

The decreased expression of GS and VGlut1 in NetG1 KO CAFs suggest that these proteins are downstream of NetG1 signaling. In order to evaluate if the absence of VGlut1 in CAFs could phenocopy the effects of NetG1 KO in CAFs, we produced knockdowns for VGlut1 (VGlut1 KD) using CRISPRi technology (**Fig 4C**). We also generated NetG1 KDs CAFs to be able to compare them to VGlut1 KDs with the same control CAFs (**S5A**). Once again, we confirmed the decreased expression of VGlut1 in NetG1 KD CAFs (**S5A**), and verified that NetG1 KD CAFs phenocopied NetG1 KO CAFs in terms of GLS and GS expression (**S5A**), as well as in the effect upon PDACc survival (**S5B**). VGlut1 KD CAFs also displayed reduced expression of GLS and GS (**Fig 4C**).

bioRxiv preprint doi: https://doi.org/10.1101/330209; this version posted March 8, 2019. The copyright holder for this preprint (which was not certified by peer review) is the author/funder, who has granted bioRxiv a license to display the preprint in perpetuity. It is made available under aCC-BY-NC-ND 4.0 International license.

Interestingly, VGlut1 KD CAFs lost the expression of NetG1, suggesting a co-regulatory mechanism for these two proteins. Corroborating this hypothesis, VGlut1 KD CAFs produced similar amounts of Glu and Gln compared to NetG1 KD CAFs, both producing significantly less Glu/Gln than CON CAFs (**Fig 4D, Sup Table 4**). Functionally, VGlut1 KD CAFs had a similar effect on PDACc survival as NetG1 KD CAFs, with PDACc survival reduced by ~50% compared to CON CAFs (**Fig 4E**). To address the contribution of GS to the support provided by CAFs for PDACc survival, we pharmacologically inhibited GS in CAFs, using increasing concentrations of methionine sulfoximine (MSO). MSO efficiently inhibited GS expression at concentrations greater than 0.1 mM (**S5C**). NetG1 expression was also affected, with significant loss of expression when CAFs were treated with 1, 2.5, or 5 mM MSO (**S5C**). Interestingly, using lower concentrations of MSO led to upregulation of VGlut1 expression, but this expression was lost at higher concentrations (2.5 and 5 mM). To address the effect of GS inhibition in CAFs on PDACc survival, CON or NetG1 KO CAFs were pre-treated for 24 hours with 1 mM MSO and then co-cultured with CON or NGL-1 KO PDACc. Inhibition of GS in CAFs resulted in a modest decrease in PDACc survival, with a negligible effect when pre-treated NetG1 KO CAFs were cultured with NGL-1 KO PDACc. (**Fig 4F**). Overall, the data illustrate that blockade of NetG1, similarly to loss of potential downstream proteins VGlut1 and GS, result in a disruption of Glu/Gln generation, as well as a significant reduction in PDAC survival.

Knockout of NetG1 in CAFs reverts their immunosuppressive phenotype and permits NK cell anti-tumor function

Thus far, we noticed that NetG1 expression in CAFs was critical for their pro-tumor functions, including modulation of CAF-PDAC interactions that resulted in a transfer of nutrients to PDAC cells. This led us to question if NetG1 was also a functional mediator of immunosuppression, another key feature of pro-tumorigenic effects of CAFs in cancer. Hence, we performed both traditional and multiplex (U-Plex) enzyme-linked immunosorbent assays (ELISAs) to identify a cytokine profile that could define the immunosuppressive milieu that CAFs generate. We found that CON CAFs produce increased levels of GM-CSF, IL-1β, IL-8, CCL20/MIP3α and TGF-β compared to PSCs (**Fig 5A**). Strikingly, ablation of NetG1 in CAFs significantly decreased protein levels of GM-CSF (40.6 fold), IL-1β (5.2 fold), IL-8 (13.3 fold), CCL20/MIP3α (80 fold), IL-6 (1.4 fold) and TGF-β (1.5 fold) compared to CON CAFs (**Fig 5A**), with a similar downregulation in NetG1 KD CAFs (**S6**). On the other hand, expression of IL-2, IL-12 p70, IL-10, IFN-γ, TNF-α, and IFN-β were all below the limit of detection in all three fibroblastic populations tested (data not shown). Interestingly, we observed that IL-15 protein levels, one of the most potent NK cell activators, was up-regulated in both CON and NetG1 KO CAFs compared to PSCs (4 and 2.9 fold, respectively; **Fig 5A**). This suggested that NetG1 KO CAFs may generate a less immunosuppressive microenvironment than the one from CON CAFs, which could allow NK cells to more effectively kill PDAC cells. To test this, we first assayed the activation of an NK cell line, NK-92, in our *in vitro* 3D culturing system. After IL-2 treatment alone, 68.5% and 72.3% of the NK cells became positive for IFNγ and Granzyme B (i.e. activated), respectively (**Fig 5B**). Conversely, direct co-culture of activated NK cells with CON CAFs or with CM from CON CAFs abolished NK cell activation marker expression, illustrating the potent immunosuppressive potential of CON CAFs. NetG1 KO CAFs, however, were less immunosuppressive, as 12-23% of NK cells maintained IFNγ or Granzyme B expression. This result is consistent with the decreased levels of immunosuppressive cytokines generated by the NetG1 KO CAFs (**Fig 5A**). A similar experiment was performed using primary NK cells isolated from healthy human donor blood, with

bioRxiv preprint doi: https://doi.org/10.1101/330209; this version posted March 8, 2019. The copyright holder for this preprint (which was not certified by peer review) is the author/funder, who has granted bioRxiv a license to display the preprint in perpetuity. It is made available under aCC-BY-NC-ND 4.0 International license.

IFNγ and CD69 as markers of activation. As with NK-92 cells, we observed that while CM from CON CAFs inactivates primary NK cells in a concentration dependent manner (i.e. 10% CM prevented NK activation by ~50%), NetG1 KO CAF CM was significantly less immunosuppressive at the same dilutions (**Fig 5C**). We next tested if the activation status of NK-92 cells correlated with their functional ability to kill PDAC cells. To this end, we performed an experiment co-culturing resting and active NK cells with CON or NGL-1 KO RFP^+ PDACc, in complete media. Accordingly, active NK cells were twice as effective in killing both CON and NGL-1 KO PDACc than resting NK cells (**S7A, B**). To probe how CAFs could directly affect the ability of NK cells to kill PDACc, we co-cultured CON or NetG1 KO CAFs with CON or NGL-1 KO RFP^+ PDACc in the presence of resting or active NK cells, using complete media. In agreement with the observed immunosuppressive profile of CON CAFs (**Fig 5A, B**), active NK-92 cells were prevented from killing PDACc in the presence of CON CAFs, and this protection was decreased by 38-39% when cultured with NetG1 KO CAFs, independently of NGL-1 status (**Fig 5D, S7A**). Intriguingly, even when resting NK cells were in the presence of NetG1 KO CAFs, they were 45-65% more effective at eliminating PDACc compared to co-culture with CON CAFs, suggesting that NetG1 KO CAFs could partially activate NK-92 cells (**Fig 5E, S7A**).

The NK-92 killing assay was replicated in 2D culturing conditions with PDACc or PANC-1 cells, and results were very similar to 3D conditions, as the KO of NetG1 in CAFs resulted in a significant decrease in CON PDACc or CON PANC-1 survival against NK cell induced death compared to CON CAF conditions (84 and 66% less, respectively) (**S7C, D**). Also, the partial activation of NK cells by NetG1 KO CAFs was reproduced in 2D (**S7E**). Interestingly, in 2D conditions, NGL-1 KO cells (KO1 and KO2) were more sensitive to NK cell killing even when co-cultured with CON CAFs (88% and 78% less survival compared to CON PDACc, respectively), suggesting that NetG1/NGL-1 heterotypic cell-cell contacts were important for protection against NK cell induced death in the absence of ECM (**S7C**). Importantly, neither resting nor active NK cells affect CON or NetG1 KO CAFs survival (**S7F**). To question whether tumor to stromal cell ratios are important for the observed effect, we co-cultured various ratios of PDACc to CAFs (5:1, 3:1, 1:3) and again performed the NK cell killing assay. As the number of CAFs increased, PDACc survival increased as well, indicating a direct effect of CAF numbers on NK cell killing function (**S7G**).

Overall, NetG1 expression in CAFs creates an immunosuppressive microenvironment that inactivates NK cells and protects PDAC cells from NK cell mediated death. Loss of NetG1 expression in CAFs partially reverts the immunosuppressive capacity of CAFs, allowing NK cells to maintain their activity and eliminate PDAC cells. Moreover, the microenvironment created by CAFs (ECM) plays an important role in the support of PDAC survival, highlighting the differential effects of 2D culture versus 3D culture.

IL-15 expression maintains functionality of NK cells in NetG1 KO CAF microenvironment

While deletion of NetG1 in CAFs led to a decrease in the expression of immunosuppressive cytokines, IL-15 levels remained significantly higher than that of PSCs (**Fig 5A**). We hypothesized that the downregulation of immunosuppressive cytokines, coupled with the maintenance of IL-15 expression, was partially responsible for the observed anti-tumor phenotype of the NetG1 KO CAFs. Thus, we repeated the NK cell killing assay in 2D and 3D, co-culturing CON or NetG1 KO CAFs with CON or NGL-1 KO PDACc, in the presence of a neutralizing IL-15 antibody or IgG isotype control. Indeed, neutralization of IL-15 resulted in a 1.4 and 0.4 fold (2D and 3D,

bioRxiv preprint doi: https://doi.org/10.1101/330209; this version posted March 8, 2019. The copyright holder for this preprint (which was not certified by peer review) is the author/funder, who has granted bioRxiv a license to display the preprint in perpetuity. It is made available under aCC-BY-NC-ND 4.0 International license.

respectively) increase in PDACc survival compared to IgG treated conditions, suggesting that IL-15 was partially responsible for the anti-tumor microenvironment created by NetG1 KO CAFs (**Fig 6A, B**).

VGlut1 and GS contribute to CAF regulated NK cell immunosuppression

Driven by the fact that the KD of VGlut1 and the inhibition of GS in CAFs phenocopied the absence of NetG1 in terms of support to PDAC survival, we questioned if these CAF proteins could also be involved in the observed NK cell immunosuppression. In fact, the ablation of either VGlut1 or GS in CAFs also led to a significant decrease in the production of GM-CSF and TGF-β compared to CON CAFs (**Fig 6C, D**). Interestingly, while VGlut1 KD reduced IL-6 levels, GS inhibition in CAFs increased IL-6 secretion at nearly all doses of MSO, suggesting that these cytokines are regulated differently. Importantly, the production of IL-15 was maintained in these cells, suggesting that VGlut1 and GS might also be important for the inhibitory effects of CAFs in the functionality of NK cells. Corroborating this hypothesis, in the NK killing assay, VGlut1 KD and GS inhibited CAFs were able to partially revert the inhibitory effect conferred by CON CAFs (35 and 25% more PDACc death compared to CON CAF condition, respectively), demonstrating a similar effect as the NetG1 KO CAFs (**Fig 6E, F**). These data suggest that NetG1, VGlut1 and GS may be linked in a signaling circuit in CAFs, being important not only for the immunosuppressive profile of these cells, but also for the metabolic support provided to PDAC cells.

Loss of NGL-1 from murine PDAC cells severely stunts tumorigenesis *in vivo*

We next tested whether disruption of NetG1/NGL-1 axis would prevent/delay tumor progression *in vivo*. First, we explored NetG1 expression in the stroma of LSL-Kras$^{G12D/+}$; Pdx-1-Cre (KC) mice, which readily develop precancerous lesions known as PanINs (Pancreatic Intraepithelial Neoplasia) and eventually full blown invasive PDAC (Hingorani et al., 2003). Using SMI, we observed that as the KC mice age and develop PanINs, stromal NetG1 expression was detected in pancreatic tissue as early as 12 weeks and at 16 weeks, while absent in non-tumor bearing mice (**Fig 7A**). Moreover, we generated two murine PDAC cell lines, isolated and cloned from the more aggressive LSL-KRAS^{G12D};TP53$^{-/-}$;PDX1-Cre (KPC) model (Hingorani et al., 2005), one with low NGL-1 expression that resulted in an average survival time of 7.5 weeks after orthotopic injection into C57BL/6 mice (KPC4B), and one with high expression of NGL-1 that resulted in an average survival time of 3.5 weeks after orthotopic injection (KPC3) (**Fig 7B**). These data indicated that NetG1/NGL-1 axis, with stromal expression of NetG1 and tumoral expression of NGL-1, is intact in mice, and that this axis may play a role *in vivo*. Using CRISPR/Cas9, we generated two NGL-1 KO murine PDAC cell lines and one control line from the aggressive KPC3 cells (**S8A**) and injected them orthotopically into C57BL/6 mice (CON, KO1, KO2). Mice injected with CON KPC3 cells (CON group) had a tumor incidence of 100% (7/7) with a mean pancreas weight of 1371 ± 262.1 mg after 3 weeks, while the groups injected with NGL-1 KO1 and KO2 KPC3 cells (NGL-1 KO group) had an incidence of 22.2% (2/9) and 40% (4/10) with a mean pancreas weight of 174.4 ± 45.3 mg and 311 ± 81.5 mg, respectively (**Fig 7C**). In addition, representative MRI images reveal the expansion of the pancreas in CON group over 3 weeks, while the pancreas from the NGL-1 KO group seemingly remains a normal size over that time span (**Fig 7D**). Analyzing the pancreatic tissue further, an average of 69% of CON group pancreata were composed of tumor areas, while only 16% of the NGL-1 KO group pancreata contained tumor cells (**S8B**). Because only 6 animals developed tumors between the two groups

bioRxiv preprint doi: https://doi.org/10.1101/330209; this version posted March 8, 2019. The copyright holder for this preprint (which was not certified by peer review) is the author/funder, who has granted bioRxiv a license to display the preprint in perpetuity. It is made available under aCC-BY-NC-ND 4.0 International license.

injected with NGL-1 KO clones, we performed the following analyses pooling both NGL-1 KO groups. Of the 6 pancreata that presented tumors in the KO groups, an average of 51% of the area was considered tumor, compared to an average of 69% in the CON group (**S8B-D**). Moreover, tumors from the KO group had a trend towards being more differentiated than those from the CON group, as an average of 79% of the cells from CON tumors were classified as poorly differentiated, while only 48% of the cells from KO tumors could be classified as poorly differentiated (**S8E-F**), indicative of less aggressive tumors overall. Consequently, NGL-1 KO tumors also proliferated slower, as measured by Ki67 staining, and had higher rates of apoptosis, as measured by TUNEL staining (**Fig 7E**). These results were in line with less Ki67 staining in human NGL-1 KO PDACc compared to CON PDACc *in vitro* (**S2J**). Therefore, we postulated that similarly to the *in vitro* conditions, disruption of the interaction between tumoral NGL-1 and stromal NetG1 (herein by knocking out NGL-1) lead to a reduction in stromal metabolic support for tumor cells. In order to evaluate the impact of the immune system, orthotopic injections of CON or NGL-1 KO KPC3 cells into SCID (lacks T and B cells) and Nod SCID Gamma (NSG; lacks T, B, and NK cells) mice were performed and compared to immunocompetent mice (B6). All animals injected with CON cells presented more tumors than those injected with NGL-1 KO cells, independently of the immune backgrounds (**S8G**). These results reinforce the idea that when NGL-1 is lacking in tumor cells, and the NetG1^{+} stroma remains intact, the likely cause for stunted tumorigenesis in this context is due to two factors: 1.) lack of CAF derived metabolic support of PDAC cells; 2.) cell intrinsic effects on the tumor cells without NGL-1 expression (slower proliferation, less uptake of nutrients). Therefore, inhibition of one arm of the NetG1/NGL-1 axis was sufficient to dramatically impede tumor initiation and progression.

RNAseq analysis reveals that ablation of NetG1 in CAFs results in a normalized expression signature

Our *in vitro* and *in vivo* results demonstrated that the key functional hallmarks of CAFs could be reverted towards a more normalized state upon KO of NetG1. To this end, we performed RNAseq analysis comparing CON CAFs to NetG1 KO CAFs to gain insight into global changes in gene expression. Pathway and gene enrichment analysis identified downregulation of genes associated with many critical pathways that we saw upregulated in CAFs in our microarray analysis (**Fig 1**), including: axon guidance, focal adhesion, ECM and TGF-β signaling, and inflammatory responses (**Fig 8A-C**). NetG1 KO CAFs displayed an upregulation of genes associated with histidine, tryptophan, and fatty acid metabolism (**Fig 8A**), which combined with the results from the amino acid screen, suggests a metabolic reprogramming of CAFs lacking NetG1. All in all, the RNAseq analysis confirmed, at the gene expression level, that deletion of NetG1 causes reversion of genes associated with pathways that confer pro-tumorigenic CAF traits.

Discussion

The present study has uncovered two previously unknown targets for the potential treatment of pancreatic cancer: the neural glutamatergic synaptic stabilizing proteins NetG1 and NGL-1 (Matsukawa et al., 2014). Here, we demonstrated the up-regulation of these proteins in different cell compartments in patient tissue, as well as their importance in governing key hallmarks of PDAC *in vitro* and in mouse models. NetG1 overexpression was evident in CAFs and dependent on CAF generated ECMs, while NGL-1 was upregulated in PDAC cells, and the ectopic

bioRxiv preprint doi: https://doi.org/10.1101/330209; this version posted March 8, 2019. The copyright holder for this preprint (which was not certified by peer review) is the author/funder, who has granted bioRxiv a license to display the preprint in perpetuity. It is made available under aCC-BY-NC-ND 4.0 International license.

expression of these proteins drove heterotypic cellular interactions, resulting in pro-tumorigenic support from CAFs to PDAC cells that promotes survival in nutrient deprived conditions. Interestingly, we found NetG1 and NGL-1 have cell autonomous functions as well. For example, ablation of NetG1 in CAFs caused a decrease in cytokine production, an alteration of Glu/Gln secretion, and a reversion to a tumor restrictive CAF phenotype. Further, NGL-1 KO in PDAC cells resulted in reduced proliferative capacity *in vitro* and the diminished ability to utilize nutrients from their environment. Importantly, orthotopically injected NGL-1 KO murine PDAC cells had a dramatically reduced tumorigenicity, demonstrating the importance of this axis *in vivo*. Thus, our data have revealed a complex signaling axis that controls heterotypic CAF-PDAC interactions, as well as cell intrinsic capabilities, that shapes the tumor microenvironment.

CAFs are a major cell type present in the PDAC microenvironment, whose role is incompletely understood. This study aimed to characterize the functions of NetG1/NGL-1 in the PDAC microenvironment, with an emphasis on the contribution of the stroma. CAFs regulate three critical hallmarks of PDAC: 1.) the deposition of ECM; 2.) overcoming nutrient deprivation; and 3.) vast immunosuppression of anti-tumor immune cells (Fu et al., 2018; Ryan et al., 2014). Our results confirm that all three hallmarks are interconnected, and that NetG1 expression in CAFs is a central driver of the PDAC microenvironment.

The PDAC microenvironment is nutrient deprived, due to the collapse of blood vessels enabled by desmoplasia, and this forces PDAC cells to seek out alternative sources of fuel (Kamphorst et al., 2015). CAFs represent a potential source of nutrients in PDAC, as they can account for up to 90% of the tumor mass (Ricci et al., 2005). Recent studies have demonstrated that CAFs supply PDAC cells with important metabolites, through exosomes (Zhao et al., 2016) and amino acid secretion (Sousa et al., 2016). Moreover, the ECM has been shown to be an important source of fuel for cancer cells (Muranen et al., 2017), which potentially positions the scaffolding produced by CAFs in the PDAC microenvironment as a vital source of fuel for PDAC cells. Here, we found that NetG1^{+} CAFs exchange material with PDAC cells and that this exchange is dependent upon NetG1 expression in CAFs and NGL-1 expression in PDAC cells (**S3**). Additionally, we observed that CAFs lacking NetG1 were less supportive of PDAC survival, in direct co-culture, with their CM, or ECM (**Fig 3**). These findings prompted us to perform a screen comparing amino acid production and secretion and revealed a NetG1 dependent increase in extracellular Glu/Gln in CAFs (**Fig 3E**).

Interestingly, it has long been recognized that patients with pancreatic cancer have elevated serum levels of Glu (Castro-Bello et al., 1976), with a corresponding depletion of serum Gln levels (Roux et al., 2017). PDAC cells have a high capacity to utilize Glu, by catabolizing Gln through the enzyme glutaminase (GLS), in a process known as glutaminolysis (Lyssiotis and Kimmelman, 2017). While it is known that inhibition of GLS can decrease cancer cell growth *in vitro* and *in vivo* in a number of cancer models (Jin et al., 2016; Xiang et al., 2015), a recent study using a potent small molecular inhibitor of GLS displayed little efficacy in preclinical mouse models, in part through up-regulation of compensatory Gln procuring pathways in PDAC cells (Biancur et al., 2017). Additionally, it has also been demonstrated that the conditions used in cell culture provide an overabundance of nutrients that does not accurately mimic the tumor microenvironment *in vivo*, and culturing cells in a medium with nutrients at levels more representative of tumors *in vivo* resulted in tumor cells with a decreased dependence on Gln, due to increased utilization of cystine (Muir et al., 2017). Our findings that CAFs can overcome tumor specific targeting therapies by

bioRxiv preprint doi: https://doi.org/10.1101/330209; this version posted March 8, 2019. The copyright holder for this preprint (which was not certified by peer review) is the author/funder, who has granted bioRxiv a license to display the preprint in perpetuity. It is made available under aCC-BY-NC-ND 4.0 International license.

supplying key Glu/Gln metabolites to PDAC cells adds to the ways in which cancer cells in PDAC can acquire glutamine in tumors.

Our results demonstrated that ablation of NetG1 in CAFs reduced GS (catalyzing conversion of Glu to Gln), but not GLS protein levels (**Fig 4A**). Indeed, GS is up-regulated in CAFs in ovarian cancer compared to their normal counterparts, and inhibition of stromal GS resulted in decreased tumor development (Yang et al., 2016). Additionally, we found that deletion of NGL-1 from PDAC cells resulted in a decrease in GLS expression (**Fig 4B**), signifying an even greater dependence of these cells on the microenvironment. Functionally, while exogenous Glu/Gln could partially rescue NGL-1^{+} PDAC cell survival from metabolic stress, the same was not true for NGL-1 KO PDAC cells, as Glu/Gln had no effect on cell survival under the same serum/Gln free conditions (**Fig 3F**). Similarly, CAF CM media only modestly rescued NGL-1 KO PDAC cell survival, while significantly improving cell survival in PDAC cells expressing NGL-1, suggesting that NGL-1 may more broadly control cellular uptake of metabolites in PDAC cells. An additional interpretation of the data could be that CAF driven metabolism of Glu/Gln is required to first process these amino acids into other metabolites that are used by NGL-1 deficient PDAC cells. Accordingly, our results obtained from the TCGA cases stratified by NGL-1 expression revealed an association between NGL-1 expression and glutamate receptor binding (**S4**). Further analysis into the expression and activity of receptors that mediate uptake of extracellular amino acids in PDAC, such as Glu/Gln, as well as TCA cycle metabolites produced by CAFs, will be necessary to gain more insight into the general uptake ability of PDAC cells.

We also observed a dramatically reduced expression of VGlut1 upon NetG1 loss in CAFs (**Fig 4A**). Interestingly, VGlut1 is present in glutamatergic synapses in neurons, where it loads Glu into vesicles (Liguz-Lecznar and Skangiel-Kramska, 2007), and VGlut1 expression in neurons was shown to be dependent on NetG1 expression (Song et al., 2013). These studies are in line with our data in CAFs, where the KO of NetG1 resulted in downregulation of VGlut1 expression, and provide a potential mechanistic explanation for the decreased levels of Glu in NetG1 KO CAF CM (**Fig 3E**). Accordingly, in our study, VGlut1 KD CAF CM displayed reduced Glu/Gln levels, as well as reduced NetG1 and GS protein expression, and this translated into reduced PDAC survival in serum/Gln free conditions (**Fig 4 B-E**). Interestingly, VGlut1, 2 and 3 have been implicated in pancreatic neuroendocrine tumors (PNET), and Glu signaling in PNET tumor cells drove tumorigenesis (Li and Hanahan, 2013). Finally, GS inhibition in CAFs resulted in decreased NetG1 expression (**S5C**), as well as decreased PDAC cell survival in co-culture under serum/Gln free conditions (**Fig 4F**). Overall, our results reveal a complex metabolic crosstalk between CAFs and PDAC cells that is, in part, regulated via NetG1 and NGL-1.

Another hallmark of PDAC tumors is an extremely immunosuppressive microenvironment. Numerous studies have confirmed a major role for CAFs in generating factors, such as secreted cytokines and chemokines (Harper and Sainson, 2014; Wu et al., 2017), that contribute to this environment, as well as physically sequestering anti-tumor immune cells (Ene-Obong et al., 2013). Furthermore, compared to many other tumor types, PDAC has one of the lowest mutational burdens and display of neoantigens (Chalmers et al., 2017; Evans et al., 2016), which correlates directly with low response rates to immune checkpoint inhibitors, such as PD-1 (Yarchoan et al., 2017). Collectively, these findings suggest that even if cytotoxic T-cells could penetrate the tumor and CAF driven immunosuppression was inhibited, the lack of tumor antigens would render them unable to kill PDAC cells effectively. However, the innate cytotoxic immune cell population—

bioRxiv preprint doi: https://doi.org/10.1101/330209; this version posted March 8, 2019. The copyright holder for this preprint (which was not certified by peer review) is the author/funder, who has granted bioRxiv a license to display the preprint in perpetuity. It is made available under aCC-BY-NC-ND 4.0 International license.

natural killer (NK) cells—can destroy PDAC cells independent of neoantigen presentation, and thus represents an attractive anti-tumor cell type for PDAC therapy (Van Audenaerde et al., 2018). Additionally, NK cells play a natural role in the pancreas which is to remove activated stromal cells during acute fibrosis in wound healing by a process known as nemosis (Vaheri et al., 2009), but are unable to accomplish this in the setting of PDAC, due to the overwhelming numbers of CAFs and immunosuppressive signals, resulting in a situation akin to unresolved chronic wound healing (Heneberg, 2016; Vaheri et al., 2009). Thus, reverting the immunosuppressive phenotype of CAFs could allow for NK cell stimulating therapies (e.g. IL-15 supplementation) (Van Audenaerde et al., 2017) to more efficiently clear CAFs and PDAC cells. In the present work, we confirmed that CAFs produce the immunosuppressive cytokines TGF-β and GM-CSF, which can expand immunosuppressive myeloid cells (Takeuchi et al., 2015; Trotta et al., 2008), as well as chemokines known to attract immunosuppressive immune cells (IL-8 and CCL20) (**Fig 5A**). Intriguingly, we showed that CAFs, compared to normal PSCs, upregulate IL-15, a potent stimulator of NK cell activity. Functionally, however, IL-15 activity is likely overwhelmed by the greater number of immunosuppressive factors secreted by CAFs, especially TGF-β, as CAFs significantly inhibited NK cell activation and function. In our study, NetG1 KO CAFs exhibited reduced levels of all immunosuppressive factors tested, compared to CON CAFs, while maintaining IL-15 expression (**Fig 5A**). This may account for the shift towards a profile that would likely allow IL-15 to stimulate NK cell activation, survival, and killing of PDAC cells. Indeed, we saw that NK cells co-cultured with NetG1 KO CAFs or their CM, remained partially activated, and could kill PDAC cells more efficiently than NK cells co-cultured with NetG1+ CAFs (**Fig 5B-E, S7**). Furthermore, we demonstrated that in fact, IL-15 was partially responsible for the NetG1 KO CAFs enabling NK cell killing ability, as neutralizing antibodies against IL-15 restored protection against NK cell induced death (**Fig. 6A, B**). In this context, unlike the metabolic stress experiments, NGL-1 status on PDAC cells had nearly no effect on NK cell ability to kill PDAC cells in 3D. In 2D, however, NGL-1 expression on PDAC was critical for CAF mediated protection of PDAC cells from NK cell induced death, illustrating the importance of ECM effects in the PDAC microenvironment. Moreover, it is interesting to note that our NK cell killing assays could be completed in 6-8 hours in 2D conditions, while 48 hours was required to complete assays performed in 3D, again highlighting the importance of ECM protective effects that are more representative of the *in vivo* situation, where the time scales are increased (Deguine et al., 2010). Collectively, the data demonstrate that NetG1 in CAFs shapes the immunosuppressive microenvironment in PDAC, and its ablation reprograms CAFs to an anti-tumor phenotype allowing NK cells to eliminate cancer cells.

In recent years, there has been growing interest in linking microenvironmental metabolites with immune cell function (Buck et al., 2017), and CAFs in the PDAC microenvironment are important players in this process (Lyssiotis and Kimmelman, 2017). For example, CAF derived prostaglandin E2 (PGE2), an immunomodulatory lipid, has been shown to inhibit NK cell anti-tumor function in a number of models (Balsamo et al., 2009; Li et al., 2012; Li et al., 2013). Thus, we postulated that CAF metabolism, driven by NetG1, and by extension, VGlut1 and GS, could be partially responsible for the immunosuppressive phenotype of CAFs. Importantly, we saw a significant decrease in amounts of immunosuppressive cytokines in the CM of VGlut1 KD or GS inhibited CAFs (**Fig 6C, D**), akin to CM from NetG1 KO CAFs. Furthermore, both VGlut1 KD and GS inhibited CAFs had a functional effect on NK cells, as PDAC cell survival was significantly decreased in the NK cell elimination assay (**Fig 6E, F**). Our results demonstrate a link between a metabolic circuit, NetG1-VGlut1-GS, and suppression of anti-tumor immunity. Taking lessons

bioRxiv preprint doi: https://doi.org/10.1101/330209; this version posted March 8, 2019. The copyright holder for this preprint (which was not certified by peer review) is the author/funder, who has granted bioRxiv a license to display the preprint in perpetuity. It is made available under aCC-BY-NC-ND 4.0 International license.

from the brain and synaptic biology, it is known that cytokines, such as TNF-α, IFN-γ, IL-6, TGF-β, and IL1-β regulate glutamatergic synaptic activity and subsequently Glu release and uptake by neurons and astrocytes (Galic et al., 2012; Haroon et al., 2017; Vesce et al., 2007). Our data suggests that a reciprocal signaling mechanism may exist in CAFs, whereby disruption of synaptic proteins like NetG1 and VGlut1 result in modulation of cytokine secretion from CAFs (**Fig 6C**), and Glu/Gln cycling may also play a role, as GS inhibition also affected cytokine secretion in CAFs (**Fig 6D**). In sum, our findings illustrate that simply modulating NetG1 expression in CAFs can simultaneously "disarm" two major pro-tumorigenic features of CAFs: metabolic support of PDAC cells and protection from immune cell killing. These data suggest that synaptic biology in CAFs might be the missing link that controls metabolic and immunosuppressive programs in pancreatic cancer.

We further showed that not only the disruption of NetG1/NGL-1 axis by targeting NetG1 in CAFs was important, but also the ablation of the other arm of the axis, NGL-1, in PDAC cells, affected tumorigenesis in murine orthotopic models of PDAC. We saw that deletion of NGL-1 in two distinct clones of murine PDAC cells resulted in significantly decreased tumor incidence and aggressiveness of tumors (**Fig 7, S8**). This led us to postulate that the diminished tumorigenicity of the NGL-1 KO cells was likely due to their inability to accept nutrients from CAFs (NetG1/NGL-1 connection broken) or scavenge extracellular material (lower uptake of GFP from material transfer assay), and not due to the modulation of CAFs directly. Thus, we anticipated that there would be no changes in immunosuppression in the tumors that form. Indeed, injection of murine PDAC cells into immunocompromised mice did not alter the course of disease compared to immunocompetent mice (**S8G**), supporting our hypothesis that the disruption of metabolic aspect of the NetG1/NGL-1 axis was primarily responsible for the decrease in tumorigenesis, when NGL-1 is absent in tumor cells. Thus, by modulating only one arm of the NetG1/NGL-1 axis, we could dramatically stunt tumorigenesis *in vivo*. Taken together, however, our results suggest that tumor development may be significantly reduced by therapeutic antibodies or small molecules targeting stromal NetG1 that can both suppress a major metabolic support mechanism and enhance anti-tumor immune responses within the PDAC microenvironment.

A major question in the field is what role do CAFs play in PDAC tumorigenesis? Several studies have demonstrated that CAFs are tumor promoting (Djurec et al., 2018; Hwang et al., 2008), while others have suggested tumor restrictive roles (Özdemir BC, 2014; Rhim et al., 2014). One possible explanation for the seemingly paradoxical findings is that not all CAFs are created equally, as it is now appreciated that there is great heterogeneity in the fibroblastic population within the tumor microenvironment (Ohlund et al., 2014). Recent studies have revealed multiple CAF subsets in a variety of tumors (Costa et al., 2018; Costea et al., 2013; Franco-Barraza et al., 2017; Moffitt et al., 2015; Ohlund et al., 2017), each with different functions. Our group has identified two distinct CAF subsets in PDAC that are predictive of patient outcome (Franco-Barraza et al., 2017). We now propose that NetG1 expression in CAFs stratifies PDAC associated CAFs into two major subtypes: Class 1 (***C1)*** anti-tumor (**NetG1 low/negative CAFs, with low pFAK, GS, and VGlut**) and Class 2 (***C2***) pro-tumor (**NetG1 positive CAFs, maintaining high pFAK, GS, and VGlut1**). ***C2*** CAFs functionally support PDAC cell survival and shield them from NK cell induced death, while ***C1*** CAFs fail to provide metabolic or immunosuppressive support, independent of myofibroblastic features (**Fig 8D**). These findings help explain how CAFs can be tumor restrictive in some settings, while tumor promoting in others, highlighting the need to fully characterize CAF populations (markers and function) in order to develop more effective

bioRxiv preprint doi: https://doi.org/10.1101/330209; this version posted March 8, 2019. The copyright holder for this preprint (which was not certified by peer review) is the author/funder, who has granted bioRxiv a license to display the preprint in perpetuity. It is made available under aCC-BY-NC-ND 4.0 International license.

therapeutics. For example, systemic pFAK inhibition in a variant of the KPC mouse model, was shown to revert the desmoplastic phenotype of tumors, including immunosuppression, which improved immunotherapeutic responses (Jiang et al., 2016), in agreement with our results.

Overall, we have identified two new potential therapeutic targets, NetG1 and NGL-1, for treating pancreatic cancer, for which there are no effective therapeutic interventions. Additionally, we have characterized two phenotypes of CAFs, the anti-tumor ***C1*** and the pro-tumor ***C2***, and by targeting NetG1 in CAFs, we can revert C2 CAFs back into tumor restrictive C1 CAFs. Thus, we offer not only a tumor cell target, but a stromal target as well, whereby ablation of this new signaling axis affects cell intrinsic properties that promote tumorigenesis, but also disrupts tumor-stroma crosstalk that is essential for PDAC tumor development and support. This work will hopefully open the door for mechanistic studies into NetG1/NGL-1 mediated signaling that will potentially generate novel therapeutics.

STAR Methods

Reproducibility: Key Resources Table

All information (manufacturer/source, RRID, website) regarding key antibodies, mouse models, chemical and biological reagents, software, and instruments has been compiled into a master "Key Resources" Table.

Cell Culture

The PDAC cells used for the majority of the assays, termed "PDACc" in this study (Campbell et al., 2007), were maintained in media containing 1 part M3 Base F (INCELL, San Antonio, TX) to 4 parts Dulbeco Modified Eagle Medium (DMEM) low glucose (1 g/mL) + sodium pyruvate 110 mg/mL + 1% Penicillin-Streptomycin (10,000 U/mL; Thermo Fisher Scientific, Waltham, MA), supplemented with 5% fetal bovine serum (Atlanta Biologicals, Flowery Branch, GA). PANC-1 cells were maintained in DMEM supplemented with 5% FBS and 1% penicillin-streptomycin (P/S) (10,000 U/mL). Patient matched tumor adjacent PSCs and CAFs (Franco-Barraza et al., 2017) were maintained in DMEM containing 15% FBS, 1% P/S, and 4 mM glutamine. For individual experiments, cells were cultured as described in the figure legends or methods, either with the maintenance conditions outlined above, or in DMEM without serum (serum free), or DMEM without serum and without glutamine (-). NK-92 cells were maintained in Alpha Minimum Essential medium without ribonucleosides and deoxyribonucleosides supplemented with the following components: 2 mM L-glutamine, 1.5 g/L sodium bicarbonate, 0.2 mM inositol, 0.1 mM 2-mercaptoethanol, 0.02 mM folic acid, 400 units/mL IL-2, 12.5% horse serum and 12.5% fetal bovine serum.

Isolation and immortalization of patient derived fibroblasts

Fresh patient pancreatic tissue collected after surgery was digested enzymatically, using our established protocol (Franco-Barraza et al., 2016). Briefly, tissue was initially stored in PBS with antibiotics (P/S, Fungizone) Next, tissue was physically minced with a sterile scalpel, and was digested overnight in collagenase (2mg/mL). After a series of filtration and centrifugation steps, cells were plated on gelatin coated plates for subsequent expansion. Cells were characterized as done previously (Amatangelo et al., 2005; Franco-Barraza et al., 2017), and fibroblasts were confirmed by a lack of cytokeratins, expression of vimentin, cell shape, ability to create

bioRxiv preprint doi: https://doi.org/10.1101/330209; this version posted March 8, 2019. The copyright holder for this preprint (which was not certified by peer review) is the author/funder, who has granted bioRxiv a license to display the preprint in perpetuity. It is made available under aCC-BY-NC-ND 4.0 International license.

substantive ECM, and the presence of lipid droplets (tumor adjacent PSCs) or acquisition of lipid droplets after TGF-β signaling inhibition (CAFs). For the immortalization, cells were retrovirally transduced as previously described (Franco-Barraza et al., 2017), with the pBABE-neo-hTERT vector, which was a gift from Dr. Robert Weinberg (Addgene plasmid # 1774).

Generation of Patient Derived PDAC cell lines from patient derived xenographs (PDX)

Procedure was performed with an approved protocol from Fox Chase Cancer Center Institutional Review Board and was done as previously described (Beglyarova et al., 2016). Briefly, tumor fragments were obtained after surgery and washed in RPMI media. The washed fragments were then resuspended in 1:1 mixture of RPMI and Matrigel on ice and were implanted subcutaneously into 5-8 week old *C-B17.scid* mice (Taconic Bioscience). Once tumors developed to a size of at least 150 mm^3, but no larger than 1,500 mm^3, mice were sacrificed, and the tumors were collected. These tumors were then digested with a solution containing collagenase/hyaluronidase, and dispase (StemCell Technologies, Cambridge, MA). After several washes, dissociated PDX cells were plated in DMEM supplemented with 10% FBS, 1% penicillin/streptomycin, and 2 mM glutamine. All of the following reagents were from Thermo Fisher Scientific (Waltham, MA) and supplemented into the media: F12 nutrient mix, 5 µg/mL insulin, 25 µg/mL hydrocortisone, 125 ng/mL EGF, 250 µg/mL fungizone, 10 µg/mL gentamycin,10 mg/mL nystatin, 11.7 mmol/L cholera toxin, and 5 mmol/L Rho kinase inhibitor Y27632 (Sigma-Aldrich, St. Louis, MO). After 1 month of passages, cells were lysed and subjected to western blot analysis for the detection of NGL-1 expression.

3D microenvironment preparation (Cell-derived ECM (CDM) production)

Production of cell-derived ECM (often referred to as CDM) was conducted as previously described (Franco-Barraza et al., 2016; Franco-Barraza et al., 2017). Briefly, CON or NetG1 KO CAFs ($1.25x10^5$/mL) were seeded onto crosslinked (1% (v/v) glutaraldehyde then 1M ethanolamine) 0.2% gelatin coated wells of a 24 well or 6 well plate. These cells were grown in DMEM supplemented with 15% FBS, 1% Penicillin-Streptomycin (10,000 U/mL), 4mM glutamine, and 50 µg/mL L-ascorbic acid (Sigma-Aldrich, St. Louis, MO), provided fresh, daily. After 5 days of ECM production, cultures were used to collect secreted factors (described below for conditioned media preparation) or cells were lysed and extracted from ECMs using 0.5% Triton X-100 (Sigma-Aldrich, St. Louis, MO) supplemented with 20 mM Ammonia Hydroxide (Sigma-Aldrich, St. Louis, MO), followed by extensive washes with PBS. The resulting cell-free ECMs were used as the 3D scaffold environment for subsequent functional assays.

Conditioned media (CM) preparation

Fibroblast CM was prepared by growing cells during 3D CDM production (see above) for 5 days and then replacing media with glutamine/serum free (-) media. Cells were allowed to condition the media for 2 days. The CM was then collected and used immediately or aliquoted and frozen at -80°C until use (for up to one month).

mRNA Microarray

RNA was isolated from two sets of patient matched tumor adjacent (PSCs) and tumor associated fibroblasts (CAFs) at the end of CDM production (see above), which were generated in two technical repetitions. The RNA was processed by the Genomics Facility at Fox Chase Cancer Center to render differentially expressed genes between the two sets of matching tumor adjacent

bioRxiv preprint doi: https://doi.org/10.1101/330209; this version posted March 8, 2019. The copyright holder for this preprint (which was not certified by peer review) is the author/funder, who has granted bioRxiv a license to display the preprint in perpetuity. It is made available under aCC-BY-NC-ND 4.0 International license.

PSCs and CAFs. Briefly, an Agilent Technologies Gene Chip (~44,000 genes) was used and RNA was hybridized to the chip and run through the Agilent Technologies Instrument (S/N: US22502680). Raw data were processed using the Agilent Feature Extraction 9.5.1.1 Software, outputting processed data into excel spreadsheets. Quantile normalization was applied to microarray data. We applied limma (Ritchie et al., 2015) to identify differentially expressed genes between PSCs and CAFs. Top differentially expressed genes were selected based on p-value < 0.01 and depicted as a heatmap. In order to identify pathways that are enriched between these two cell types, we applied GSEA (preranked with default parameters) on significantly differentially expressed genes (p-value < 0.05) with no fold-change cutoff. To depict the resulting enriched pathways (FDR < 0.25) we applied enrichment map method (Merico et al., 2010). The full data set is available as the supplemental file: “Microarray Data”.

Quantitative Reverse Transcriptase Polymerase Chain Reaction (qRT-PCR)

The Ambion PureLink kit (Life Technologies, Carlsbad, CA) was used, following manufacturer’s instructions, to extract total RNA cells from the various experimental conditions and tested for RNA quality using a Bioanalyzer (Agilent, Santa Clara, CA). Contaminating genomic DNA was removed using Turbo DNA free from Ambion. RNA concentrations were determined with a spectrophotometer (NanoDrop; Thermo Fisher Scientific, Waltham, MA). RNA was reverse transcribed (RT) using Moloney murine leukemia virus reverse transcriptase (Ambion, Life Technologies, Carlsbad, CA) and a mixture of anchored oligo-dT and random decamers (Integrated DNA Technologies, Skokie, Illinois). Two reverse-transcription reactions were performed for each biological replicate using 100 and 25 ng of input RNA. Taqman assays were used in combination with Taqman Universal Master Mix and run on a 7900 HT sequence detection system (Applied Biosystems, Foster City, CA). Cycling conditions were as follows:
95°C, 15 min, followed by 40 (two-step) cycles (95°C, 15 s; 60°C, 60 s).
Ct (cycle threshold) values were converted to quantities (in arbitrary units) using a standard curve (four points, four fold dilutions) established with a calibrator sample. Values were averaged per sample and standard deviations were from a minimum of two independent PCRs. Polymerase (RNA) II (DNA directed) polypeptide F (POLR2F) was used as internal control. Identification numbers of commercial assays (Life Technologies, Carlsbad, CA) and sequences of the NTNG1 primers (FW and RV) and probe for the POLR2F assay are as follows:
GGAAATGCAAGAAGAATTATCAGG (forward),
GTTGTCGCAGACATTCGTACC (reverse),
6fam-CCCCATCATCATTCGCCGTTACC-bqh1 (probe)

SDS-PAGE and Western Blot Analysis

Cell lysates were prepared by adding 150 µL standard RIPA buffer to 6 well plates containing 10^6 cells. The lysates were homogenized using a sonicator. After centrifugation, the supernatant was collected and 30 µg of lysate (determined by the Bradford Assay) was diluted in 2x loading buffer (Bio-Rad, Hercules, CA) and was loaded onto 4-20% polyacrylamide gels (Bio-Rad, Hercules, CA). The gels were run at 70 volts for 2 hours, and transferred to PVDF membranes (Millipore, Burlington, MA) using the semi-dry transfer system (Bio-Rad, Hercules, CA). Membranes were blocked in 5% nonfat milk in 0.1% Tween in tris buffered saline (TBST) for 1 hour at room temperature (RT), and primary antibodies were incubated with the membranes overnight at 4°C. Next, membranes were washed 5 times with 0.1% TBST and then secondary antibodies linked to

bioRxiv preprint doi: https://doi.org/10.1101/330209; this version posted March 8, 2019. The copyright holder for this preprint (which was not certified by peer review) is the author/funder, who has granted bioRxiv a license to display the preprint in perpetuity. It is made available under aCC-BY-NC-ND 4.0 International license.

HRP were diluted in 5% nonfat milk in 0.1% TBST and were applied for 2 hours at RT. Membranes were washed again as before, and incubated for 5 minutes in Immobilon Western Chemiluminescent HRP substrate (Millipore, Burlington, MA). Membranes were developed using film and scanned to create digital images. Primary and secondary antibodies are listed in the Reagents table.

Indirect Immunofluorescence

CAFs were allowed to generate ECM (3D microenvironment) as outlined above (CDM production). After 5 days of ECM production, cells on coverslips were fixed and simultaneously permeabilized for 5 minutes at RT in 4% paraformaldehyde containing 0.5% TritonX-100 and 150 mM sucrose and allowed to continue fixation, using the same preparation lacking triton, for an additional 20 minutes at RT. Fixed/permeabilized cells were then blocked for 1 hour at RT with Odyssey Blocking Buffer (PBS base; Li-Cor, Lincoln, NE). Cells were stained for 1 hour at RT with the following antibodies diluted in blocking buffer: fibronectin (Sigma-Aldrich, St. Louis, MO) and α-smooth muscle actin (α-SMA) (Sigma-Aldrich, St. Louis, MO). After 1 hour incubation, cells were washed 3 times with 0.05% Tween in phosphate buffered saline (PBST), and secondary antibodies diluted in blocking buffer were applied for 1 hour at RT (TRITC for α-SMA; Cy5 for fibronectin, Jackson ImmunoResearch, West Grove, PA). Next, cells were washed 3 times with 0.05% PBST, and nuclei were counter stained with SYBR green (1:10,000; Invitrogen, Carlsbad, CA). Stained coverslips were imaged using Spinning disk confocal microscopy (Perkin Elmer, Waltham, MA), captured by a CoolSNAP CCD Camera (Photometrics, Tucson, AZ) attached to an Eclipse 2000-S inverted microscope (Nikon, Tokyo, Japan). Images were exported from Volocity 3D Image Analysis Software (Perkins Elmer, Waltham, MA). The integrated intensity of α-SMA was quantified using Metamorph Image Analysis Software (Molecular Devices, San Jose, CA). Fibronectin alignment was quantified as described below.

ECM fiber orientation analysis

ECM fiber orientation, indicative of alignment, was performed as previously described (Franco-Barraza et al., 2017). Briefly, confocal images of fibronectin in CAF generated ECM's were analyzed for fiber orientation using the OrientationJ plugin (Rezakhaniha et al., 2012) for ImageJ. Fiber angles generated by the plugin were normalized to fit within the angle range of -90° to +90°. Next, normalized angles were plotted in Excel to generate orientation curves (alignment output at every angle). Finally, the percentage of fibers between -15° to +15° was plotted as a measurement indicative of ECM fiber alignment. In general, tumor adjacent PSCs tend to have disorganized -15° to +15° angle fibers (<50%), while CAFs tend to have fibers with angles >50%.

PDAC Cell Proliferation Assay

CON or NGL-1 KO PDACc cells ($2x10^4$) were seeded in CAF-derived 3D ECMs and allowed to proliferate overnight. Ki67, a nuclear marker of proliferation, and nuclei (DAPI) were stained by IF (as outlined above). The number of Ki67 positive cells/nuclei per field was calculated using Metamorph image analysis software.

bioRxiv preprint doi: https://doi.org/10.1101/330209; this version posted March 8, 2019. The copyright holder for this preprint (which was not certified by peer review) is the author/funder, who has granted bioRxiv a license to display the preprint in perpetuity. It is made available under aCC-BY-NC-ND 4.0 International license.

CRISPR/Cas9 Mediated Knockout of NetG1 and NGL-1

Knockout of NetG1 in CAFs, or NGL-1 in PDACc or PANC-1 cells, was achieved by introducing a frameshift mutation in coding regions of each gene, induced by cuts made by CRISPR/Cas9 and gene specific gRNAs introduced into cells by lentiviral transduction.

gRNA design:

Using the MIT Optimized CRISPR Design website: http://crispr.mit.edu/, the first 200 bp of exon 5 for NetG1 (first common exon for all splice variants) and first 220 bp of the NGL-1 gene were used to generate gRNAs. The top two hits for each gene were selected and designed to include BsmBI/Esp3I overhangs (bold, underline, italics), the specific gRNA sequence (plain text). G (italics, underline) was added to the .1 gRNAs (and corresponding C on the .2 gRNA) to optimize its expression for the human U6 promoter.

The gRNA sequences are listed below:

NetrinG1 gRNA 1.1	***CACC***<u>*G*</u>GGCGTCCAGACCAAATGATCC
NetrinG1 gRNA 1.2	***AAAC***GGATCATTTGGTCTGGACGC***C***
NetrinG1 gRNA 2.1	***CACC***<u>*G*</u>TGATGCGAGTACCCCTGAGC
NetrinG1 gRNA 2.2	***AAAC***GCTCAGGGGTACTCGCATCA***C***
NGL1 gRNA1.1	***CACC***<u>*G*</u>AACCTGCGTGAGGTTCCGGA
NGL1 gRNA1.2	***AAAC***TCCGGAACCTCACGCAGGTT***C***
NGL1 gRNA 2.1	***CACC***<u>*G*</u>TGCCATCCGGAACCTCACGC
NGL1 gRNA 2.2	***AAAC***GCGTGAGGTTCCGGATGGCA***C***

Empty vector or Nontargeting gRNA against eGFP was used as a control:

eGFP gRNA 2.1	***CACC***<u>*G*</u>CATGTGATCGCGCTTCTCGT
eGFP gRNA 2.2	***AAAC***ACGAGAAGCGCGATCACATG***C***

Generation of Lentiviral Vectors:

Designed oligos were ordered from Integrated DNA Technologies (Skokie, Illinois) and cloned into the LentiCRISPR v2 vector, as previously published (a gift from Feng Zhang; Addgene plasmid # 52961; (Franco-Barraza et al., 2017; Sanjana et al., 2014). Briefly, oligos were phosphorylated using T4 PNK (New England Biolabs, Ipswich, MA) and annealed in a thermal cycler. Annealed oligos were cloned into a gel purified (GeneJet Gel Extration Kit; Thermo Fisher Scientific, Waltham, MA), dephosphorylated (Fast AP; Thermo Fisher Scientific, Waltham, MA), and digested vector (Fast Digest Esp3I; Thermo Fisher Scientific, Waltham, MA). Annealed oligos were ligated into the digested vector using quick ligase (New England Biolabs, Ipswich, MA). The ligated vectors were transformed into Stbl3 strain of *Escherichia coli* (Thermo Fisher Scientific, Waltham, MA) and selected with 100 µg/mL ampicillin on LB/agar plates. The following day, single colonies of bacteria were screened by colony PCR using a forward primer for the U6 promoter (GAGGGCCTATTTCCCATGATT) and the reverse primer sequence (gRNA x.2) for each gene.

bioRxiv preprint doi: https://doi.org/10.1101/330209; this version posted March 8, 2019. The copyright holder for this preprint (which was not certified by peer review) is the author/funder, who has granted bioRxiv a license to display the preprint in perpetuity. It is made available under aCC-BY-NC-ND 4.0 International license.

Positive clones were subjected to sequencing and subsequently expanded for plasmid purification and lentivirus production.

Lentiviral Transduction:

To package the LentiCRISPRv2 plasmid into functional virus particles, 10 µg LentiCRISPRv2, 5 µg psPAX2 (psPAX2 was a gift from Didier Trono; Addgene plasmid # 12260) and 2 µg VSVg were mixed with 30 µL X-tremeGene9 transfection reagent (Sigma-Aldrich, St. Louis, MO) in 1 mL of serum free/antibiotic free DMEM and held at RT for 30 minutes. The transfection mixture was added dropwise to 293T cells containing 5 mL serum free/antibiotic free DMEM and the cells were incubated at 37°C overnight. The next day, the media was replaced with complete DMEM media. On days 2 and 4 post-transfection, the media with viral particles was collected and syringe filtered through a 0.45 µM filter (Millipore, Burlington, MA). The filtered viral supernatant was used immediately to transduce target cells (PDACc/PANC-1 or fibroblasts) with 10 µg/mL polybrene (Santa Cruz Biotechnology, Dallas, Texas) or stored at -80°C for use in the future. Target cells were selected with puromycin (2 µg/mL for CAFs, 5 µg/mL PANC-1, 12 µg/mL KRAS) for 2 weeks. Cells that survived selection were used for future experiments.

Generation of RFP+ and GFP+ CRISPR/Cas9 transduced cells:

eGFP and mCherry (RFP) were PCR amplified using Phusion HF polymerase master mix (Thermo Fisher Scientific, Waltham, MA) to add overhangs compatible with restriction enzymes. Then cloned into XbaI/XhoI (New England Biolabs, Ipswich, MA) digested, Fast AP dephosphorylated pLV-CMV-H4-puro vector (kindly provided by Dr. Alexey Ivanov, West Virginia University School of Medicine, Morgantown, WV, USA). Empty vector transduced (CON) or NetG1 KO CAF were transduced with pLV-CMV-H4-puro-GFP and the CON or NGL-1 KO PDACc were transduced with pLV-CMV-H4-puro-RFP, with 10 µg/mL polybrene. Cells were selected by flow cytometry. The selected cells were used for future experiments.

CRISPR interference (CRISPRi) mediated Knockdown of NetG1 and VGlut1

We generated a lentiviral vector named CRISPRi-Puro (modified from pLV hU6-sgRNA hUbC-dCas9-KRAB-T2a-Puro; Addgene Plasmid #71236; a gift from Charles Gersbach) (Thakore et al., 2015) containing dead Cas9 (dCas9) fused to Krueppel-associated box (KRAB) domain, gRNA cloning site, and puromycin resistance. The gRNA cloning site was modified to contain a “stuffer” (cut from LentiCRISPRv2 plasmid using the restriction enzyme BsmBI and ligated into our vector) that resulted in a higher gRNA cloning efficiency. Upon insertion of gene specific gRNA, dCas9-KRAB mediated knockdown of target genes could be achieved. Three gRNA oligos were selected from the top ten gRNA sequences generated from the study “Compact and highly active next-generation libraries for CRISPR-mediated gene repression and activation” (Horlbeck et al., 2016). Generation of the vector and transduction of the target cells was performed as described above for the generation and transduction of the LentiCRISPRv2 vector. The best two knockdown cell lines generated were subsequently used for all experiments. Cells transduced with vector alone were used as a control.
The selected oligos are listed below:

NetrinG1 CRISPRi gRNA 1.1	***CACC***GGCGCCCCGAGGTCGTGGAG
NetrinG1 CRISPRi gRNA 1.2	***AAAC***CTCCACGACCTCGGGGCGCC***C***

bioRxiv preprint doi: https://doi.org/10.1101/330209; this version posted March 8, 2019. The copyright holder for this preprint (which was not certified by peer review) is the author/funder, who has granted bioRxiv a license to display the preprint in perpetuity. It is made available under aCC-BY-NC-ND 4.0 International license.

NetrinG1 CRISPRi gRNA 2.1	***CACC***GACAGCAACAGCGAGCGGGA
NetrinG1 CRISPRi gRNA 2.2	***AAAC***TCCCGCTCGCTGTTGCTGTC***C***
NetrinG1 CRISPRi gRNA 3.1	***CACC***GCGAGAGCCGGAAAGAGGAG
NetrinG1 CRISPRi gRNA 3.2	***AAAC***CTCCTCTTTCCGGCTCTCGC***C***
VGlut1 CRISPRi gRNA 1.1	***CACC***GAGAGAGAGTGGAGCCGGGT
VGlut1 CRISPRi gRNA 1.2	***AAAC***ACCCGGCTCCACTCTCTCTC***C***
VGlut1 CRISPRi gRNA 2.1	***CACC***GGCTCCGCTCGGGGGGAAGG
VGlut1 CRISPRi gRNA 2.2	***AAAC***CCTTCCCCCCGAGCGGAGCC***C***
VGlut1 CRISPRi gRNA 3.1	***CACC***GAGAGACCCAGAAGTGGTGG
VGlut1 CRISPRi gRNA 3.2	***AAAC***CCACCACTTCTGGGTCTCTC***C***

Cell Engagement/Motility Assays

RFP+ CON or NGL-1 KO PDACc ($5x10^4$) were plated with GFP+ CON or NetG1 KO CAFs ($5x10^4$) in 3D and allowed to attach for 2 hours. Following cell attachment, 3 regions per well, where there was obvious clustering of red PDACc and green CAFs, were selected to be imaged every 15 minutes for 24 hours, using a motorized XYZ stage (Optical Apparatus Co., Ardmore, PA) controlled by MetaMorph 6.3r7 (Molecular Devices, Downingtown, PA) software. Time-lapse movies were built with images from each corresponding fluorescence channels acquired every 15 min for a period of 24 hours using either 4X or 20X Pan Fluor objectives mounted on a Nikon TE-2000U wide field inverted microscope (Optical Apparatus Co., Ardmore, PA) with a Cool Snap HQ camera rendering 3 time-lapse movies per condition for a total of 9 videos generated over 3 independent experimental repetitions. The resulting time-lapse videos were analyzed to quantify heterotypic cell engagement (yellow interacting areas using both channels simultaneously in merged file stacks) and PDACc cell motility (using only the monochromatic images corresponding to the red channel), as outlined below.

Cell Engagement:

For image analysis MetaMorph offline 7.8.1.0 software was used. To achieve sequence coherence, out of focus or blank images from particular fluorescence channels were removed, together with its fluorescence counterpart image. All movies were normalized (trimmed) to 18 hours data for analysis. Images were scaled and pseudocolored (RFP in red, GFP in green) similarly for all conditions. After merging of fluorescence channels, cell engagement areas (CEA) obtained from regions of fluorescence colocalization (in yellow) were digitally detected, isolated and measured for each condition over time.

PDAC Cell Motility:

Monochromatic channel of RFP+ PDAC cells were tracked using the Track Object function in MetaMorph 7.8.1.0 offline software (Molecular Devices, Downingtown, PA). A minimum of 5 cells per region were chosen to carefully follow. Red PDACc that were touching other red PDACc, moving out of the imaging plane, or that began to round up prior to mitosis were not counted in

bioRxiv preprint doi: https://doi.org/10.1101/330209; this version posted March 8, 2019. The copyright holder for this preprint (which was not certified by peer review) is the author/funder, who has granted bioRxiv a license to display the preprint in perpetuity. It is made available under aCC-BY-NC-ND 4.0 International license.

this experiment. Motility was analyzed according to the total distance (µm) traveled over the timespan of the experiment (24 hr), expressed as velocity (µm/hr).

Material Transfer Assay

$2x10^4$ RFP+ CON or NGL-1 KO PDACc and/or $2x10^4$ GFP+ CAFs were seeded in 3D and were co-cultured for 36 hours, in serum free DMEM. Spinning disk confocal images (Perkin Elmer, Waltham, MA) were captured by a CoolSNAP CCD Camera (Photometrics, Tucson, AZ) attached to an Eclipse 2000-S inverted microscope (Nikon, Tokyo, Japan). Images were exported from Volocity 3D Image Analysis Software (Perkins Elmer, Waltham, MA) and quantified for the integrated intensity of GFP+ pixels under RFP+ pixels, using Metamorph Image Analysis Software (Molecular Devices, San Jose, CA), which was indicative CAF derived GFP material transfer to RFP+ PDACc.

PDAC Survival Assay

$2x10^4$ RFP+ CON or NGL-1 KO PDAC cells (PDACc or PANC-1) and/or $2x10^4$ GFP+ CON or NetG1 KO CAFs were seeded in 3D (CON CAF, NetG1 KO, or normal PSC ECMs, as indicated) in 24 well plates. Cells were co-cultured for 96 hours in glutamine free/serum free DMEM. Next, at least 10 images were taken of red PDAC cells and green CAFs using a Cool Snap 1HQ camera (Roper Scientific, Vianen, Netherlands) on an Eclipse 2000-U inverted microscope (Nikon, Tokyo, Japan). PDAC cell survival was quantified as the number of RFP+ per field of view, using Image J. Dead cells were excluded by Sytox Blue (1 µM; Thermo Fisher Scientific, Waltham, MA) positivity or cell size. Briefly, identical thresholds were established for each color channel for each batch of images per experiment. Then the images were batch processed using a macro that measures cell counts and % area coverage of cells in each image, at a given threshold. The mean RFP+/Sytox blue negative cells (live) from each condition was calculated (counts or % area, depending on the experiment) and normalized to the CON PDAC/CON CAF condition. Cell counts were chosen when cells were clearly isolated (accurate cell counts), and % area was chosen when cells had more overlap (could not accurately determine cell counts). The 96 hour timepoint was determined empirically, when cell death became evident by eye. Other PDAC survival assays were performed with CAF conditioned media (CM), VGlut1 KD CAFs, or CAFs pretreated 24 hours with 1mM L-Methionine sulfoximine (Sigma-Aldrich, St. Louis, MO), as indicated.

NK-92 cell killing assay

$2x10^4$ RFP+ CON or NGL-1 KO PDAC cells and/or $2x10^4$ GFP+ CON or NetG1 KO CAFs were seeded in 3D in 24 well plates and were co-cultured in 500 µL NK-92 media without IL-2 to establish their niche. The following day, wells were seeded with $8x10^4$ resting or active NK-92 cells, in 500 µL of NK-92 media without IL-2. Cells were co-cultured for 48 hours and PDAC survival was assessed identically to the PDAC cell survival assay. To produce active NK-92 cells, cells were maintained with 400 units/mL IL-2 and for resting NK-92 cells, cells were maintained for one week in 100 units/mL IL-2 and switched overnight to NK culture media containing no IL-2 the day before the experiment. For 2D conditions, all experimental conditions were the same, except the endpoint of the experiment was at 6-8 hours, as lack of CAF derived ECM (3D microenvironment) allowed NK-92 cells to kill at a faster rate. For the IL-15 neutralizing experiments, an IL-15 neutralizing antibody (10 µg/mL; R&D Systems, Minneapolis, MN) or Nonspecific IgG isotype control (10 µg/mL; Jackson Immunoresearch, West Grove, PA) were added to the co-cultures where specified. Whenever CON or NetG1 KO CAF CM was used, it

bioRxiv preprint doi: https://doi.org/10.1101/330209; this version posted March 8, 2019. The copyright holder for this preprint (which was not certified by peer review) is the author/funder, who has granted bioRxiv a license to display the preprint in perpetuity. It is made available under aCC-BY-NC-ND 4.0 International license.

was diluted 1:1 in NK-92 media without IL-2. Images were quantified for live PDAC cells as in the "PDAC Survival Assay" section above.

NK-92 cell activation assay

$8x10^4$ IL-2 activated NK-92 cells were directly co-cultured (CC) with CAFs or with conditioned media (CM) derived from CAFs for 2 hours. After the co-culture period, NK-92 activation status was determined by staining Granzyme B intracellularly, or by using the IFNγ secretion assay detection kit. Stained cells were subjected to flow cytometry using by LSRII (Beckton Dickinson, San Jose, CA) and analyzed with FlowJo 9.9 software (Tree Star, San Carlos, CA). IL-2 activated NK-92 cells cultured alone were used as the positive control. Percentage of cells that were positive for either Granzyme B or IFNγ were considered activated.

Enzyme-linked immunosorbent assay (ELISA)

ELISAs for IL-15, IFN-β, and TGF-β (R&D Systems, Minneapolis, MN) were performed as recommended by the manufacturer. Briefly, buffers for the IL-15 and IFN-β ELISAs were prepared using the DuoSet ELISA Ancillary Reagent Kit 2, and buffers were prepared using the DuoSet ELISA Ancillary Reagent Kit 1 for the TGF-β ELISA (R&D Systems, Minneapolis, MN). Standards, CM or lysates from Normal PSCs, CON CAFs, or NetG1 KO CAFs were incubated for 2 hours on plates pre-coated overnight with capture antibody. For the TGF-β ELISA, samples first underwent activation using the Sample Activation Kit 1 (R&D Systems, Minneapolis, MN) before sample incubation. Next, detection antibody linked to biotin was added to the wells and incubated for 2 hours. Streptavidin-HRP was then added to the wells and incubated for 20 mins. Samples were rinsed 3 times with wash buffer in between all steps. Substrate was added for 20 min and was neutralized with stop buffer. Plates were read using Spark® Multimode Microplate Reader (Tecan, Switzerland) at 450 nm to measure the specified protein present in sample. Plate imperfections, measured at 570 nm, were subtracted from the readings at 450 nm, to produce corrected readings. Finally, media alone (BLANK) was subtracted from the corrected readings for each sample. To determine the concentration of the indicated protein in each sample, a standard curve was generated using known concentrations of analyte, and the blank corrected values determined for each sample were compared to the standard curve.

U-Plex Assay

U-Plex Assay (multiplex ELISA) was carried out as recommended by the manufacturer (Meso Scale Discoveries, Rockville, MD). Briefly, Normal PSC and CON or NetG1 KO CAF CM samples were generated and added to a pre-coated plate containing 10 capture antibodies per well for the detection of the following proteins: IL-1β, IL-2, IFNγ, GM-CSF, IL-6, IL-8, IL-10, IL-12p70, MIP3α, and TNFα. After 3 washes, sample, standards, or calibrator were added to the wells and incubated for 1 hour. Next, after 3 washes, detection antibody was added to the wells and incubated for 1 hour. After a final set of 3 washes, read buffer was added to the wells and the plate was read using the MSD SECTOR Imager 2400 (Meso Scale Discoveries, Rockville, MD) and the data was processed using the MSD Workbench 4.0 software (Meso Scale Discoveries, Rockville, MD).

Amino Acid Screen: Biochrom Method

*Media***:** 20 µL of media was mixed with 80 µL of water and 100 µL of 10% Sulfosalicylic acid (Sigma-Aldrich, St. Louis, MO) followed by incubation for 1 hour at 4°C and then centrifugation at 13,000 rpm (15 min; 4°C). No visible pellet was seen. Supernatant was filtered using Ultrafree-

bioRxiv preprint doi: https://doi.org/10.1101/330209; this version posted March 8, 2019. The copyright holder for this preprint (which was not certified by peer review) is the author/funder, who has granted bioRxiv a license to display the preprint in perpetuity. It is made available under aCC-BY-NC-ND 4.0 International license.

MC-GV centrifugal filters (Millipore, Burlington, MA) and used for amino acid analysis employing Biochrom 30 amino acid analyzer. Results are in terms of µM.

Cell Lysates: 14.55 µg of cell lysate protein in RIPA buffer was brought to a total volume of 50 µL in water and was mixed with 50 µL of 10% Sulfosalicylic acid (Sigma-Aldrich, St. Louis, MO) followed by incubation for 1 hour at 4°C and then centrifugation at 13,000 rpm (15 min; 4°C). Supernatant was filtered using Ultrafree-MC-GV centrifugal filters (Millipore, Burlington, MA) and used for amino acid analysis employing the Biochrom 30 amino acid analyzer (Biochrom US, Holliston, MA). Results were provided in nmol/mg protein units.

Amino Acid Screen: Mass Spectrometry

Metabolite Extraction and Quantitation

Metabolites were extracted from media and quantitated as described previously (Muir et al., 2017). 10µL of media was mixed with 10µL of a mixture of isotopically labeled metabolites and amino acids of known concentrations (Cambridge Isotope Laboratories, Tewksbury, MA) and extracted with 600µL ice-cold HPLC grade methanol. Samples were vortexed for 10 mins at 4ºC, centrifuged at max speed on a tabletop centrifuge for 10min 4ºC, and then 450uL of supernatant was dried under nitrogen gas and frozen at -80ºC until analyzed by GC-MS.

Gas Chromatograpy-Mass Spectrometry Analysis

Polar metabolites were analyzed by GC-MS as described previously (Lewis et al 2014, Muir et al eLife). Dried metabolite extracts were derivatized with 16µL MOX reagent (Thermofisher, Waltham, MA) for 90 min. at 37°C, followed by 20 µL of N-tertbutyldimethylsilyl-N-methyltrifluoroacetamide with 1% tert-butyldimethylchlorosilane (Sigma Aldrich, St. Louis, MO) for 60 min. at 60°C. After derivatization, samples were analyzed by GC-MS using a DB-35MS column (Agilent Technologies, Santa Clara, CA) installed in an Agilent 7890A gas chromatograph coupled to an Agilent 5997B mass spectrometer. Helium was used as the carrier gas at a flow rate of 1.2 mL/min. One microliter of sample was injected in split mode (all samples were split 1:1) at 270°C. After injection, the GC oven was held at 100°C for 1 min. and increased to 300°C at 3.5 °C/min. The oven was then ramped to 320°C at 20 °C/min. and held for 5 min. at this 320°C. The MS system operated under electron impact ionization at 70 eV and the MS source and quadrupole were held at 230°C and 150°C respectively. The detector was used in scanning mode, and the scanned ion range was 100–650 m/z.

Human NK cell Isolation and Activation Experiments

Isolation of Primary NK cells:

Blood was collected into heparinized tubes from healthy volunteer donors that consented using HIPAA-compliant procedures approved by the Institutional Review Board of Fox Chase Cancer Center. NK cells were enriched from healthy donor PBMCs using the EasySep NK cell negative selection kit (StemCell Technologies, Cambridge, MA) and confirmed to be >95% purity using flow cytometry.

Primary NK Cell Activation Assay:

bioRxiv preprint doi: https://doi.org/10.1101/330209; this version posted March 8, 2019. The copyright holder for this preprint (which was not certified by peer review) is the author/funder, who has granted bioRxiv a license to display the preprint in perpetuity. It is made available under aCC-BY-NC-ND 4.0 International license.

Purified NK cells were incubated overnight at 37°C in indicated percentages of CON or NetG1 CAF CM diluted in NK cell media (10%-65%) in the presence of IL-2 (500 units/mL) and IL-12 (10 ng/mL). NK cells activated with IL-2 and IL-12 were used as a positive control. After overnight incubation, the population of IFNγ secreting cells was identified using the IFNγ Secretion assay detection kit (PE) (Miltenyi Biotec, Bergisch Gladbach, Germany) according to the manufacturer's protocol. After a 2 hour incubation with IFNγ catch reagent, cells were washed twice. Next, cells were stained with IFNγ detection antibody and antibodies against NKp80 (anti-NKp80-APC, Biolegend, San Diego, CA), CD3 (anti-CD3-Cy7APC, BD Pharmigen, San Jose, CA), CD56 (anti-CD56-BUV395, BD Horizon, San Jose, CA), CD69 (anti-CD69-Pac Blue, San Diego, CA). Cells were centrifuged and rinsed twice, with propidium iodide in the second wash. NK cells were defined as NKp80+CD56+CD3- cells.

Flow cytometry and data analysis:

Stained cells were analyzed on a BD ARIA II flow cytometer (Becton Dickinson, Franklin Lakes, NJ). Data was collected with BD FACS Diva software (v6) and analyzed with FlowJo (v9.9; Tree Star Inc., Ashland, OR). IFNγ and CD69 expression were identified as the percentage of IFNγ+ cells or mean fluorescence intensity (MFI) of CD69+ cells. The data were normalized to the positive control (NK cells with IL2/IL12 treatment alone).

Mouse Models

Tissue for stromal analysis was obtained from the LSL-**K**RAS^{G12D}, PDX1-**C**re (KC) model (Hingorani et al., 2003), and KPC4B and KPC3 murine PDAC cell lines were derived from tumors generated from a variant of LSL-**K**RAS^{G12D}, T**P**53$^{-/-}$, PDX1-**C**re (KPC) mice (Hingorani et al., 2005).

Murine PDAC cell orthotopic injections

All animal work was performed under protocols approved by IACUC at Fox Chase Cancer Center. A small incision was made in the abdominal skin of the mice, and gently moved aside the spleen to reveal the pancreas. Next, 10^6 murine CON or NGL-1 KO #1 or #2 PDAC cells (derived from KPC tumors), were injected (100 µL) orthotopically into the pancreas of syngeneic C57BL/6 mice and tumors were allowed to develop for 3.5 weeks. Mice were monitored by observation, palpation, and weekly MRIs and sacrificed at 3.5 weeks. Pancreas weights were obtained and pancreatic tissue was further analyzed as described below. To determine the effect of the immune system on tumorigenesis in the orthotopic model, the injections were performed as above, with the following mice used as hosts:

C57BL/B6 (immunocompetent; FCCC), C.B17 Severe Combined Immunodeficient, (SCID; lacks T and B cells; Taconic Bioscience), and NOD.Cg-Prkdc^{scid} IL2rg^{tm1Wjl}/SzJ: NOD *scid* gamma (NSG; lacks NK, T, and B cells; Jackson Laboratories).

Magnetic Resonance Imaging (MRI)

Animals were imaged in a 7 Tesla vertical wide-bore magnet, using a Bruker DRX 300 spectrometer (Billerica, MA) with a micro-imaging accessory, which included a micro 2.5 gradient set, a 30 cm radiofrequency coil, and Paravision software (Bruker, Billerica, MA). Animals were anesthetized with a mixture of oxygen and isoflurane (2-3%). An injection of 0.2 mL of 10:1 diluted Magnevist (gadopentetate dimeglumine; Bayer, Whippany, NJ) was made into the shoulder

bioRxiv preprint doi: https://doi.org/10.1101/330209; this version posted March 8, 2019. The copyright holder for this preprint (which was not certified by peer review) is the author/funder, who has granted bioRxiv a license to display the preprint in perpetuity. It is made available under aCC-BY-NC-ND 4.0 International license.

region immediately preceding the scan. Scout scans were performed in the axial and sagittal orientations, permitting us to accurately prescribe an oblique data set in coronal and sagittal orientations that included the organs of interest. A two-dimensional spin echo pulse sequence was employed with echo time 15 msec, repetition time 630 msec, field of view = 2.56 cm, acquisition matrix= 256x256, slice thickness= 0.75 mm, 2 averages, scan time = 5 minutes. Fat suppression (standard on Bruker DRX systems) was used for all scans. Raw data files were converted to Tiff format image files using the Bruker plugin on ImageJ.

Murine tissue preparation and histopathological analysis

Tissue Preparation:

Tissues were collected and fixed in 10% phosphate-buffered formaldehyde (formalin) 24-48 hrs, dehydrated and embedded in paraffin. Tissues were processed by dehydration in a series of ethanol followed by xylene (70% ethanol 3 hr, 95% ethanol 2 hr, 100% ethanol 2 hr, 100% ethanol Xylene mixed 1hr, Xylene 3hr, then immersed in Paraffin). Paraffin blocks were cut into 5 µm sections, mounted on microscope slides, and stored at room temperature until used. Sections were stained with hematoxylin and eosin for pathologic evaluation.

All H&E slides were viewed with a Nikon Eclipse 50i microscope and photomicrographs were taken with an attached Nikon DS-Fi1 camera (Melville, NY, USA).

Tumor area analysis:

H&E stained slides were also scanned using Aperio ScanScope CS scanner (Aperio, Vista, CA). Scanned images were then viewed with Aperio's image viewer software (ImageScope). Selected regions of interest for PDAC and total pancreatic areas were outlined respectively by a pathologist, who was blinded to the treatment groups. The ratio of PDAC to the total pancreatic areas scanned was calculated for each animal.

Differentiation status of tumor cells:

H&E images of pancreata injected with CON or NGL-1 KO cells were scored for the percentage of cells that were well differentiated, moderately differentiated, or poorly differentiated, as determined by a pathologist, who was blinded to the treatment groups.

TUNEL Staining:

Apoptotic cells were quantified using the DeadEnd™ Fluorometric TUNEL System (Promega, Madison, WI), per manufacturer's instructions. Briefly, tissue was deparaffinized and fixed in 4% formaldehyde for 15 minutes at RT. After 2 PBS washes, tissue was treated with 20 µg/mL proteinase K solution for 10 minutes at RT. After 2 PBS washes, slides were fixed again in 4% formaldehyde for 5 minutes at RT. Tissue was then submerged in Equilibration buffer at RT for 5 minutes. Next, apoptotic cells were labeled with TdT reaction mixture for 1 hour at 37°C. After 1 hour, the reaction was stopped by adding SSC buffer for 15 minutes at RT. Tissue was then washed 3x in PBS and then stained with DAPI (1:10,000) for 15 minutes at RT. Finally, after an additional wash, tissue was mounted and imaged using the Eclipse 2000-U inverted microscope.

bioRxiv preprint doi: https://doi.org/10.1101/330209; this version posted March 8, 2019. The copyright holder for this preprint (which was not certified by peer review) is the author/funder, who has granted bioRxiv a license to display the preprint in perpetuity. It is made available under aCC-BY-NC-ND 4.0 International license.

Metamorph software was used to quantify dead cells (green)/nuclei (blue) in each field of view. At least 10 images (20X) per sample were acquired.

Ki67 staining (proliferation):

IF on tissue sections was done as previously published (Franco-Barraza et al., 2017). Briefly, deparaffinized tissue underwent antigen retrieval by boiling in buffer containing 10 mM Sodium citrate, 0.05% Tween 20, pH 6.0 for 1 hour. Next, tissue was blocked in Odyssey Blocking Buffer (PBS base) (LI-COR Biosciences, Lincoln, NE) for 1 hour at RT. Tissue was then stained with primary antibody against Ki67 (Abcam, Cambridge, UK) overnight at 4°C. The following day, tissue was washed 3 times in 0.05% PBST, and secondary antibody conjugated to TRITC (Jackson ImmunoResearch, West Grove, PA) was applied to the samples for 2 hours at RT. After 3 additional washes, nuclei were stained with DAPI (1:10,000) for 15 minutes at RT. After one final wash, samples were mounted and images (20X) were captured using an Eclipse 2000-U inverted microscope. Proliferating cells (red)/nuclei (blue) in each field of view were quantified using Metamorph Software.

Acquisition and Use of Human Tissue

All human tissues used in this paper were collected using HIPAA approved protocols and exemption-approval of the Fox Chase Cancer Center's Institutional Review Board, after patients signed a written informed consent in which they agreed to donate surgical specimens to research. To protect patient's identity, samples were classified, coded and distributed by the Institutional Biosample Repository Facility. Normal pancreatic tissue was obtained through US Biomax Inc. (Rockville, MD) following their rigorous ethical standards for collecting tissue from healthy expired donors.

Simultaneous Multichannel Immunofluorescence (SMI)

Qdot antibody conjugation

Corresponding antibodies were linked to Qdot molecules using SiteClick Qdot labeling from Molecular Probes-ThermoFisher Scientific. In brief, approximately 100 mg of specific IgG were pre-purified to remove excessive carrier proteins (if needed) and each conjugation was performed following manufacturer's three-step protocol requiring antibody's carbohydrate domain modifications to allowing an azide molecule attachment to facilitate linking DIBO-modified nanocrystals to the antibodies.

Formalin fixed and paraffin embedded (FFPE) tissue processing

FFPE sections were deparaffinized using xylene and rehydrated in progressive ethanol to water dilutions. Tissues then were processed through heat-induced epitope retrieval using pH 6.0 Citrate buffer, followed by permeabilization with 0.5% TritonX-100. After treating the specimens with Odyssey (PBS base) blocking buffer (LI-COR Biosciences, Lincoln, NE) samples were labeled by a three-day indirect immunofluorescence scheme. Initially, primary antibodies against mouse monoclonal NetG1 (D-2, Santa Cruz. Dallas, TX) and rabbit polyclonal NGL-1 (N1N3, Genetex Inc., Irvine, CA) were incubated at 4°C overnight, followed by anti-mouse Q625 and anti-rabbit Q655 secondary antibodies, together with primary rabbit polyclonal Y397P-FAK (Genetex

bioRxiv preprint doi: https://doi.org/10.1101/330209; this version posted March 8, 2019. The copyright holder for this preprint (which was not certified by peer review) is the author/funder, who has granted bioRxiv a license to display the preprint in perpetuity. It is made available under aCC-BY-NC-ND 4.0 International license.

Inc., Irvine, CA) pre-linked to Q605, for an overnight incubation (see Q-dots antibody conjugation details above). After washes, specimens were treated with corresponding monovalent Fab IgG fragments (Jackson Immuno Research Inc., West Grove, PA) to avoid cross-reaction during the incubation of the following cocktail of primary antibodies: mouse monoclonal anti-pan-cytokeratin (clones AE1/AE3, DAKO) to detect the epithelial compartment; rabbit monoclonal anti-vimentin (EPR3776, Abcam) antibodies for mesenchymal (stromal) components. Secondary antibodies used were donkey anti-mouse Cy3 and donkey anti-rabbit Cy2 (Jackson Immuno Research Inc., West Grove, PA). Nuclei were labeled by DRAQ5 (Invitrogen-Thermo Fisher Scientific, Waltham, MA). Lastly, sections were dehydrated in progressive ethanol concentrations and clarified in Toluene before mounting using Cytoseal-60 (Thermo Fisher Scientific, Waltham, MA). Slides were cured overnight in dark at RT before the imaging.

Image acquisitions for SMI analysis

Imaging of fluorescently labeled tissue sections was performed utilizing Nuance-FX multispectral imaging system (Caliper LifeSciences, PerkinElmer), using full capabilities of its Tunable Liquid Crystal imaging module, attached to a Nikon Eclipse TE-2000-S epifluorescence microscope. Images were acquired using a Plan Fluor 40X/0.75 objective. A specific wavelength based spectral library for each system was built using control pancreatic tissues (i.e. murine and human), individually labeled for each Qdot and fluorophore used. Unstained specimens were also included to digitally discard specific auto-fluorescence spectra. Each particular spectral library was used for the subsequent image acquisition and analysis. All excitations were achieved via a high-intensity mercury lamp using the following filters for emission-excitation, for Nuance-FX, DAPI (450-720), FITC (500-720), TRITC (580-720), CY5 (680-720). Excitation was conducted from the infrared to ultraviolet spectrum, attempting to avoid energy transfer and excitation of nearby fluorophores. Emission was collected using 'DAPI' filter (wavelength range 450–720) for all Qdot labeled markers, while masks used the conventional FITC, TRITC, and CY5 filters.

Collected image cubes (multi-spectral data files) were unmixed to obtain 16-bit (gray scale) individual monochromatic files. Next, the images were processed in bulk for similar levels adjustment and 8-bit monochromatic image conversion for each channel, using Photoshop's 'Levels' and 'Batch processing' automated functions. The resulting images were sampled to set identical threshold values for each marker (NetG1, Y397P-FAK and NGL-1) and masks (vimentin and nuclei). Threshold values distinguishing cytokeratin in normal versus tumor samples needed to be independently adjust for each tissue set to assure variations in intensity staining patterns between the two types of epithelium (i.e., normal vs tumoral) were accounted for, as these were needed to be used as "gating masks" identifying epithelial/tumoral area pixels. Processed images were used to analyze distribution, intensity and co-localization of positive-selected pixels using SMIA-CUKIE (SCR_014795) algorithm, available online at https://github.com/cukie/SMIA (Franco-Barraza et al., 2017).

SMIA-CUKIE usage and outputs

As described previously (Franco-Barraza et al., 2017), SMIA-CUKIE algorithm (SCR_014795) was used to analyze high throughput monochromatic images acquired from SMI-processed FFPE

bioRxiv preprint doi: https://doi.org/10.1101/330209; this version posted March 8, 2019. The copyright holder for this preprint (which was not certified by peer review) is the author/funder, who has granted bioRxiv a license to display the preprint in perpetuity. It is made available under aCC-BY-NC-ND 4.0 International license.

tissue sections. In brief, the algorithm is based on the usage of digital masks, constructed from pixel-positive area distribution, resulting in tissue compartmentalization (i.e. cytokeratin positive/vimentin negative area: epithelium/tumor compartment *vs.* vimentin positive/cytokeratin negative area: stromal compartment). Next, we queried mean, median, coverage area, integrated intensity of the markers of interest (i.e. NetG1, NGL-1, Y397P-FAK), under each mask. Each mask and marker required a numeric threshold (0-255), indicating the value of pixel intensity considered positive for each channel (corresponding to each mask and marker). These were kept identical for each marker and mask throughout the study. Finally, the analysis generated an Excel file containing numerical values, which were scrutinized for statistical significance as described in the corresponding statistical analysis section. Black lines through a row indicate an unquantifiable image. The algorithm is available at the public domain: https://github.com/cukie/SMIA_CUKIE. This dataset is available as the supplemental material file: “Human Single Patient SMI”.

RNA sequencing

Stranded mRNA-seq library: 1000ng total RNAs from each sample were used to make library according to the product guide of Truseq stranded mRNA library kit (Illumina, Cat# 20020595). In short, mRNAs were enriched twice via poly-T based RNA purification beads, and subjected to fragmentation at 94 degree for 8 min via divalent cation method. The 1st strand cDNA was synthesized by SuperscriptII reverse transcriptase (ThermoFisher, Cat# 18064014) and random primers at 42 degree for 15 mins, followed by 2nd strand synthesis at 16 degree for 1hr. During second strand synthesis, the dUTP was used to replace dTTP, thereby the second strand was quenched during amplification. A single ‘A’ nucleotide is added to the 3’ ends of the blunt fragments at 37 degree for 30 min. Adapters with illuminaP5, P7 sequences as well as indices were ligated to the cDNA fragment at 30 degree for 10 min. After SPRIselect beads (Beckman Coulter, Cat# B23318) purification, a 15-cycle PCR reaction was used to enrich the fragments. PCR was set at 98 degree for 10 sec, 60 degree for 30 sec and extended at 72 degree for 30 sec. Libraries were again purified using SPRIselect beads, had a quality check on Agilent 2100 bioanalyzer (serial # DE34903146) using Agilent high sensitivity DNA kit (Cat# 5067-4626), and quantified with Qubit 3.0 flurometer (ThermoFisher Scientific, Cat#Q33216) using Qubit 1x dsDNA HS assay kit (Cat#Q33230). Sample libraries were subsequently pooled and loaded to the Hiseq 2500 (Illumina, serial number SN930). Single end reads at 50bp were generated by using Hiseq rapid SR cluster kit V2 (Illumina, Cat# GD-402-4002) and HiSeq rapid SBS kit v2 50 cycles (Illumina, Cat# FC-402-4022). Faseq files were obtained at Illumina base space (https://basespace.illumina.com) and aligned to Hg38 using Tophat2 (Kim et al., 2013) and resulting BAM files were used to estimate the gene counts using HT-Seq (Anders et al., 2015). Subsequently, to identify differentially expressed genes between CON and NetG1 KO CAFs, we applied DESeq2 (Love et al., 2014). The resulting differentially expressed genes were used as input to GSEA (Subramanian et al., 2005) (default parameters with enrichment statistic set as classic). Heatmap depicting differentially expressed genes using mean-centered rlog transformed gene counts were plotted using pheatmap package available in R. Data is available in the file named: “RNAseq”.

bioRxiv preprint doi: https://doi.org/10.1101/330209; this version posted March 8, 2019. The copyright holder for this preprint (which was not certified by peer review) is the author/funder, who has granted bioRxiv a license to display the preprint in perpetuity. It is made available under aCC-BY-NC-ND 4.0 International license.

Pancreatic Cancer Datasets

We obtained the gene expression data from (Puleo et al., 2018) (processed data available at ArrayExpress ID: E-MTAB-6134), (Moffitt et al., 2015) (processed expression data available at Gene Expression Omnibus ID GSE21501) and TCGA (rsem normalized gene expression data available at GDAC Firehose repository for 76 high tumor purity samples). Clinical outcomes data indicating patient overall survival was obtained from the respective data repositories. In the case of Moffitt and TCGA studies, we used Moffitt *et al.* classification to stratify PDAC tumors into basal and classical subtypes. In the case of Puleo *et al.* we applied 5 different classes as described by that study. Analyses to compare the overall-survival among the basal and classical subtypes were performed by comparing survival curves with log-rank tests. These were calculated using the R 'survival' package Therneau, T. M. & Grambsch, P. M. Modeling Survival Data: Extending the Cox Model (Springer-Verlag, 2010).

Statistics

For all *in vitro* and animal experiments, Prism 7.0 (Graph Pad Software, San Diego, California) was used for all statistical analysis. For comparison between two groups, a two tailed Student's T-Test was performed. For comparisons between more than two groups, a One-Way ANOVA was performed, using either a Dunnett's multiple comparisons test (compared to control condition) or Tukey's multiple comparisons test (comparing all conditions to one another), depending on the experiment. Groups were deemed statistically significantly different from one another if the p-value was less than or equal to 0.05. On graphs, significance was defined as follows: * $P < 0.05$; ** $P < 0.01$; *** < 0.001; **** $P < 0.0001$. For the correlation of the SMI analysis, linear regression was applied to the SMIA generated values of two markers at the designated components, and the R^2 value was calculated. All *in vitro* experiments were performed at least three times (unless explicitly stated in the figure legend) and the orthotopic injections were performed in two cohorts, resulting in N=7 for Control injected mice, and N=19 for combined NGL-1 KO injected mice.

Author Contributions

Conceptualization, E.C., R.F., D.B.V.C.; Methodology, E.C., R.F., J.F.B, I.A., L.G., J.W, T.P., K.S.C., A.M., A.N.L., S.G, K.Q.C., R.T., S.B., M.G.V.H., H.H., E.N., N.S., T.L, S.P., R.T., Y.T.; Validation, T.L., R.F., D.B.V.C, J.W., A.M. D.Ro., D.Re., Y.T.; Formal Analysis, R.F., D.B.V.C, A.M., A.N.L., J.F.B., J.W., T.L., N.S., T.P., K.D., E.M., K.Q.C., E.C., D.Ro., Y.Z., S.P.; Investigation, R.F., D.B.V.C., J.F.B., T.L., N.S., T.P., S.G., L.G., A.M., A.N.L., E.M., H.H.; Resources, E.C., I.A., M.V.H., S.B., W.D.K., W.S.E.D., K.C.; Data Curation; J.F.B., N.S., D.K., Y.Z., D.Ro., T.L, S.P., Y.T.; Writing-original draft, R.F., D.B.V.C.; Writing-review & editing, E.C., I.A., J.W., J.F.B., T.P., S.B., K.S.C., A.M., R.F., D.B.V.C., S.P., M.G.V.H; Visualization, E.C., J.F.B., R.F., D.B.V.C., J.W., A.M., A.N.L., T.P., D.Ro., T.L.; Supervision, E.C., I.A., K.S.C.; Funding Acquisition, E.C., I.A., K.S.C., M.G.V.H.

bioRxiv preprint doi: https://doi.org/10.1101/330209; this version posted March 8, 2019. The copyright holder for this preprint (which was not certified by peer review) is the author/funder, who has granted bioRxiv a license to display the preprint in perpetuity. It is made available under aCC-BY-NC-ND 4.0 International license.

Declaration of Interests

The authors declare no competing interests. M.G.V.H. discloses that he is a consultant and SAB member for Agios Pharmaceuticals, Aeglea Biotherapeutics and Auron Therapeutics.

Acknowledgments

This study is dedicated to the memory of the late P. Keely, who continues to inspire our work. We would like to thank Dr. Martin Humphries for the SNAKA 51 antibody. We appreciate the advice from Dr. Alexander Macfarlane on NK cells and flow cytometry. We thank Jim Oesterling for his great feedback and technical assistance with flow cytometry. We greatly appreciate the NetG1/NGL-1 discussions with Dr. Shigeyoshi Itohara. We are grateful for the kind gifts provided by Robert Weinberg (pBABE-neo-hTERT vector; Addgene plasmid # 1774), Dr. Feng Zhang (LentiCRISPRv2; Addgene plasmid # 52961), Dr. Didier Trono (psPAX2; Addgene plasmid # 12260), Charles Gersbach (pLV hU6-sgRNA hUbC-dCas9-KRAB-T2a-Puro; Addgene plasmid #71236), and Dr. Alexey Ivanov (pLV-CMV-H4-puro vector). This work was supported in part by gifts donated to the memory of Judy Costin, funds from the Martin and Concetta Greenberg Pancreatic cancer Institute, Pennsylvania's DOH Health Research Formula Funds, the Greenfield Foundation, the 5th AHEPA Cancer Research Foundation, Inc., Fox Chase In Vino Vita Institutional Pilot Award, as well as NIH/NCI grants R01CA113451-10 (EC), T32CA009035 (RF), R01CA113451-09S1 (JFB/EC), R21 CA231252 (EC/IA), R01CA188430 (IA), R03CA212949 (IA), R01GM116911 (IA), R01CA194263 (KC) Core grant CA06927 in support to Fox Chase Cancer Center's facilities including: Bio Sample Repository, Light Microscopy, Small Animal Imaging, Biostatistics and Bioinformatics, Flow Cytometry, Laboratory Animal, Cell Culture, DNA sequencing, Genotyping and Real-time PCR and Talbot Library. DOD grant WX81XWH-15-1-0170 (EC/RF/JFB). The authors also acknowledge support from F32CA213810 (AM), the Damon Runyon Cancer Research Foundation (ANL), R01CA168653, R01CA201276, and P30CA1405141 (M.G.V.H), the Lustgarten Foundation (MGVH), the MIT Center for Precision Medicine (MGVH), SU2C (MGVH), and the Ludwig Center at MIT (MGVH). MGVH is a Howard Hughes Medical Institute Faculty Scholar.

References

Amatangelo, M. D., Bassi, D. E., Klein-Szanto, A. J., and Cukierman, E. (2005). Stroma-derived three-dimensional matrices are necessary and sufficient to promote desmoplastic differentiation of normal fibroblasts. Am J Pathol *167*, 475-488.

Anders, S., Pyl, P. T., and Huber, W. (2015). HTSeq--a Python framework to work with high-throughput sequencing data. Bioinformatics *31*, 166-169.

Balsamo, M., Scordamaglia, F., Pietra, G., Manzini, C., Cantoni, C., Boitano, M., Queirolo, P., Vermi, W., Facchetti, F., Moretta, A.*, et al.* (2009). Melanoma-associated fibroblasts modulate NK cell phenotype and antitumor cytotoxicity. Proc Natl Acad Sci U S A *106*, 20847-20852.

Basso, D., Gnatta, E., and Plebani, M. (2014). Pancreatic Cancer Fostered Immunosuppression Privileges Tumor Growth and Progression. Journal of Clinical & Cellular Immunology, 16.

Beglyarova, N., Banina, E., Zhou, Y., Mukhamadeeva, R., Andrianov, G., Bobrov, E., Lysenko, E., Skobeleva, N., Gabitova, L., Restifo, D.*, et al.* (2016). Screening of Conditionally Reprogrammed Patient-Derived Carcinoma Cells Identifies ERCC3-MYC Interactions as a Target in Pancreatic Cancer. Clin Cancer Res *22*, 6153-6163.

bioRxiv preprint doi: https://doi.org/10.1101/330209; this version posted March 8, 2019. The copyright holder for this preprint (which was not certified by peer review) is the author/funder, who has granted bioRxiv a license to display the preprint in perpetuity. It is made available under aCC-BY-NC-ND 4.0 International license.

Biancur, D. E., Paulo, J. A., Malachowska, B., Quiles Del Rey, M., Sousa, C. M., Wang, X., Sohn, A. S. W., Chu, G. C., Gygi, S. P., Harper, J. W.*, et al.* (2017). Compensatory metabolic networks in pancreatic cancers upon perturbation of glutamine metabolism. Nat Commun *8*, 15965.
Buck, M. D., Sowell, R. T., Kaech, S. M., and Pearce, E. L. (2017). Metabolic Instruction of Immunity. Cell *169*, 570-586.
Campbell, P. M., Groehler, A. L., Lee, K. M., Ouellette, M. M., Khazak, V., and Der, C. J. (2007). K-Ras promotes growth transformation and invasion of immortalized human pancreatic cells by Raf and phosphatidylinositol 3-kinase signaling. Cancer Res *67*, 2098-2106.
Cancer Genome Atlas Research Network. Electronic address, a. a. d. h. e., and Cancer Genome Atlas Research, N. (2017). Integrated Genomic Characterization of Pancreatic Ductal Adenocarcinoma. Cancer Cell *32*, 185-203 e113.
Castro-Bello, F., Ramos, F., Vivanco, F., and Marina-Fiol, C. (1976). High serum glutamic acid levels in patients with carcinoma of the pancreas. Digestion *14*, 360-363.
Cerami, E., Gao, J., Dogrusoz, U., Gross, B. E., Sumer, S. O., Aksoy, B. A., Jacobsen, A., Byrne, C. J., Heuer, M. L., Larsson, E.*, et al.* (2012). The cBio cancer genomics portal: an open platform for exploring multidimensional cancer genomics data. Cancer Discov *2*, 401-404.
Chalmers, Z. R., Connelly, C. F., Fabrizio, D., Gay, L., Ali, S. M., Ennis, R., Schrock, A., Campbell, B., Shlien, A., Chmielecki, J.*, et al.* (2017). Analysis of 100,000 human cancer genomes reveals the landscape of tumor mutational burden. Genome Med *9*, 34.
Chan, T. S., Hsu, C. C., Pai, V. C., Liao, W. Y., Huang, S. S., Tan, K. T., Yen, C. J., Hsu, S. C., Chen, W. Y., Shan, Y. S.*, et al.* (2016). Metronomic chemotherapy prevents therapy-induced stromal activation and induction of tumor-initiating cells. J Exp Med *213*, 2967-2988.
Clark, C. E., Hingorani, S. R., Mick, R., Combs, C., Tuveson, D. A., and Vonderheide, R. H. (2007). Dynamics of the immune reaction to pancreatic cancer from inception to invasion. Cancer Res *67*, 9518-9527.
Costa, A., Kieffer, Y., Scholer-Dahirel, A., Pelon, F., Bourachot, B., Cardon, M., Sirven, P., Magagna, I., Fuhrmann, L., Bernard, C.*, et al.* (2018). Fibroblast Heterogeneity and Immunosuppressive Environment in Human Breast Cancer. Cancer Cell *33*, 463-479 e410.
Costea, D. E., Hills, A., Osman, A. H., Thurlow, J., Kalna, G., Huang, X., Pena Murillo, C., Parajuli, H., Suliman, S., Kulasekara, K. K.*, et al.* (2013). Identification of two distinct carcinoma-associated fibroblast subtypes with differential tumor-promoting abilities in oral squamous cell carcinoma. Cancer Res *73*, 3888-3901.
Cukierman, E., Pankov, R., Stevens, D. R., and Yamada, K. M. (2001). Taking cell-matrix adhesions to the third dimension. Science *294*, 1708-1712.
Deguine, J., Breart, B., Lemaitre, F., Di Santo, J. P., and Bousso, P. (2010). Intravital imaging reveals distinct dynamics for natural killer and CD8(+) T cells during tumor regression. Immunity *33*, 632-644.
Djurec, M., Grana, O., Lee, A., Troule, K., Espinet, E., Cabras, L., Navas, C., Blasco, M. T., Martin-Diaz, L., Burdiel, M.*, et al.* (2018). Saa3 is a key mediator of the protumorigenic properties of cancer-associated fibroblasts in pancreatic tumors. Proc Natl Acad Sci U S A *115*, E1147-E1156.
Ene-Obong, A., Clear, A. J., Watt, J., Wang, J., Fatah, R., Riches, J. C., Marshall, J. F., Chin-Aleong, J., Chelala, C., Gribben, J. G.*, et al.* (2013). Activated pancreatic stellate cells sequester CD8+ T cells to reduce their infiltration of the juxtatumoral compartment of pancreatic ductal adenocarcinoma. Gastroenterology *145*, 1121-1132.
Erkan, M., Kurtoglu, M., and Kleeff, J. (2016). The role of hypoxia in pancreatic cancer: a potential therapeutic target? Expert Rev Gastroenterol Hepatol *10*, 301-316.
Erkan, M., Michalski, C. W., Rieder, S., Reiser-Erkan, C., Abiatari, I., Kolb, A., Giese, N. A., Esposito, I., Friess, H., and Kleeff, J. (2008). The activated stroma index is a novel and

bioRxiv preprint doi: https://doi.org/10.1101/330209; this version posted March 8, 2019. The copyright holder for this preprint (which was not certified by peer review) is the author/funder, who has granted bioRxiv a license to display the preprint in perpetuity. It is made available under aCC-BY-NC-ND 4.0 International license.

independent prognostic marker in pancreatic ductal adenocarcinoma. Clin Gastroenterol Hepatol *6*, 1155-1161.
Evans, R. A., Diamond, M. S., Rech, A. J., Chao, T., Richardson, M. W., Lin, J. H., Bajor, D. L., Byrne, K. T., Stanger, B. Z., Riley, J. L.*, et al.* (2016). Lack of immunoediting in murine pancreatic cancer reversed with neoantigen. JCI Insight *1*.
Franco-Barraza, J., Beacham, D. A., Amatangelo, M. D., and Cukierman, E. (2016). Preparation of Extracellular Matrices Produced by Cultured and Primary Fibroblasts. Curr Protoc Cell Biol *71*, 10 19 11-10 19 34.
Franco-Barraza, J., Francescone, R., Luong, T., Shah, N., Madhani, R., Cukierman, G., Dulaimi, E., Devarajan, K., Egleston, B. L., Nicolas, E.*, et al.* (2017). Matrix-regulated integrin alphavbeta5 maintains alpha5beta1-dependent desmoplastic traits prognostic of neoplastic recurrence. Elife *6*.
Fu, Y., Liu, S., Zeng, S., and Shen, H. (2018). The critical roles of activated stellate cells-mediated paracrine signaling, metabolism and onco-immunology in pancreatic ductal adenocarcinoma. Mol Cancer *17*, 62.
Galic, M. A., Riazi, K., and Pittman, Q. J. (2012). Cytokines and brain excitability. Front Neuroendocrinol *33*, 116-125.
Gao, J., Aksoy, B. A., Dogrusoz, U., Dresdner, G., Gross, B., Sumer, S. O., Sun, Y., Jacobsen, A., Sinha, R., Larsson, E.*, et al.* (2013). Integrative analysis of complex cancer genomics and clinical profiles using the cBioPortal. Sci Signal *6*, pl1.
Gardiner, C. M., and Finlay, D. K. (2017). What Fuels Natural Killers? Metabolism and NK Cell Responses. Front Immunol *8*, 367.
Haroon, E., Miller, A. H., and Sanacora, G. (2017). Inflammation, Glutamate, and Glia: A Trio of Trouble in Mood Disorders. Neuropsychopharmacology *42*, 193-215.
Harper, J., and Sainson, R. C. (2014). Regulation of the anti-tumour immune response by cancer-associated fibroblasts. Semin Cancer Biol *25*, 69-77.
Heneberg, P. (2016). Paracrine tumor signaling induces transdifferentiation of surrounding fibroblasts. Critical reviews in oncology/hematology *97*, 303-311.
Hidalgo, M. (2010). Pancreatic cancer. N Engl J Med *362*, 1605-1617.
Hingorani, S. R., Petricoin, E. F., Maitra, A., Rajapakse, V., King, C., Jacobetz, M. A., Ross, S., Conrads, T. P., Veenstra, T. D., Hitt, B. A.*, et al.* (2003). Preinvasive and invasive ductal pancreatic cancer and its early detection in the mouse. Cancer Cell *4*, 437-450.
Hingorani, S. R., Wang, L., Multani, A. S., Combs, C., Deramaudt, T. B., Hruban, R. H., Rustgi, A. K., Chang, S., and Tuveson, D. A. (2005). Trp53R172H and KrasG12D cooperate to promote chromosomal instability and widely metastatic pancreatic ductal adenocarcinoma in mice. Cancer Cell *7*, 469-483.
Horlbeck, M. A., Gilbert, L. A., Villalta, J. E., Adamson, B., Pak, R. A., Chen, Y., Fields, A. P., Park, C. Y., Corn, J. E., Kampmann, M., and Weissman, J. S. (2016). Compact and highly active next-generation libraries for CRISPR-mediated gene repression and activation. Elife *5*.
Hwang, R. F., Moore, T., Arumugam, T., Ramachandran, V., Amos, K. D., Rivera, A., Ji, B., Evans, D. B., and Logsdon, C. D. (2008). Cancer-associated stromal fibroblasts promote pancreatic tumor progression. Cancer Res *68*, 918-926.
Jiang, H., Hegde, S., Knolhoff, B. L., Zhu, Y., Herndon, J. M., Meyer, M. A., Nywening, T. M., Hawkins, W. G., Shapiro, I. M., Weaver, D. T.*, et al.* (2016). Targeting focal adhesion kinase renders pancreatic cancers responsive to checkpoint immunotherapy. Nat Med *22*, 851-860.
Jin, L., Alesi, G. N., and Kang, S. (2016). Glutaminolysis as a target for cancer therapy. Oncogene *35*, 3619-3625.
Kamphorst, J. J., Nofal, M., Commisso, C., Hackett, S. R., Lu, W., Grabocka, E., Vander Heiden, M. G., Miller, G., Drebin, J. A., Bar-Sagi, D.*, et al.* (2015). Human pancreatic cancer tumors are nutrient poor and tumor cells actively scavenge extracellular protein. Cancer Res *75*, 544-553.

bioRxiv preprint doi: https://doi.org/10.1101/330209; this version posted March 8, 2019. The copyright holder for this preprint (which was not certified by peer review) is the author/funder, who has granted bioRxiv a license to display the preprint in perpetuity. It is made available under aCC-BY-NC-ND 4.0 International license.

Kim, D., Pertea, G., Trapnell, C., Pimentel, H., Kelley, R., and Salzberg, S. L. (2013). TopHat2: accurate alignment of transcriptomes in the presence of insertions, deletions and gene fusions. Genome Biol *14*, R36.
Kim, E. J., Sahai, V., Abel, E. V., Griffith, K. A., Greenson, J. K., Takebe, N., Khan, G. N., Blau, J. L., Craig, R., Balis, U. G.*, et al.* (2014). Pilot clinical trial of hedgehog pathway inhibitor GDC-0449 (vismodegib) in combination with gemcitabine in patients with metastatic pancreatic adenocarcinoma. Clin Cancer Res *20*, 5937-5945.
Kouidhi, S., Ben Ayed, F., and Benammar Elgaaied, A. (2018). Targeting Tumor Metabolism: A New Challenge to Improve Immunotherapy. Front Immunol *9*, 353.
Kumar, V., Donthireddy, L., Marvel, D., Condamine, T., Wang, F., Lavilla-Alonso, S., Hashimoto, A., Vonteddu, P., Behera, R., Goins, M. A.*, et al.* (2017). Cancer-Associated Fibroblasts Neutralize the Anti-tumor Effect of CSF1 Receptor Blockade by Inducing PMN-MDSC Infiltration of Tumors. Cancer Cell *32*, 654-668 e655.
Li, L., and Hanahan, D. (2013). Hijacking the neuronal NMDAR signaling circuit to promote tumor growth and invasion. Cell *153*, 86-100.
Li, T., Yang, Y., Hua, X., Wang, G., Liu, W., Jia, C., Tai, Y., Zhang, Q., and Chen, G. (2012). Hepatocellular carcinoma-associated fibroblasts trigger NK cell dysfunction via PGE2 and IDO. Cancer Lett *318*, 154-161.
Li, T., Yi, S., Liu, W., Jia, C., Wang, G., Hua, X., Tai, Y., Zhang, Q., and Chen, G. (2013). Colorectal carcinoma-derived fibroblasts modulate natural killer cell phenotype and antitumor cytotoxicity. Med Oncol *30*, 663.
Liguz-Lecznar, M., and Skangiel-Kramska, J. (2007). Vesicular glutamate transporters (VGLUTs): the three musketeers of glutamatergic system. Acta Neurobiol Exp (Wars) *67*, 207-218.
Lin, J. C., Ho, W. H., Gurney, A., and Rosenthal, A. (2003). The netrin-G1 ligand NGL-1 promotes the outgrowth of thalamocortical axons. Nat Neurosci *6*, 1270-1276.
Love, M. I., Huber, W., and Anders, S. (2014). Moderated estimation of fold change and dispersion for RNA-seq data with DESeq2. Genome Biol *15*, 550.
Lyssiotis, C. A., and Kimmelman, A. C. (2017). Metabolic Interactions in the Tumor Microenvironment. Trends Cell Biol *27*, 863-875.
Matsukawa, H., Akiyoshi-Nishimura, S., Zhang, Q., Lujan, R., Yamaguchi, K., Goto, H., Yaguchi, K., Hashikawa, T., Sano, C., Shigemoto, R.*, et al.* (2014). Netrin-G/NGL complexes encode functional synaptic diversification. J Neurosci *34*, 15779-15792.
McCarroll, J. A., Naim, S., Sharbeen, G., Russia, N., Lee, J., Kavallaris, M., Goldstein, D., and Phillips, P. A. (2014). Role of pancreatic stellate cells in chemoresistance in pancreatic cancer. Front Physiol *5*, 141.
Merico, D., Isserlin, R., Stueker, O., Emili, A., and Bader, G. D. (2010). Enrichment map: a network-based method for gene-set enrichment visualization and interpretation. PLoS One *5*, e13984.
Moffitt, R. A., Marayati, R., Flate, E. L., Volmar, K. E., Loeza, S. G., Hoadley, K. A., Rashid, N. U., Williams, L. A., Eaton, S. C., Chung, A. H.*, et al.* (2015). Virtual microdissection identifies distinct tumor- and stroma-specific subtypes of pancreatic ductal adenocarcinoma. Nat Genet *47*, 1168-1178.
Muir, A., Danai, L. V., Gui, D. Y., Waingarten, C. Y., Lewis, C. A., and Vander Heiden, M. G. (2017). Environmental cystine drives glutamine anaplerosis and sensitizes cancer cells to glutaminase inhibition. Elife *6*.
Muranen, T., Iwanicki, M. P., Curry, N. L., Hwang, J., DuBois, C. D., Coloff, J. L., Hitchcock, D. S., Clish, C. B., Brugge, J. S., and Kalaany, N. Y. (2017). Starved epithelial cells uptake extracellular matrix for survival. Nat Commun *8*, 13989.

bioRxiv preprint doi: https://doi.org/10.1101/330209; this version posted March 8, 2019. The copyright holder for this preprint (which was not certified by peer review) is the author/funder, who has granted bioRxiv a license to display the preprint in perpetuity. It is made available under aCC-BY-NC-ND 4.0 International license.

Nakashiba, T., Ikeda, T., Nishimura, S., Tashiro, K., Honjo, T., Culotti, J. G., and Itohara, S. (2000). Netrin-G1: a novel glycosyl phosphatidylinositol-linked mammalian netrin that is functionally divergent from classical netrins. J Neurosci *20*, 6540-6550.
Ohlund, D., Elyada, E., and Tuveson, D. (2014). Fibroblast heterogeneity in the cancer wound. J Exp Med *211*, 1503-1523.
Ohlund, D., Handly-Santana, A., Biffi, G., Elyada, E., Almeida, A. S., Ponz-Sarvise, M., Corbo, V., Oni, T. E., Hearn, S. A., Lee, E. J.*, et al.* (2017). Distinct populations of inflammatory fibroblasts and myofibroblasts in pancreatic cancer. J Exp Med *214*, 579-596.
Olive, K. P., Jacobetz, M. A., Davidson, C. J., Gopinathan, A., McIntyre, D., Honess, D., Madhu, B., Goldgraben, M. A., Caldwell, M. E., Allard, D.*, et al.* (2009). Inhibition of Hedgehog signaling enhances delivery of chemotherapy in a mouse model of pancreatic cancer. Science *324*, 1457-1461.
Özdemir BC, P.-H. T., Carstens JL, Zheng X, Wu CC, Simpson TR, Laklai H, Sugimoto H, Kahlert C, Novitskiy SV, De Jesus-Acosta A, Sharma P, Heidari P, Mahmood U, Chin L, Moses HL, Weaver VM, Maitra A, Allison JP, LeBleu VS, Kalluri R. (2014). Depletion of carcinoma-associated fibroblasts and fibrosis induces immunosuppression and accelerates pancreas cancer with reduced survival. Cancer Cell *25*, 719-734.
Provenzano, P. P., Cuevas, C., Chang, A. E., Goel, V. K., Von Hoff, D. D., and Hingorani, S. R. (2012). Enzymatic targeting of the stroma ablates physical barriers to treatment of pancreatic ductal adenocarcinoma. Cancer Cell *21*, 418-429.
Puleo, F., Nicolle, R., Blum, Y., Cros, J., Marisa, L., Demetter, P., Quertinmont, E., Svrcek, M., Elarouci, N., Iovanna, J.*, et al.* (2018). Stratification of Pancreatic Ductal Adenocarcinomas Based on Tumor and Microenvironment Features. Gastroenterology *155*, 1999-2013 e1993.
Rahib, L., Smith, B. D., Aizenberg, R., Rosenzweig, A. B., Fleshman, J. M., and Matrisian, L. M. (2014). Projecting cancer incidence and deaths to 2030: the unexpected burden of thyroid, liver, and pancreas cancers in the United States. Cancer Res *74*, 2913-2921.
Renner, K., Singer, K., Koehl, G. E., Geissler, E. K., Peter, K., Siska, P. J., and Kreutz, M. (2017). Metabolic Hallmarks of Tumor and Immune Cells in the Tumor Microenvironment. Front Immunol *8*, 248.
Rezakhaniha, R., Agianniotis, A., Schrauwen, J. T., Griffa, A., Sage, D., Bouten, C. V., van de Vosse, F. N., Unser, M., and Stergiopulos, N. (2012). Experimental investigation of collagen waviness and orientation in the arterial adventitia using confocal laser scanning microscopy. Biomech Model Mechanobiol *11*, 461-473.
Rhim, A. D., Oberstein, P. E., Thomas, D. H., Mirek, E. T., Palermo, C. F., Sastra, S. A., Dekleva, E. N., Saunders, T., Becerra, C. P., Tattersall, I. W.*, et al.* (2014). Stromal elements act to restrain, rather than support, pancreatic ductal adenocarcinoma. Cancer Cell *25*, 735-747.
Ricci, F., Kern, S. E., Hruban, R. H., and Iacobuzio-Donahue, C. A. (2005). Stromal responses to carcinomas of the pancreas: juxtatumoral gene expression conforms to the infiltrating pattern and not the biologic subtype. Cancer Biol Ther *4*, 302-307.
Ritchie, M. E., Phipson, B., Wu, D., Hu, Y., Law, C. W., Shi, W., and Smyth, G. K. (2015). limma powers differential expression analyses for RNA-sequencing and microarray studies. Nucleic Acids Res *43*, e47.
Roux, C., Riganti, C., Borgogno, S. F., Curto, R., Curcio, C., Catanzaro, V., Digilio, G., Padovan, S., Puccinelli, M. P., Isabello, M.*, et al.* (2017). Endogenous glutamine decrease is associated with pancreatic cancer progression. Oncotarget *8*, 95361-95376.
Ryan, D. P., Hong, T. S., and Bardeesy, N. (2014). Pancreatic adenocarcinoma. N Engl J Med *371*, 2140-2141.
Sanjana, N. E., Shalem, O., and Zhang, F. (2014). Improved vectors and genome-wide libraries for CRISPR screening. Nat Methods *11*, 783-784.
Seo, J. W., Choi, J., Lee, S. Y., Sung, S., Yoo, H. J., Kang, M. J., Cheong, H., and Son, J. (2016). Autophagy is required for PDAC glutamine metabolism. Sci Rep *6*, 37594.

bioRxiv preprint doi: https://doi.org/10.1101/330209; this version posted March 8, 2019. The copyright holder for this preprint (which was not certified by peer review) is the author/funder, who has granted bioRxiv a license to display the preprint in perpetuity. It is made available under aCC-BY-NC-ND 4.0 International license.

Siegel, R. L., Miller, K. D., and Jemal, A. (2019). Cancer statistics, 2019. CA Cancer J Clin *69*, 7-34.
Son, J., Lyssiotis, C. A., Ying, H., Wang, X., Hua, S., Ligorio, M., Perera, R. M., Ferrone, C. R., Mullarky, E., Shyh-Chang, N.*, et al.* (2013). Glutamine supports pancreatic cancer growth through a KRAS-regulated metabolic pathway. Nature *496*, 101-105.
Song, Y. S., Lee, H. J., Prosselkov, P., Itohara, S., and Kim, E. (2013). Trans-induced cis interaction in the tripartite NGL-1, netrin-G1 and LAR adhesion complex promotes development of excitatory synapses. J Cell Sci *126*, 4926-4938.
Sousa, C. M., Biancur, D. E., Wang, X., Halbrook, C. J., Sherman, M. H., Zhang, L., Kremer, D., Hwang, R. F., Witkiewicz, A. K., Ying, H.*, et al.* (2016). Pancreatic stellate cells support tumour metabolism through autophagic alanine secretion. Nature *536*, 479-483.
Subramanian, A., Tamayo, P., Mootha, V. K., Mukherjee, S., Ebert, B. L., Gillette, M. A., Paulovich, A., Pomeroy, S. L., Golub, T. R., Lander, E. S., and Mesirov, J. P. (2005). Gene set enrichment analysis: a knowledge-based approach for interpreting genome-wide expression profiles. Proc Natl Acad Sci U S A *102*, 15545-15550.
Takeuchi, S., Baghdadi, M., Tsuchikawa, T., Wada, H., Nakamura, T., Abe, H., Nakanishi, S., Usui, Y., Higuchi, K., Takahashi, M.*, et al.* (2015). Chemotherapy-Derived Inflammatory Responses Accelerate the Formation of Immunosuppressive Myeloid Cells in the Tissue Microenvironment of Human Pancreatic Cancer. Cancer Res *75*, 2629-2640.
Thakore, P. I., D'Ippolito, A. M., Song, L., Safi, A., Shivakumar, N. K., Kabadi, A. M., Reddy, T. E., Crawford, G. E., and Gersbach, C. A. (2015). Highly specific epigenome editing by CRISPR-Cas9 repressors for silencing of distal regulatory elements. Nat Methods *12*, 1143-1149.
Trotta, R., Dal Col, J., Yu, J., Ciarlariello, D., Thomas, B., Zhang, X., Allard, J., 2nd, Wei, M., Mao, H., Byrd, J. C.*, et al.* (2008). TGF-beta utilizes SMAD3 to inhibit CD16-mediated IFN-gamma production and antibody-dependent cellular cytotoxicity in human NK cells. J Immunol *181*, 3784-3792.
Vaheri, A., Enzerink, A., Rasanen, K., and Salmenpera, P. (2009). Nemosis, a novel way of fibroblast activation, in inflammation and cancer. Exp Cell Res *315*, 1633-1638.
Van Audenaerde, J. R. M., De Waele, J., Marcq, E., Van Loenhout, J., Lion, E., Van den Bergh, J. M. J., Jesenofsky, R., Masamune, A., Roeyen, G., Pauwels, P.*, et al.* (2017). Interleukin-15 stimulates natural killer cell-mediated killing of both human pancreatic cancer and stellate cells. Oncotarget *8*, 56968-56979.
Van Audenaerde, J. R. M., Roeyen, G., Darcy, P. K., Kershaw, M. H., Peeters, M., and Smits, E. L. J. (2018). Natural Killer cells and their therapeutic role in pancreatic cancer: A systematic review. Pharmacol Ther.
Vesce, S., Rossi, D., Brambilla, L., and Volterra, A. (2007). Glutamate release from astrocytes in physiological conditions and in neurodegenerative disorders characterized by neuroinflammation. Int Rev Neurobiol *82*, 57-71.
von Ahrens, D., Bhagat, T. D., Nagrath, D., Maitra, A., and Verma, A. (2017). The role of stromal cancer-associated fibroblasts in pancreatic cancer. J Hematol Oncol *10*, 76.
Wu, Q., Tian, Y., Zhang, J., Zhang, H., Gu, F., Lu, Y., Zou, S., Chen, Y., Sun, P., Xu, M.*, et al.* (2017). Functions of pancreatic stellate cell-derived soluble factors in the microenvironment of pancreatic ductal carcinoma. Oncotarget *8*, 102721-102738.
Xiang, Y., Stine, Z. E., Xia, J., Lu, Y., O'Connor, R. S., Altman, B. J., Hsieh, A. L., Gouw, A. M., Thomas, A. G., Gao, P.*, et al.* (2015). Targeted inhibition of tumor-specific glutaminase diminishes cell-autonomous tumorigenesis. J Clin Invest *125*, 2293-2306.
Yang, L., Achreja, A., Yeung, T. L., Mangala, L. S., Jiang, D., Han, C., Baddour, J., Marini, J. C., Ni, J., Nakahara, R.*, et al.* (2016). Targeting Stromal Glutamine Synthetase in Tumors Disrupts Tumor Microenvironment-Regulated Cancer Cell Growth. Cell Metab *24*, 685-700.
Yarchoan, M., Hopkins, A., and Jaffee, E. M. (2017). Tumor Mutational Burden and Response Rate to PD-1 Inhibition. N Engl J Med *377*, 2500-2501.

bioRxiv preprint doi: https://doi.org/10.1101/330209; this version posted March 8, 2019. The copyright holder for this preprint (which was not certified by peer review) is the author/funder, who has granted bioRxiv a license to display the preprint in perpetuity. It is made available under aCC-BY-NC-ND 4.0 International license.

Zhao, H., Yang, L., Baddour, J., Achreja, A., Bernard, V., Moss, T., Marini, J. C., Tudawe, T., Seviour, E. G., San Lucas, F. A., *et al.* (2016). Tumor microenvironment derived exosomes pleiotropically modulate cancer cell metabolism. Elife *5*, e10250.

Figure Legends

Figure 1. *NetG1 is upregulated in CAFs compared to patient matched PSCs*. **A.** Heatmap representing increased (red) or decreased (blue) gene expression levels between patient derived PSCs and CAFs. Position of NetG1 in the heatmap is represented with arrow. **B.** Pathways that are significantly enriched between these two cell types are represented as network map. Each node (circle) represent a pathway while the edges (lines) connecting nodes show shared genes between pathways with thickness of edge corresponds to degree of sharing. Color of node indicate positive (red) or negative (blue) enrichment in CAF cells. Enrichment of select pathways are shown as GSEA enrichment plots with positive (**C**) and negative (**D**) enrichment in CAFs.

Figure 2. *NetG1 is highly expressed in the stroma, while NGL-1 is up-regulated in the epithelia of PDAC patients.* **A.** Representative images of simultaneous multi-channel immunofluorescent (SMI) approach, performed on formalin fixed paraffin embedded tissue samples corresponding either to normal pancreatic tissue (normal human pancreas), normal tissue adjacent to PDAC tumor (tumor adjacent), or PDAC tumor tissue (tumor) from patient/donor surgical samples. Upper row panels show merged and pseudo-colored images corresponding to the three locations used as "gating masks." These masks correspond to pan-cytokeratins positive areas in purple demarking epithelial/tumoral compartment, vimentin regions in cyan and DRAQ5 for nuclei in yellow. The SMIA-CUKIE algorithm (described in Material and Methods) was instructed to render an intersection "mask" image corresponding to vimentin positive epithelial/tumoral negative areas (S-stroma in upper panels inserts), whereas epi/tumor positive masks omitted all vimentin positive pixels. The two above-mentioned masks were used as areas to generate the images shown in the medium and lower rows, which are magnified images corresponding to the regions of interest highlighted in upper row images within white squares and asterisks. Medium row show "markers" in stromal areas corresponding to NetG1 and pFAK, while lower row shows NGL-1 at tumor areas. Lower left corner panels indicate the algorithm generated area "masks" used (S-epi/tumor; S/stroma). Representative scale bars are provided for each magnification **B.** Graphs depict integrated intensities of stromal NetG1, stromal pFAK, or epithelial NGL-1 staining in normal (N= 6), tumor adjacent (N= 4), or tumor (N= 15) pancreatic tissue. One-Way ANOVA, Dunnett's multiple comparison test. *$p<0.05$, **$p<0.01$, ***$p<0.001$; ****$p<0.0001$. **C. (LEFT)** Linear regression analysis comparing expression of stromal pFAK with stromal NetG1 and **(RIGHT)** epithelial NGL-1 with stromal NetG1. Each dot represents the integrated intensity of each parameter from a single image; colored dots are as indicated in **B**. P-values are shown in black and R^2 values are shown in red. **D.** Representative western blot comparing NetG1 expression in 4 PSCs and 5 CAFs obtained from PDAC patient tissues, with the respective quantifications normalized to GAPDH and mean PSC expression. **E.** Representative western blot comparing NGL-1 expression in cell lines derived from PDAC PDX models. H3 was used as a loading control. **F.** Representative western blot comparing NGL-1 expression in an isogenic cell line of human pancreatic epithelial cells (HPNE system) with progressive mutations, simulating different stages of pancreatic cancer. hTERT = immortalized epithelia; E6/E7 = Rb and P53 inactivated hTERT cells; PDACc = E6/E7 cells with $KRAS^{G12D}$. H3 was used as a loading control.

bioRxiv preprint doi: https://doi.org/10.1101/330209; this version posted March 8, 2019. The copyright holder for this preprint (which was not certified by peer review) is the author/funder, who has granted bioRxiv a license to display the preprint in perpetuity. It is made available under aCC-BY-NC-ND 4.0 International license.

Figure 3. *CAFs support PDAC survival under metabolically stressed conditions in a NetG1/NGL-1 dependent manner*
A. RFP$^+$ CON or NGL-1 KO PDACc (2x10^4) were co-cultured in 3D with GFP$^+$ CON or NetG1 KO CAFs (2x10^4) (2 clones, KO1 and KO2) or alone in the absence of serum and Gln for 4 days followed by cell survival assessments. * compared to CON PDACc/CON CAF. **B.** Same assay as in (**A**), but with RFP$^+$ CON or NGL-1 KO PANC-1 cells. * compared to CON PANC-1/CON CAF. **C.** RFP$^+$ CON or NGL-1 KO PDACc (2x10^4) were co-cultured in 3D with CM from CON, NetG1 KO CAFs, or PSCs in SF/Gln free media, and PDACc survival was measured after 4 days. * compared to CON PDACc/CON CAF. **D.** RFP$^+$ CON PDACc (2x10^4) were grown in 3D in the indicated fibroblast derived ECMs alone in the absence of serum and Gln for 4 days and PDAC cell survival was measured. * compared to CON PDACc/CON CAF. **E.** Relative glutamate and glutamine levels in the CM of PSCs and CON or NetG1 KO CAFs. N= 6 biological replicates, all groups were compared to PSC condition. **F.** RFP$^+$ CON or NGL-1 KO PDACc (2x10^4) were cultured alone in 3D under serum and Gln deprivation (-). Graph depicts relative PDACc survival after exposure to media alone, Glu, Gln, or CAF CM. Treatment groups consisted of Glu (150 µM) and Gln (25 µM) addbacks to determine if those amino acids alone could rescue PDAC cell survival in the absence of CAFs. CM from CON CAFs was used as a positive control for rescue. Note how amino acids alone partially rescue CON PDACc but not NGL-1 KO PDACc, which also benefit from CM media to a lesser extent than their CON counterparts. * compared to CON PDACc alone; # compared to KO PDACc alone. All Graphs: One-Way ANOVA, Dunnett's multiple comparison test. *p<0.05, **p<0.01, ***p<0.001; ****p<0.0001.

Figure 4. *NetG1, VGlut1, and GS regulate Glu/Gln levels in CAFs and support PDAC survival in co-culture.* **A.** Representative western blots of glutaminase (GLS), glutamine synthetase (GS) and vesicular glutamate transporter 1 (VGlut1) in PSCs (N), control CAFs (C) and NetG1 KO CAFs (KO). H3 was used as a loading control. **B.** Representative western blots of GLS and GS in control CAFs (C) and NetG1 KO CAFs (KO) in comparison to CON and NGL-1 KO PDACc. H3 was used as a loading control. **C. (LEFT)** Representative western blots of VGlut1 in CAFs, demonstrating effective knockdown (KD) by CRISPRi. **(RIGHT)** Representative western blots of NetG1, GLS, and GS in PSCs, CON, or VGlut1 KD CAFs. GAPDH was used as a loading control. **D.** Relative Glu and Gln levels in the CM of NetG1 and VGlut1 KD CAFs compared to CON CAF. Note that both NetG1 KD and VGlut1 KD CAFs have a reduction in Glu/Gln levels. * Compared to CON CAF. **E.** RFP$^+$ CON or NGL-1 KO PDACc (2x10^4) were cultured in 3D with CON or VGlut1 KD CAFs (2x10^4) for 96 hours in SF/Gln Free media and cell survival was assessed. **F.** RFP$^+$ CON or NGL-1 KO PDAC (2x10^4) were cultured, using 3D conditions as before, for 96 hours in SF/Gln Free media with CON or NetG1 KO CAFs (2x10^4) that were pre-treated 24 hours with vehicle (water) a GS inhibitor (1 mM methionine sulfoximine) and PDAC survival was evaluated. For all graphs: One-Way ANOVA, Dunnett's multiple comparison test. *p<0.05, **p<0.01, ***p<0.001; ****p<0.0001.

Figure 5. *NetG1$^+$ CAFs create an immunosuppressive microenvironment that protects PDAC cells from NK cell induced death.* **A.** Quantification of U-Plex (multiplex ELISA; GM-CSF, IL-1β, CCL20, IL-6, IL-8) and ELISAs (IL-15, TGF-β) of assorted cytokines with immunomodulatory or immunoattractive potentials, detected in the CM of PSCs, CON CAFs, or NetG1 KO CAFs, growing in 3D. N= 6 biological replicates. * compared to PSCs. **B.** Quantification of the % of NK-92 cells positive for markers of activation (IFNγ and Granzyme B) determined by flow cytometry after IL-2 pre-activated NK-92 cells (8x10^4) were in direct co-culture (CC) with CON or NetG1 KO

bioRxiv preprint doi: https://doi.org/10.1101/330209; this version posted March 8, 2019. The copyright holder for this preprint (which was not certified by peer review) is the author/funder, who has granted bioRxiv a license to display the preprint in perpetuity. It is made available under aCC-BY-NC-ND 4.0 International license.

CAFs ($2x10^4$) or treated with their conditioned media (CM) for 16 hours. * compared to CON CAF CC. **C.** Primary NK cells (10^5) were isolated from healthy human donors, pre-activated with IL-2/IL-12, incubated with CM from CON or NetG1 KO CAFs for 16 hours, and their activation status was determined by flow cytometry, using IFNγ and CD69 as markers. Expression of markers was normalized to the positive control (IL-2 alone = 1.0). * comparison between the CON and KO at each % of CM. **D.** RFP^+ CON or NGL-1 KO PDACc ($2x10^4$) were co-cultured in 3D with GFP^+ CON or NetG1 KO CAFs ($2x10^4$) and with active **(LEFT)** or resting **(RIGHT)** NK-92 cells ($8x10^4$) for 48 hours and PDAC survival was quantified. Groups were normalized to CON PDACc/CON CAF with active NK cells. Dotted line in the resting graph **(RIGHT)** denotes PDACc survival with CON PDACc/CON CAF with active NK cells. * compared to CON PDACc/CON CAF with active NK cells. One-Way ANOVA, Dunnett's multiple comparison test **(A, B, D)** or T-test **(C).** *p<0.05, **p<0.01, ***p<0.001; ****p<0.0001.

Figure 6. *IL-15, VGlut1, and GS are regulators of CAF induced immunosuppression*. **A.** NK cell killing assay in 2D, where RFP^+ CON or NGL-1 KO PDACc ($2x10^4$) were co-cultured with CON or NetG1 KO CAFs ($2x10^4$) and $8x10^4$ active NK-92 cells (IL-2 preactivated) for 6 hours in the presence of isotype control IgG or IL-15 neutralizing antibody. Graphs depict PDACc survival, relative to the CON PDACc/CON CAF condition treated with IgG (dotted green line). * compared to IgG treated CON PDACc/CON CAF with NK cells. **B.** Same assay as in (**A**), but the co-culture is performed in 3D for 48 hours. * compared to IgG treated CON PDACc/CON CAF with NK cells. **C.** CON and VGlut1 KD CAFs were grown in 3D and allowed to generate CM for 48 hours in SF/Gln Free media. Graphs show quantification of ELISAs performed to detect the amount of GM-CSF, IL-6, IL-15, or TGF-β present in the CM of CON CAFs and VGlut1 KD CAFs. **D.** GS inhibited CAFs (MSO, 0, 0.1, 0.5, 1, 2.5 and 5 mM) were grown in 3D and allowed to generate CM for 48 hours in SF/Gln free media. Graphs show quantification of ELISAs of the indicated cytokines. * compared to CAFs treated with 0 mM MSO. **E.** CON RFP^+ CON or NGL-1 KO PDACc ($2x10^4$) were co-cultured with CON, NetG1 KO, or VGlut1 KD CAFs ($2x10^4$) and IL-2 preactivated NK-92 cells ($8x10^4$) for 48 hours in 3D and PDACc survival was measured. * compared to CON PDACc/CON CAF with NK cells. **F.** CON RFP^+ CON or NGL-1 KO PDACc ($2x10^4$) were co-cultured with vehicle (water) or MSO (1 mM) 24 hour pre-treated CON or NetG1 KO CAFs ($2x10^4$), in the presence of active NK-92 cells (IL-2 preactivated), and PDACc cell survival was assessed 48 hours later. In **(E+F)**, PDACc alone with and without active NK cells were used as controls. * compared to CON PDACc/CON CAF with NK cells. One-Way ANOVA, Dunnett's multiple comparison test. *p<0.05, **p<0.01, ****p<0.0001.

Figure 7. *NGL-1 KO in murine PDAC cells stunts tumorigenesis in an orthotopic murine model*. **A.** SMI was conducted on murine pancreatic tissue from wild type C57BL/B6 (normal) or KC mice (12 weeks or 16 weeks old). **(TOP Panel)** Epithelium (purple), stroma (cyan), and nuclei (yellow) were labeled and used as "masks" to query stromal (i.e., $cyan^+/purple^-$ pixel areas shown in **BOTTOM Insert** and marked by cyan square) expression of NetG1 (white, **BOTTOM Panel**). Representative scale bars are shown**. B.** Representative western blot of NGL-1 in two different murine PDAC cell line clones derived from KPC mice (KPC4B and KPC3). H3 was used as a loading control. Note the time for orthotopically injected tumor progression in weeks listed above the lanes. **C.** C57BL/6 mice were injected orthotopically with CON or NGL-1 KO KPC3 cells (10^6) and were sacrificed 3.5 weeks later. Graph depicting quantification of the weight of pancreata from each mouse group. Red numbers above the bars represent tumor incidence over total mice for each group. Images below display representative pancreata from each group. **D.**

bioRxiv preprint doi: https://doi.org/10.1101/330209; this version posted March 8, 2019. The copyright holder for this preprint (which was not certified by peer review) is the author/funder, who has granted bioRxiv a license to display the preprint in perpetuity. It is made available under aCC-BY-NC-ND 4.0 International license.

Representative MRI images for pancreata injected with CON or NGL-1 KO cells, taken at 1, 2, and 3 weeks after injection. Yellow outline marks the pancreas in each image. **E. (LEFT)** Representative images of Ki67 (red) and TUNEL (green) staining of tumors that developed from mice injected with CON KPC3 or NGL-1 KO KPC3 cells. Nuclei is stained by DAPI (blue). Scale bar is 50 µm**. (RIGHT)** Quantification of Ki67 or TUNEL staining (integrated intensity) normalized to nuclei, relative to the control PDAC group. Each dot represents the quantification of Ki67 or TUNNEL image from a single image. N= 7 CON and 6 pooled KO tumors. One-Way ANOVA, Dunnett's multiple comparison test (**C.**) or T-Test (**E.**). *p<0.05, **p<0.01, ****p<0.0001.

Figure 8. *RNAseq analysis comparing CON CAFs to NetG1 KO CAFs reveals a normalization of CAF function upon NetG1 deletion.* **A.** Heatmap showing differentially expressed genes ($p < 0.001$) in NetG1 KO CAFs with genes increased (red) and decreased (blue) expression levels. Over-represented biological process or a pathway among these genes are shown. **B and C** show GSEA enrichment plots for positive and negative enrichment respectively in NetG1 KO CAFs. **D.** Elevated levels of NetG1, VGlut1, GS, pFAK, and active-$\alpha_5\beta_1$ integrin are all representative traits indicative of C2 CAFs.. High NetG1 expression allows C2 CAFs to interact with PDAC cells that express the NetG1 binding partner, NGL-1 (red receptors). These interactions facilitate heterotypic cell-cell contacts that mediate the transfer of nutrients (orange circles; Glu/Gln metabolism) to PDAC cells, increasing their survival in the nutrient depleted tumor microenvironment. NetG1$^+$ CAFs intrinsically produce elevated levels of immunosuppressive factors (green boxes), which render NK cells unable to eliminate PDAC cells. Moreover, NetG1$^+$ CAFs have increased VGlut1 (blue squares) and GS activity, which also contributes to enhanced pro-tumor metabolic and immunosuppressive functions. Thus, NetG1 controls CAF cell autonomous and reciprocal pro-tumorigenic functions.

Supplemental Figure Legends

Fig S1. Related to Figure 2. *Expression of NetG1 and its ligand NGL-1 in cancers*. **A.** Plots show the mRNA expression of NetG1 (*NTNG1*) and its ligand NGL-1 (*LRRC4C*) in various cancers. The expression data (Z-scores of RNASeq V2 RSEM expression data) are shows as box plots where each dot represent a patient with colors describing the molecular alterations within that patient**. B-D.** (**LEFT**) Kaplan- Meier curves for overall survival based on 5 different subtypes of PDAC cases as described by Puleo *et al.* (**B)** et al. (**C**) and TCGA (**D**) are shown. (**RIGHT**) Box plots show the expression of *NTNG1* and *LRRC4C* in PDAC tumors for various subtypes across Puleo *et al.* (**B)** Moffitt *et al*. (**C**) and TCGA (**D**) studies. Significance of differences in expression of these two genes across subtypes is estimated using Kruskal-Wallis test.

Figure S2. Related to Figure 2. *Loss of NetG1 in CAFs results in a decrease in expression of proteins associated with tumor promoting properties of CAFs*. **A.** Representative western blot demonstrating NetG1 expression in 2D vs. 3D culturing conditions. Note the significantly higher expression of NetG1 in 3D. GAPDH served as a loading control. **B.** Representative mRNA expression of NetG1 in PSCs and CAFs from a single patient cultured in 3D. **C.** Representative western blot of NetG1 illustrating consistent expression of the protein throughout 6 days of 3D ECM production. H3 was used as a loading control. **D.** Generation of two human NetG1 KO CAF lines, using CRISPR/Cas9, as shown in the western blot. H3 was used as a loading control. Cell line containing vector targeting GFP was used as control**. E.** ECM fiber orientation, as indicated by fibronectin IF and pseudo-colored to highlight fiber orientation using the OrientationJ plugin in

bioRxiv preprint doi: https://doi.org/10.1101/330209; this version posted March 8, 2019. The copyright holder for this preprint (which was not certified by peer review) is the author/funder, who has granted bioRxiv a license to display the preprint in perpetuity. It is made available under aCC-BY-NC-ND 4.0 International license.

ImageJ. Color bar: color coded angle orientation showing green color used for normalized mode angle fibers. FN fibers within 15 degrees of the mode angle were scored as an indicator of ECM orientation and were graphed on the right. **F. (LEFT)** Representative images of α-smooth muscle actin (α-SMA) IF. **(RIGHT)** Quantification (intensity) displayed in the graph. Scale bar is 50 µm and serves for both (**E**) and (**F**). **G.** Quantification of active integrin $\alpha_5\beta_1$; IF intensity, detected using the SNAKA51 antibody in CON or NetG1 KO CAFs. **H.** Quantification of phospho-FAK^{397} (pFAK) IF intensity in CON or NetG1 KO CAFs. **I.** Validation of CRISPR/Cas9 mediated NGL-1 KO in PDACc cells, as shown in the representative western blot. GAPDH was used as a loading control. Cell lines containing vector targeting GFP were used as control. **J.** Quantification of the relative Ki67 staining in CON and NGL-1 KO PDACc grown in 3D, in CON CAF generated ECMs. **K.** Validation of CRISPR/Cas9 mediated KO of NGL-1 in PANC-1 cells, as shown in the representative western blot. H3 was used as a loading control. Cell lines containing vector targeting GFP were used as control.. T-test, ** $p< 0.01$; *** $p< 0.001$; **** $p< 0.0001$.

Figure S3. Related to Figure 3. *NetG1 promotes heterotypic cell interactions and material transfer from CAFs to PDAC cells.* A cell engagement assay was undertaken by co-culturing $2x10^4$ CON or NGL-1 KO PDACc (RFP^+) in 3D with $2x10^4$ CON or NetG1 KO CAFs (GFP^+) for 24 hours, and areas of cell engagement were measured. **A.** Example of the type of areas analyzed in the cell engagement assay. Note the yellow area in the top panel (representing the engagement area), with the zoomed in region of the yellow in the panel below. Scale bar is 10 µm. **B.** Representative images of the areas of cell engagement for each co-culture condition, over the time span of the assay. Scale bar is 10 µm. **C.** Quantification of cell engagement areas during 10 hours of engagement. **D. 3D** Cell movement, following cells invading through CAF generated ECMs was performed by co-culturing RFP^+ CON or NGL-1 KO PDACc ($2x10^4$) with GFP^+ CON or NetG1 KO CAFs ($2x10^4$) for 24 hours; time lapse videos measured PDACc cell movement over that timespan. Shown are all motility tracks of PDACc, moving through ECMs, that were acquired from each co-culture experimental condition. **E.** Velocity (µm/hour) of PDACc from (**D**). * compared to CON PDACc/ CON CAF group. **F.** Representative images from a 36 hour 3D co-culture of GFP labeled CON or NetG1 KO CAFs ($2x10^4$) with RFP labeled CON or NGL-1 KO PDACc ($2x10^4$), in SF media. Note the yellow color inside of RFP^+ PDACc in the CON/CON condition, indicative of PDACc intracellular GFP, acquired from CAFs (Merged). Scale bar is 50 µm**. G.** Quantification of the amount of GFP^+ PDACc cells, calculated as integrated GFP fluorescence intensity, from the 36 hour material transfer assay in (**F**), relative to the CON PDACc /CON CAF co-culture condition. Each dot represents the quantification of one image. N = 3 independent experiments with a minimum of 7 images per condition. Note how loss of stromal NetG1 or tumoral NGL-1 sufficed to prevent CAF material transfer into PDAC cells. One-way ANOVA, Dunnett's multiple comparison test ** $p< 0.01$; *** $p< 0.001$; **** $p< 0.0001$.

Fig S5. Related to Figure 4. *NetG1 KD CAFs generated with CRISPRi phenocopy NetG1 KO CAFs generated with CRISPR.* **A.** Representative western blots displaying the expression levels of NetG1, VGlut1, GLS, GS in PSCs, CON CAFs, and NetG1 KD CAFs (KD1 and KD2). Note the effective knockdown of NetG1, as well as downregulation of VGlut1 and GS expression, similar to NetG1 KO CAFs. **B.** PDAC cell survival was determined after RFP^+ CON or NGL-1 KO PDACc ($2x10^4$) were cultured with CON or NetG1 KD CAFs for 96 hours in SF/Gln free media. Note that the NetG1 KD CAFs functionally behave similarly to the NetG1 KO CAFs. **C.** Representative western blots demonstrating changes in VGlut1, NetG1, GLS, and GS protein expression in CAFs

bioRxiv preprint doi: https://doi.org/10.1101/330209; this version posted March 8, 2019. The copyright holder for this preprint (which was not certified by peer review) is the author/funder, who has granted bioRxiv a license to display the preprint in perpetuity. It is made available under aCC-BY-NC-ND 4.0 International license.

treated for 24 hours in 3D with increasing concentrations of MSO (GS inhibitor). For all blots, GAPDH served as the loading control.

Fig S6. Related to Figure 5. *NetG1 KD CAFs also produce less cytokines compared to CON CAFs.* CON CAFs or NetG1 KD CAFs, produced with CRISPRi, were allowed to produce CM for 48 hours in 3D. The CM was then subjected to ELISA analysis for the quantification of the following cytokines: GM-CSF, IL-6, IL-8, TGF-β, and IL-15. Note that the NetG1 KD CAFs produce similar fold changes in cytokine production as the NetG1 KO CAFs do compared to their CON CAF counterparts. One-way ANOVA, Dunnett's multiple comparison test, * $p< 0.05$; ** $p< 0.01$; *** $p< 0.001$; **** $p< 0.0001$.

Fig S7. Related to Figure 5. *NetG1 KO CAFs support NK cell killing of PDAC cells in several 2D in vitro models*. **A.** Representative images of PDAC cell survival. RFP^+ CON or NGL-1 KO PDACc ($2x10^4$) were co-cultured in 3D with GFP^+ CON or NetG1 KO CAFs ($2x10^4$) in the presence of active NK-92 cells ($8x10^4$) **(TOP panel)** or without CAFs in the presence of resting or active NK-92 cells ($8x10^4$) **(BOTTOM panel)** for 48 hours. Scale bar is 500 µm**. B.** Quantification of **(A); BOTTOM** panel. * compared to CON with active NK cells. **C. (LEFT)** 2D NK cell assay: RFP^+ CON or NGL-1 KO PDACc were co-cultured 1:1 ($2x10^4$ cells) with resting or activated NK-92 cells ($8x10^4$) alone, or with GFP^+ CON and NetG1 KO CAFs for 8 hours. PDACc cell survival was assessed**.** Representative images of PDACc (red) and CAFs (green) from the various assay conditions. White insert in the top left-hand corner shows dead cell channel, marked by Sytox blue. **(RIGHT)** Quantification of the 2D NK cell killing assay. * compared to CON PDACc/CON CAF cultured with active NK-92 cells. **D.** The same NK cell assay performed in (**C**), but with PANC-1 cells instead of PDACc cells. * compared to CON PANC-1/CON CAF cultured with active NK-92 cells. **E**. Quantification of the co-culture conditions with resting NK cells from (**C**). * compared to CON PDACc/CON CAF cultured with resting NK-92 cells. **F.** Quantification of CAF control conditions from the experiment in (**C**). **G.** The NK cell killing assay was performed as in (**C**), but with the indicated ratios of PDACc:CAF (5:1, 3:1, 1:3). * compared to CON PDACc/CON CAF cultured with active NK-92 cells, for each ratio. Graphs show mean survival and standard errors of the three independent experiments. One-way ANOVA, Dunnett's multiple comparison test, * $p< 0.05$; ** $p< 0.01$; *** $p< 0.001$; **** $p< 0.0001$.

Fig S8. Related to Figure 7. *NGL-1 knockout in murine KPC PDAC cells is sufficient to limit* in vivo *tumorigenesis despite immune competency.* **A.** Western blot of NGL-1, demonstrating knockout in two independent clones of KPC3 murine PDAC cells. H3 was used as a loading control. **B.** Quantification of the % area that tumor cells occupy in the pancreata of mice injected with CON KPC3 or NGL-1 KO KPC3 cells (pooled KO mice together). **C.** Same quantification as in (**B**), but only considering the pancreata that had histological evidence of tumor cells (CON, N = 7; NGL-1 KO, N = 6). **D.** Representative images of the entire pancreas of representative mice quantified in (**C**) Scale bar is 5 mm**. E.** Representative images of the pancreatic tissue from CON or NGL-1 KO injected mice, demonstrating morphology indicative of differentiation status of tumor cells. Scale bar is 100 µm**. F.** Quantification of the differentiation status of tumors within the pancreatic tissue that formed tumors (CON, N = 7; KO, N = 6), as measured by % cells that were classified as well differentiated, moderately differentiated, or poorly differentiated by a blinded pathologist. **G**. B6, SCID (lacks T and B cells), or NSG (lacks T, B, and NK cells) mice were injected with 10^6 CON KPC3 or NGL-1 KO #2 cells. Animals were sacrificed after 3.5 weeks and

bioRxiv preprint doi: https://doi.org/10.1101/330209; this version posted March 8, 2019. The copyright holder for this preprint (which was not certified by peer review) is the author/funder, who has granted bioRxiv a license to display the preprint in perpetuity. It is made available under aCC-BY-NC-ND 4.0 International license.

pancreas weight (mg) was assessed. (n=5, for each cell type, in each background). T-Test, * $p< 0.05$; *** $p< 0.001$; **** $p< 0.0001$.

bioRxiv preprint doi: https://doi.org/10.1101/330209; this version posted March 8, 2019. The copyright holder for this preprint (which was not certified by peer review) is the author/funder, who has granted bioRxiv a license to display the preprint in perpetuity. It is made available under a CC-BY-NC-ND 4.0 International license.

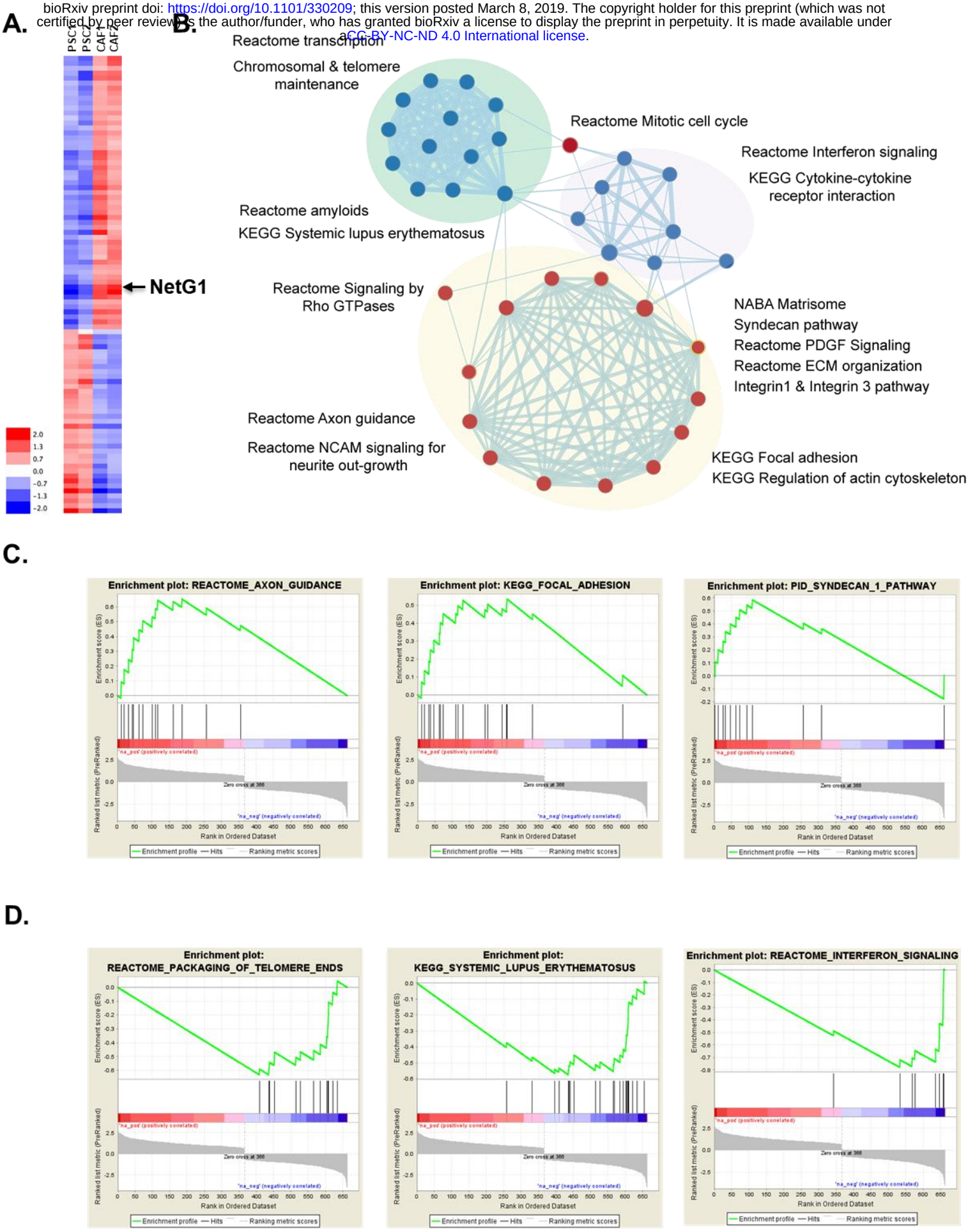

Figure 1

bioRxiv preprint doi: https://doi.org/10.1101/330209; this version posted March 8, 2019. The copyright holder for this preprint (which was not certified by peer review) is the author/funder, who has granted bioRxiv a license to display the preprint in perpetuity. It is made available under aCC-BY-NC-ND 4.0 International license.

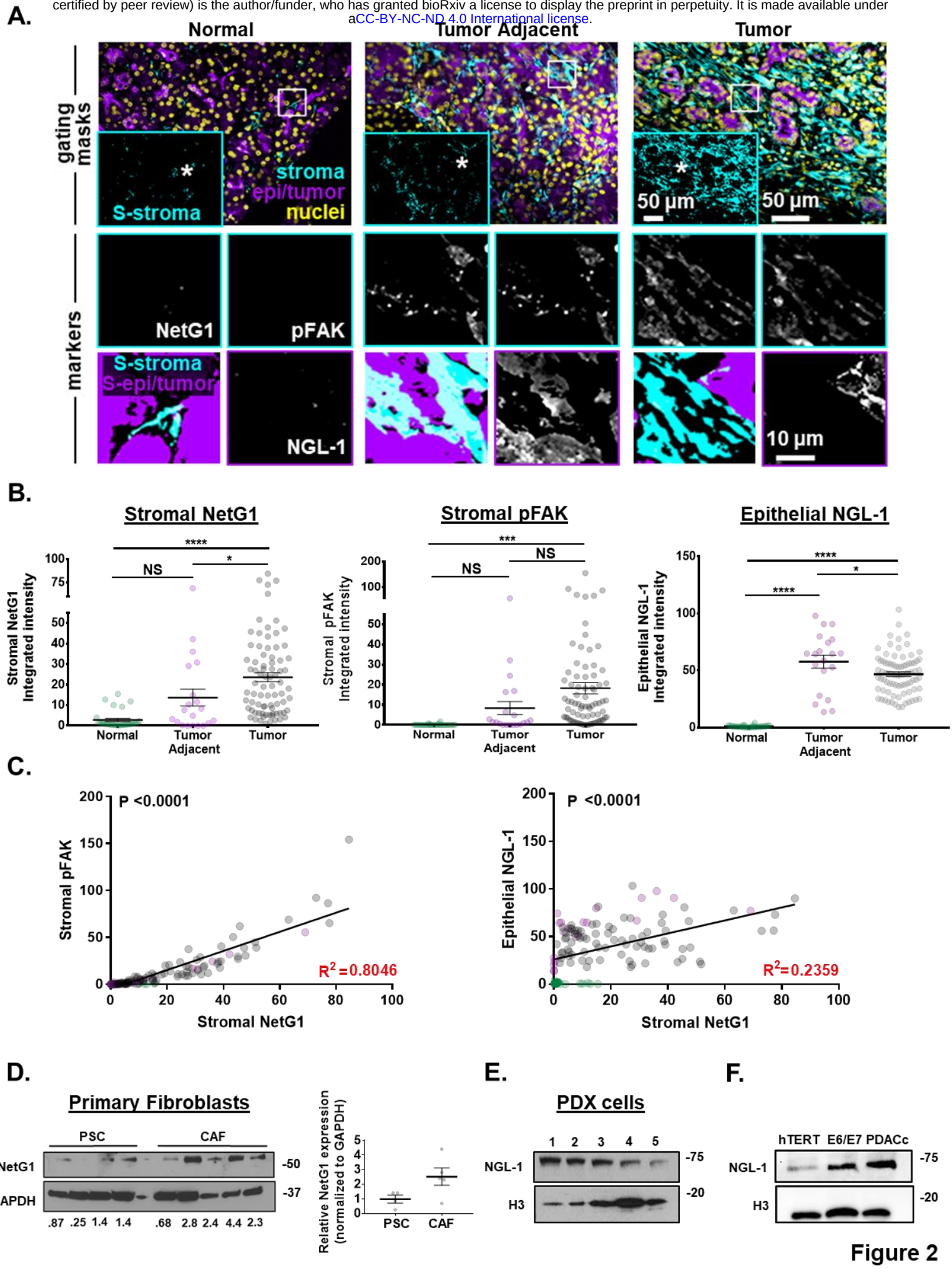

Figure 2

bioRxiv preprint doi: https://doi.org/10.1101/330209, this version posted March 8, 2019. The copyright holder for this preprint (which was not certified by peer review) is the author/funder, who has granted bioRxiv a license to display the preprint in perpetuity. It is made available under aCC-BY-NC-ND 4.0 International license.

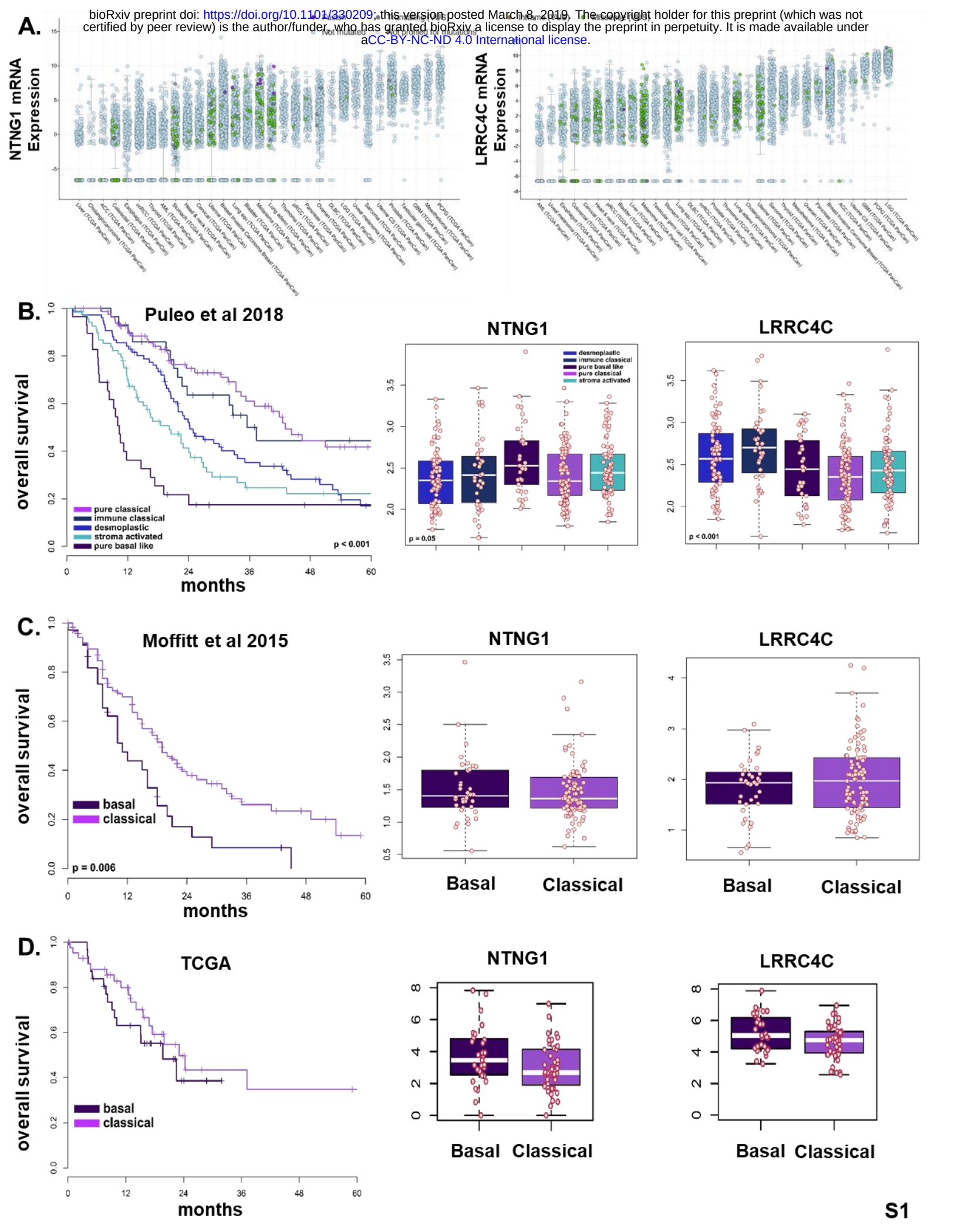

S1

bioRxiv preprint doi: https://doi.org/10.1101/330209; this version posted March 8, 2019. The copyright holder for this preprint (which was not certified by peer review) is the author/funder, who has granted bioRxiv a license to display the preprint in perpetuity. It is made available under aCC-BY-NC-ND 4.0 International license.

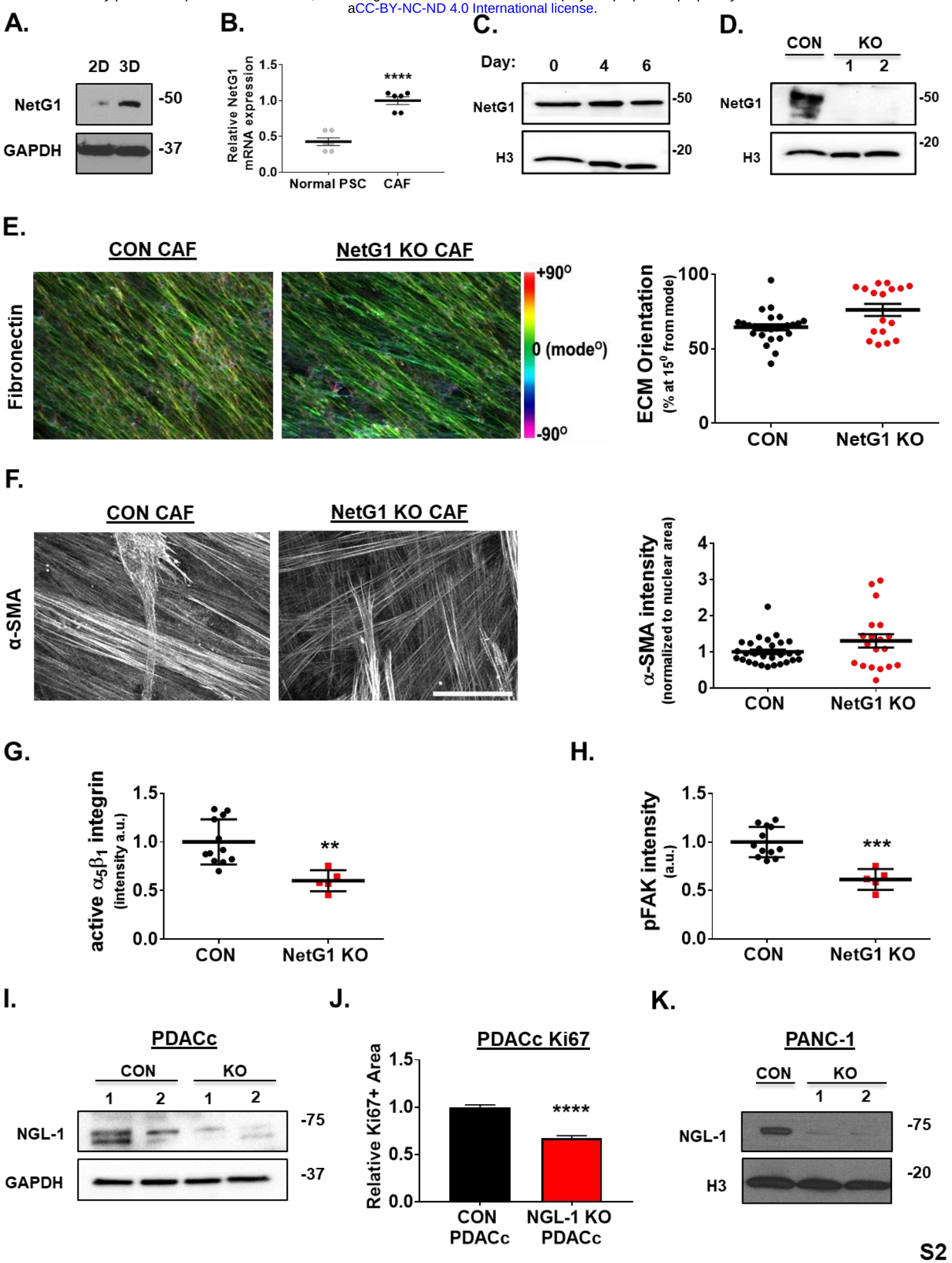

S2

bioRxiv preprint doi: https://doi.org/10.1101/330209; this version posted March 8, 2019. The copyright holder for this preprint (which was not certified by peer review) is the author/funder, who has granted bioRxiv a license to display the preprint in perpetuity. It is made available under aCC-BY-NC-ND 4.0 International license.

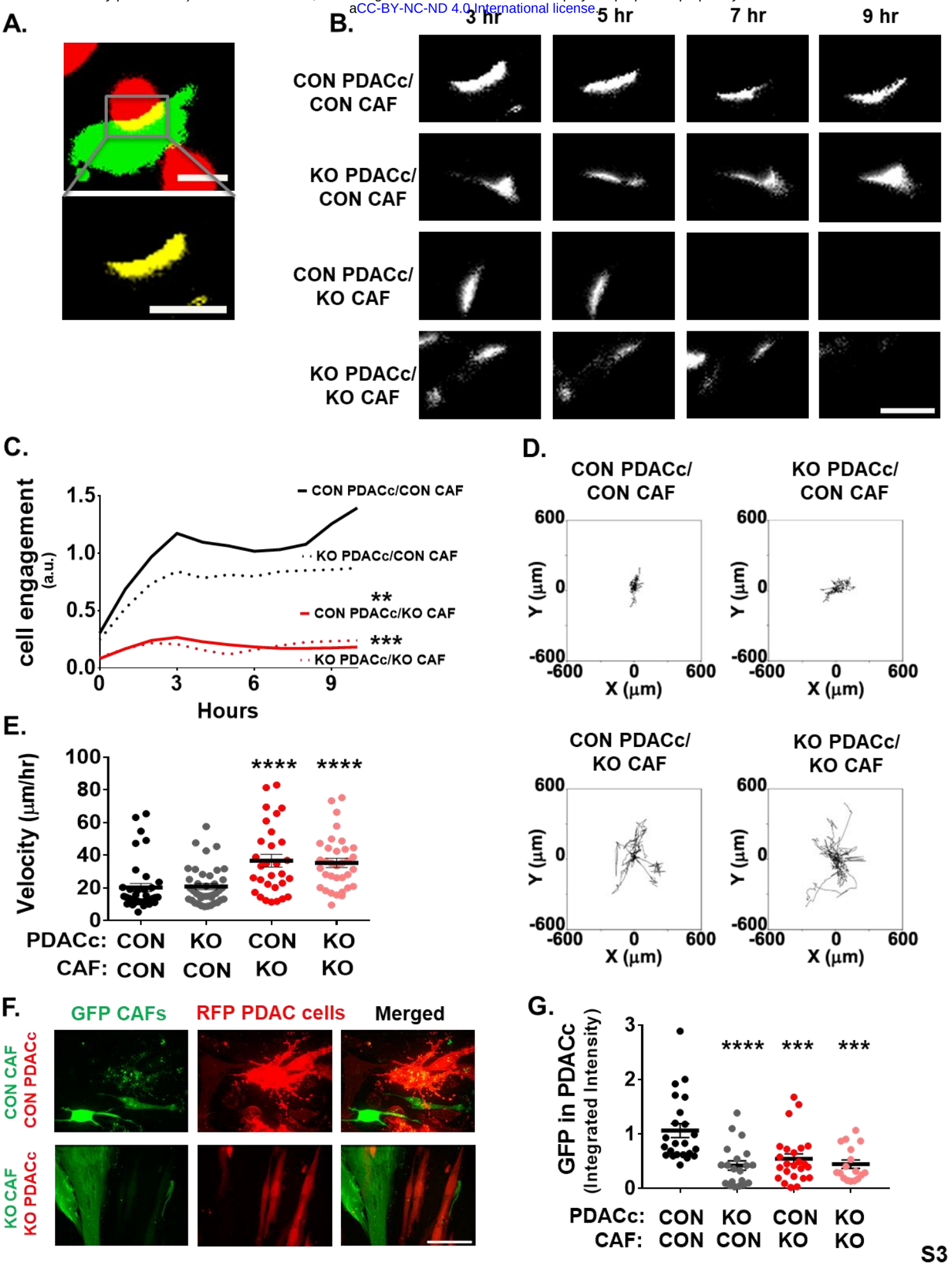

bioRxiv preprint doi: https://doi.org/10.1101/330209; this version posted March 8, 2019. The copyright holder for this preprint (which was not certified by peer review) is the author/funder, who has granted bioRxiv a license to display the preprint in perpetuity. It is made available under aCC-BY-NC-ND 4.0 International License.

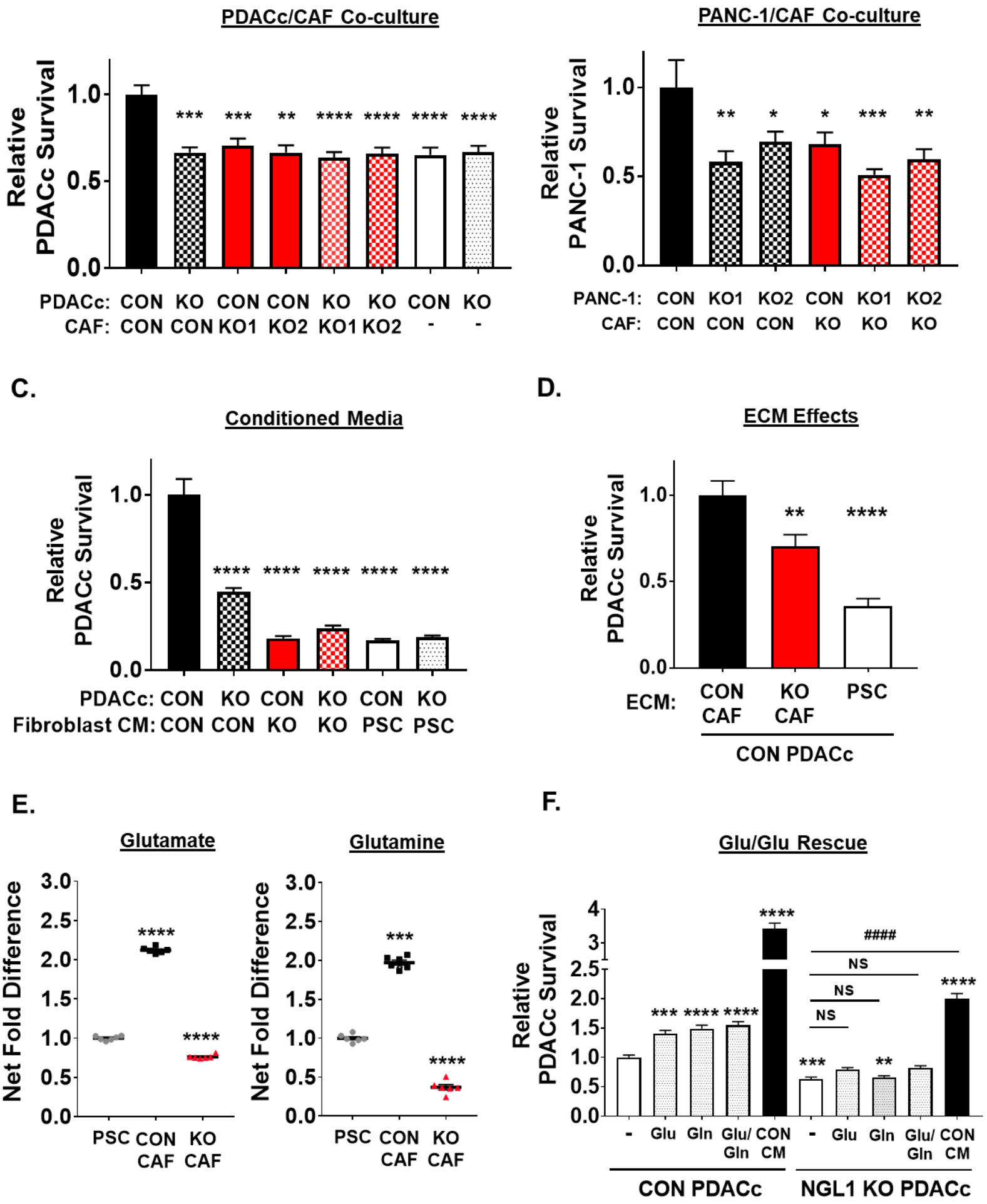

Figure 3

bioRxiv preprint doi: https://doi.org/10.1101/330209; this version posted March 8, 2019. The copyright holder for this preprint (which was not certified by peer review) is the author/funder, who has granted bioRxiv a license to display the preprint in perpetuity. It is made available under a CC-BY-NC-ND 4.0 International license.

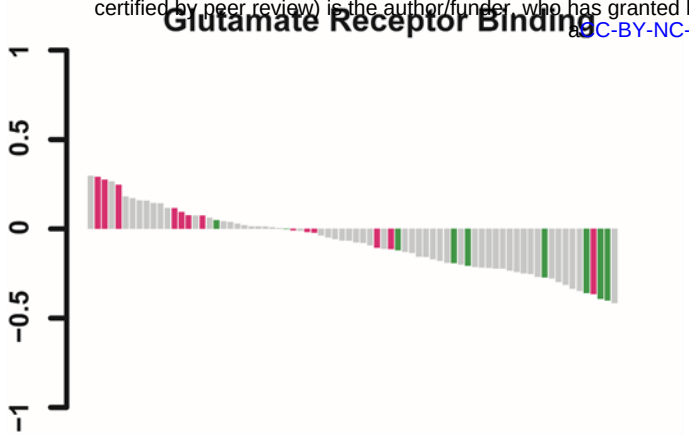

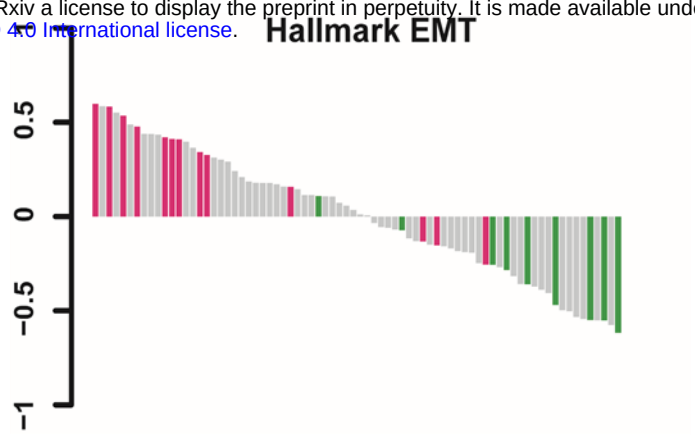

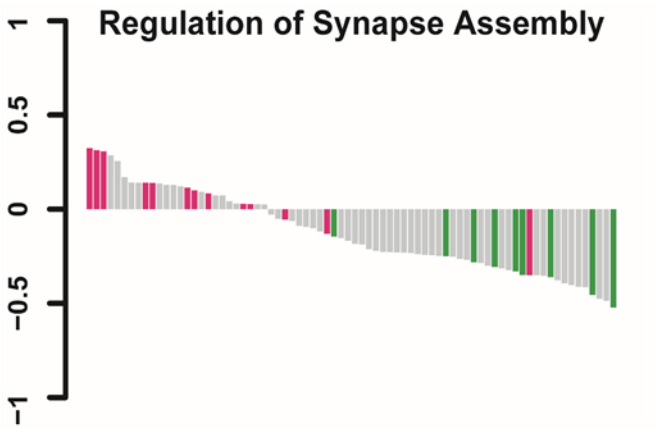

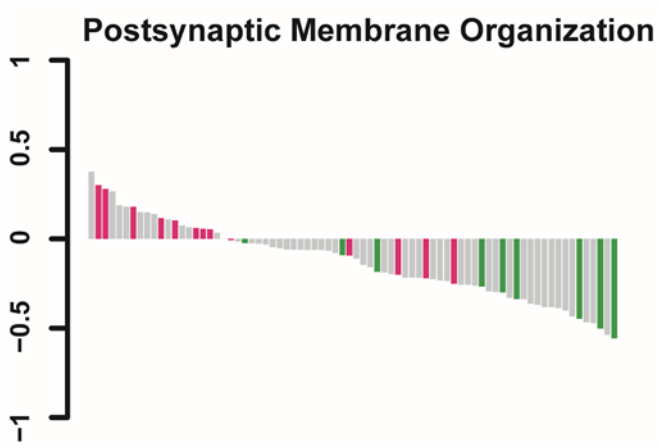

bioRxiv preprint doi: https://doi.org/10.1101/330209; this version posted March 8, 2019. The copyright holder for this preprint (which was not certified by peer review) is the author/funder, who has granted bioRxiv a license to display the preprint in perpetuity. It is made available under aCC-BY-NC-ND 4.0 International license.

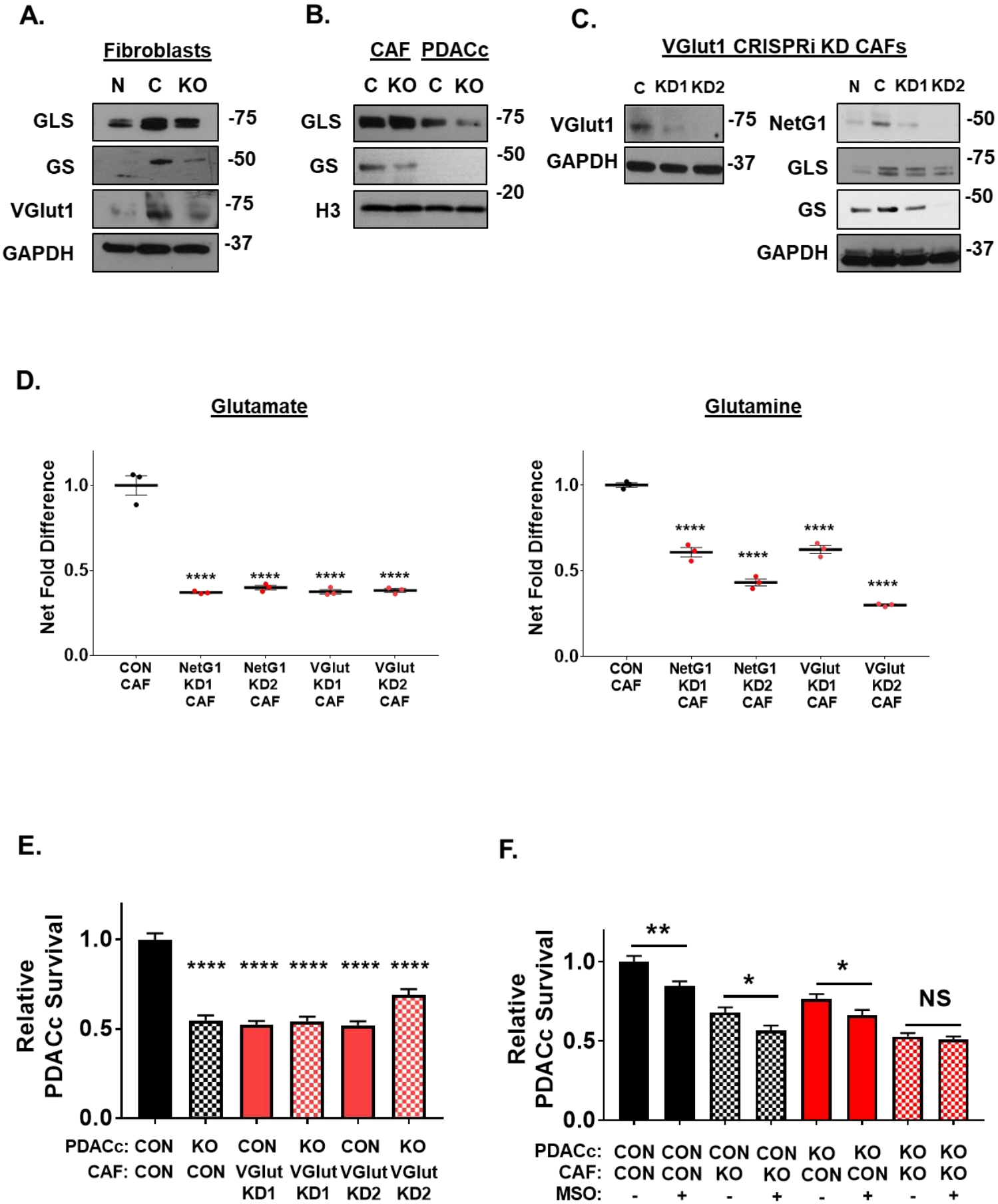

Figure 4

bioRxiv preprint doi: https://doi.org/10.1101/330209; this version posted March 8, 2019. The copyright holder for this preprint (which was not certified by peer review) is the author/funder, who has granted bioRxiv a license to display the preprint in perpetuity. It is made available under aCC-BY-NC-ND 4.0 International license.

A.

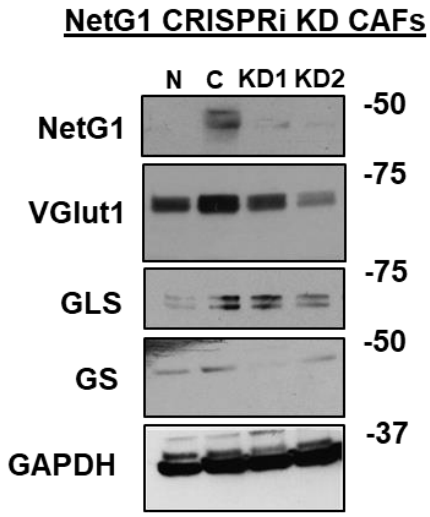

B.

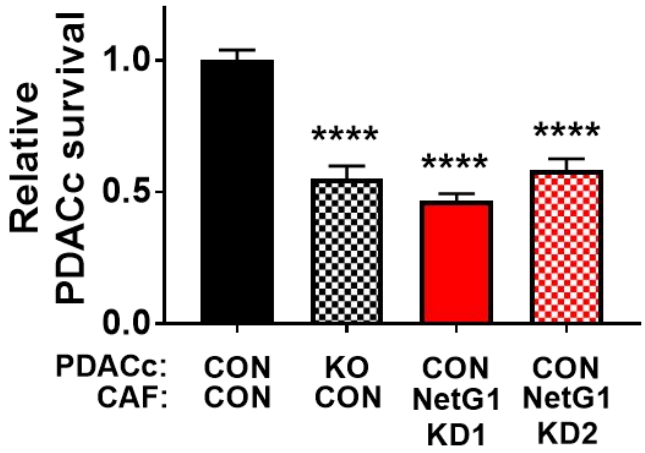

C.

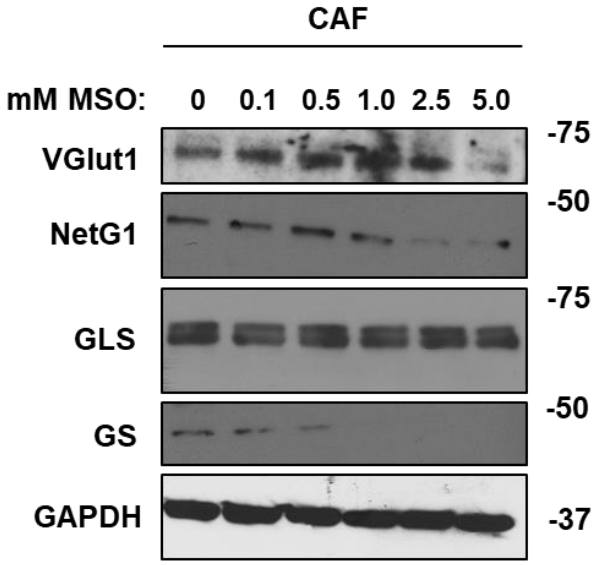

bioRxiv preprint doi: https://doi.org/10.1101/330209; this version posted March 8, 2019. The copyright holder for this preprint (which was not certified by peer review) is the author/funder, who has granted bioRxiv a license to display the preprint in perpetuity. It is made available under aCC-BY-NC-ND 4.0 International license.

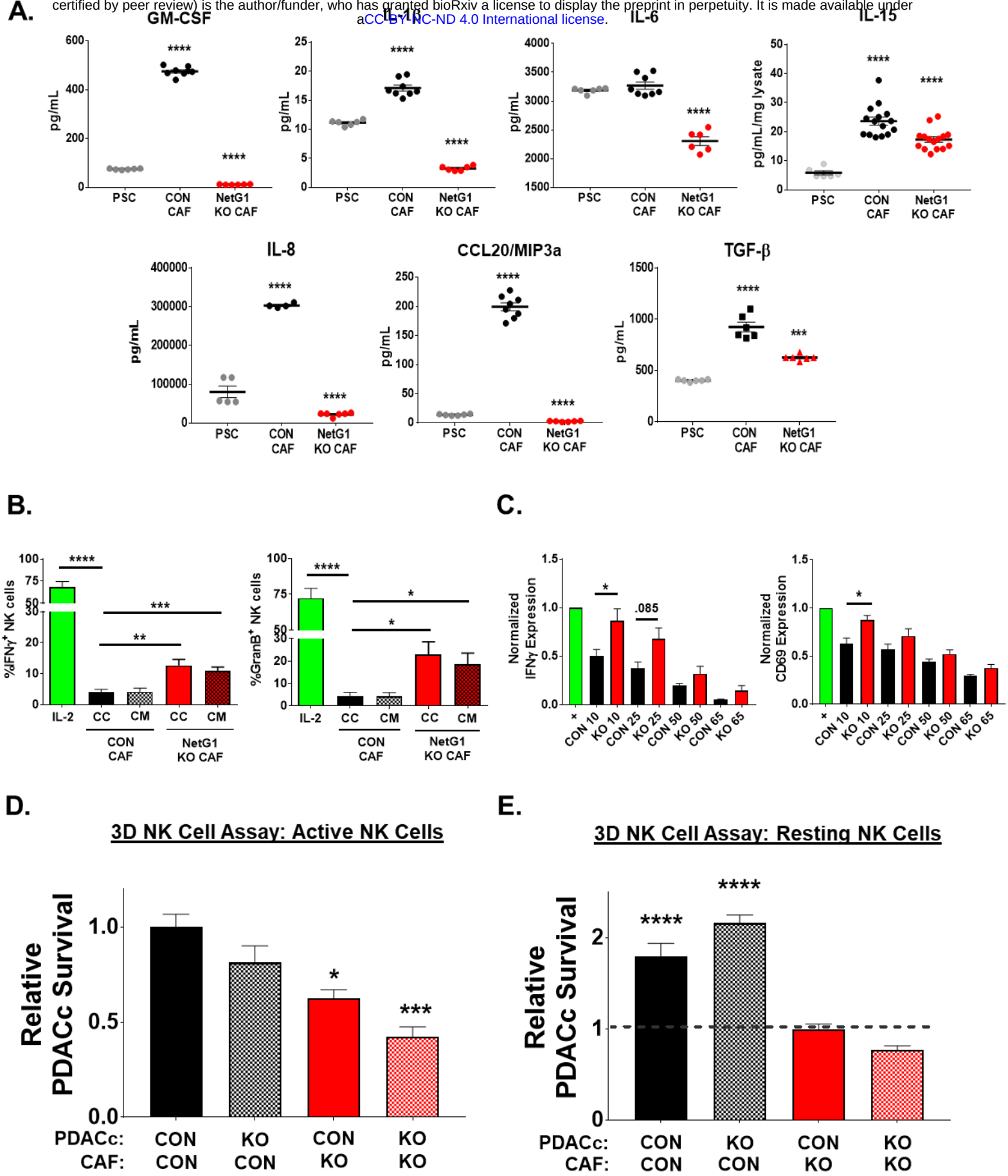

Figure 5

bioRxiv preprint doi: https://doi.org/10.1101/330209; this version posted March 8, 2019. The copyright holder for this preprint (which was not certified by peer review) is the author/funder, who has granted bioRxiv a license to display the preprint in perpetuity. It is made available under aCC-BY-NC-ND 4.0 International license.

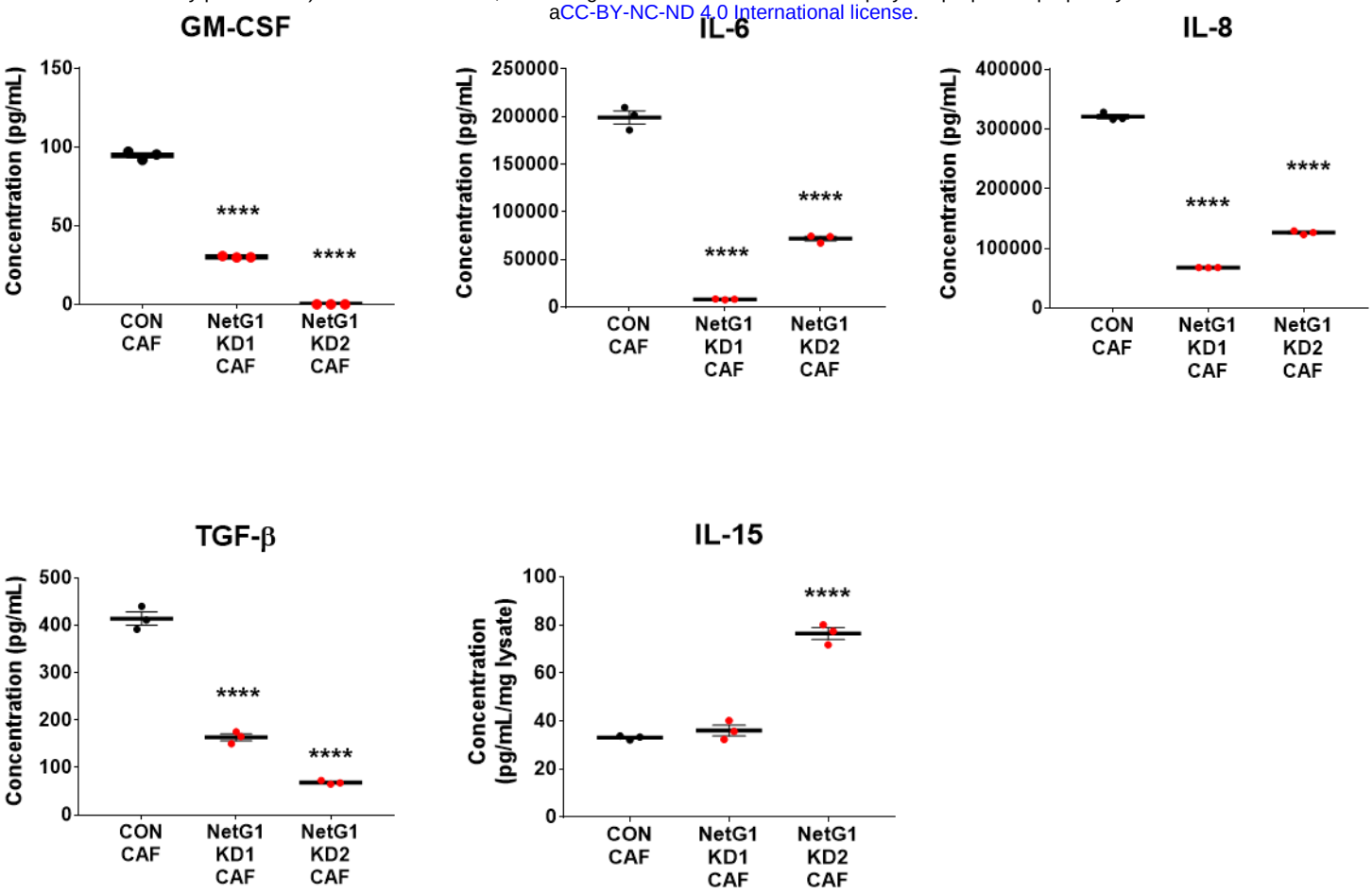

bioRxiv preprint doi: https://doi.org/10.1101/330209; this version posted March 8, 2019. The copyright holder for this preprint (which was not certified by peer review) is the author/funder, who has granted bioRxiv a license to display the preprint in perpetuity. It is made available under aCC-BY-NC-ND 4.0 International license.

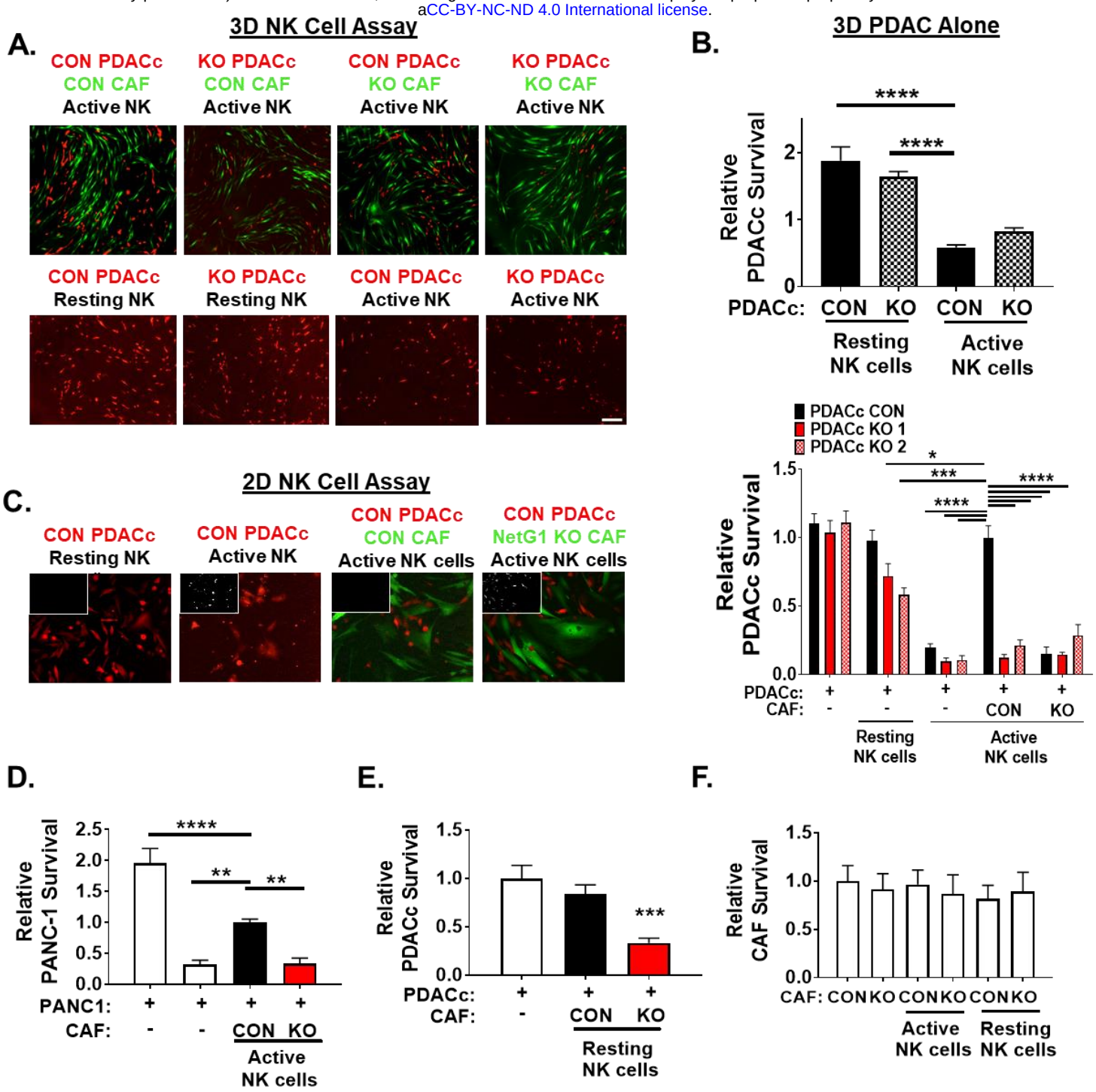

bioRxiv preprint doi: https://doi.org/10.1101/330209; this version posted March 8, 2019. The copyright holder for this preprint (which was not certified by peer review) is the author/funder, who has granted bioRxiv a license to display the preprint in perpetuity. It is made available under aCC-BY-NC-ND 4.0 International license.

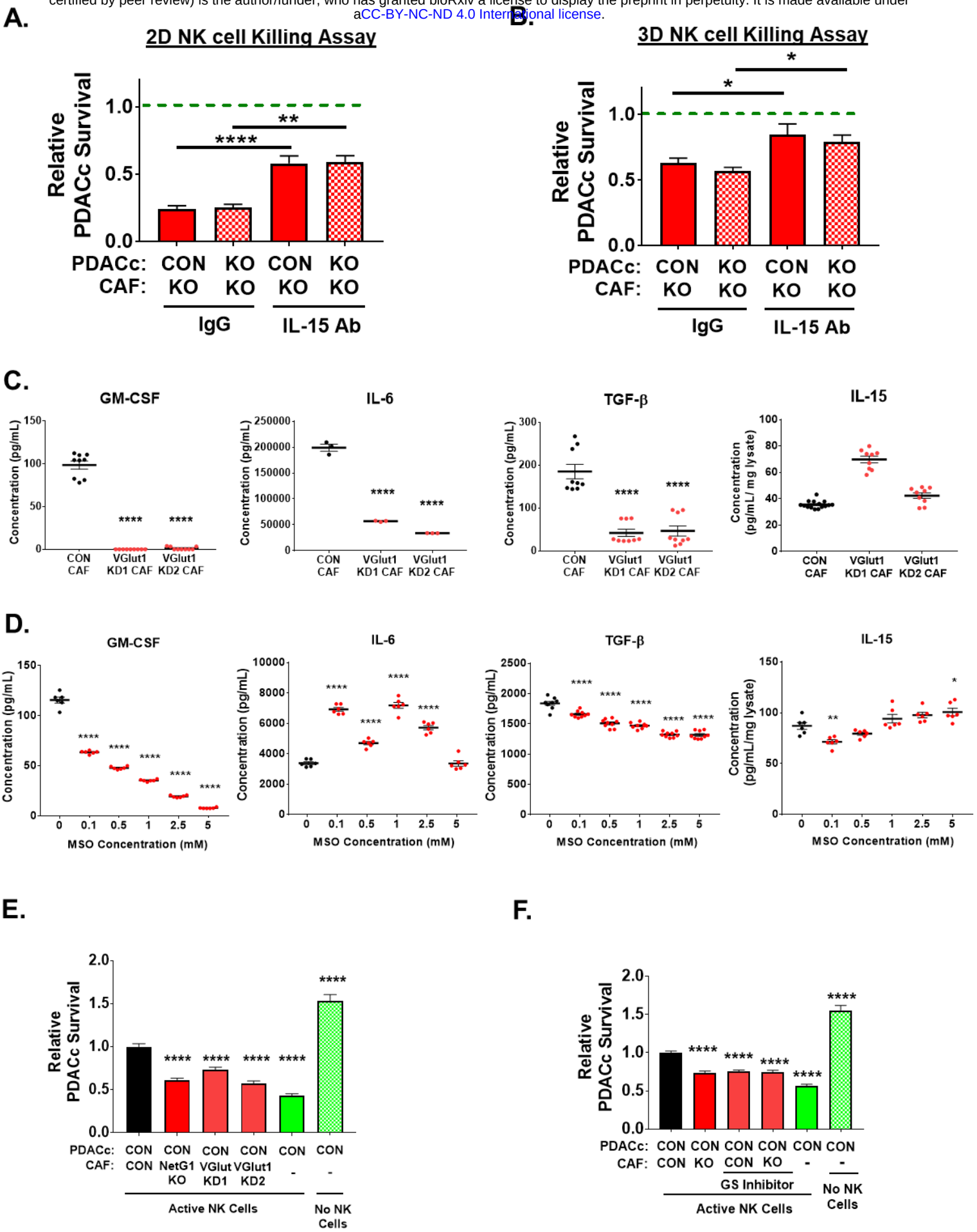

Figure 6

bioRxiv preprint doi: https://doi.org/10.1101/330209; this version posted March 8, 2019. The copyright holder for this preprint (which was not certified by peer review) is the author/funder, who has granted bioRxiv a license to display the preprint in perpetuity. It is made available under aCC-BY-NC-ND 4.0 International license.

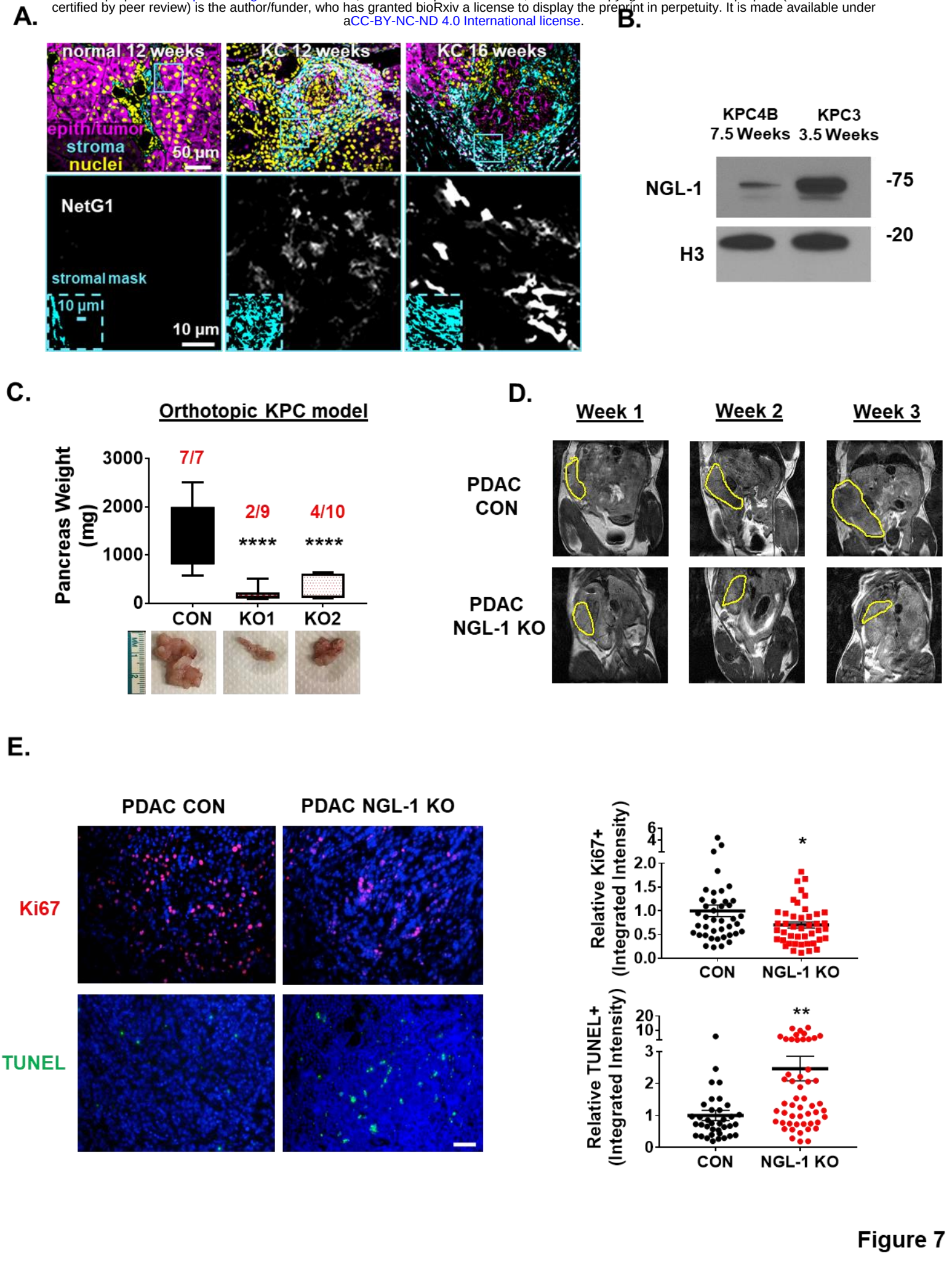

Figure 7

bioRxiv preprint doi: https://doi.org/10.1101/330209; this version posted March 8, 2019. The copyright holder for this preprint (which was not certified by peer review) is the author/funder, who has granted bioRxiv a license to display the preprint in perpetuity. It is made available under aCC-BY-NC-ND 4.0 International license.

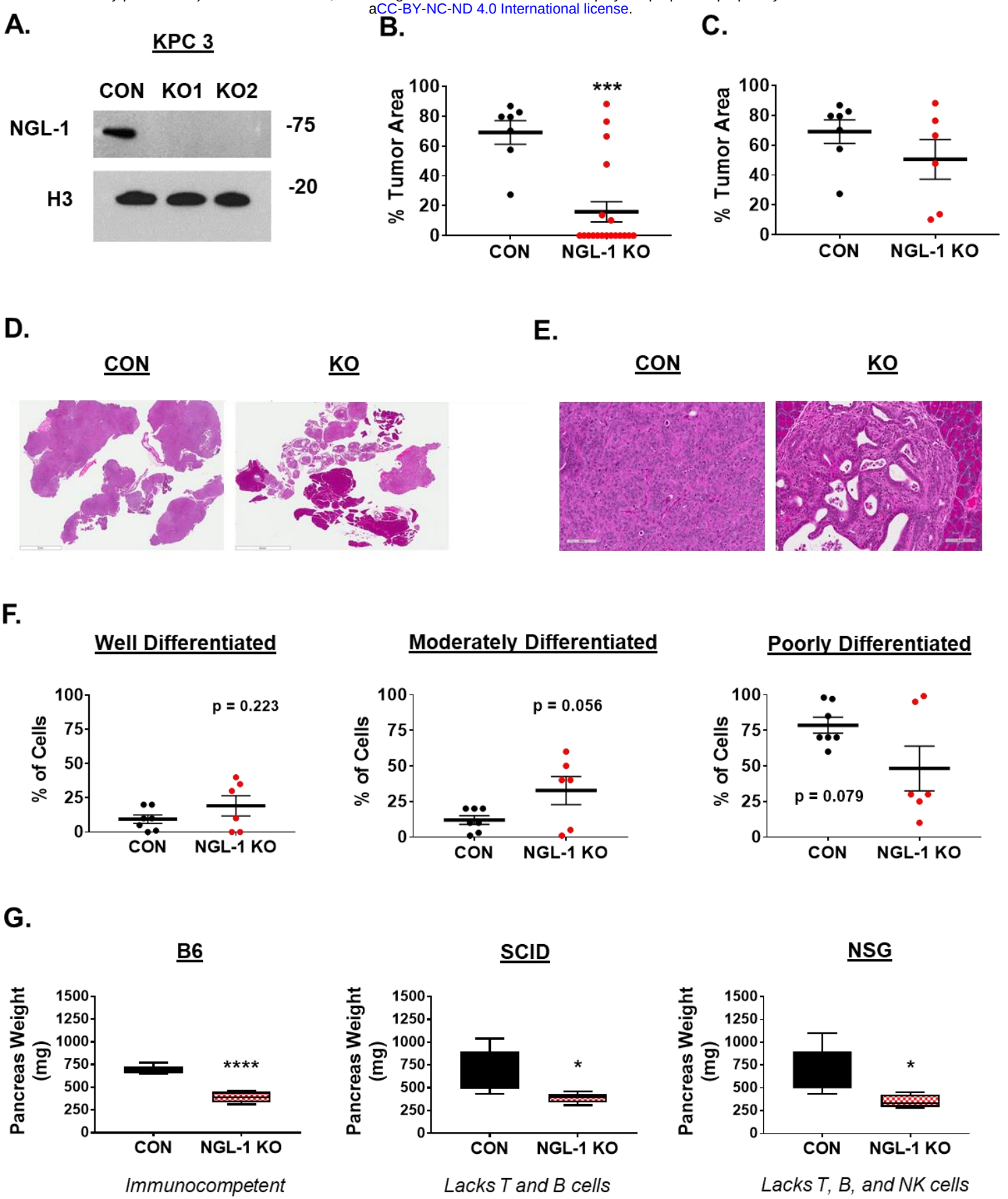

bioRxiv preprint doi: https://doi.org/10.1101/330209; this version posted March 8, 2019. The copyright holder for this preprint (which was not certified by peer review) is the author/funder, who has granted bioRxiv a license to display the preprint in perpetuity. It is made available under aCC-BY-NC-ND 4.0 International license.

A.

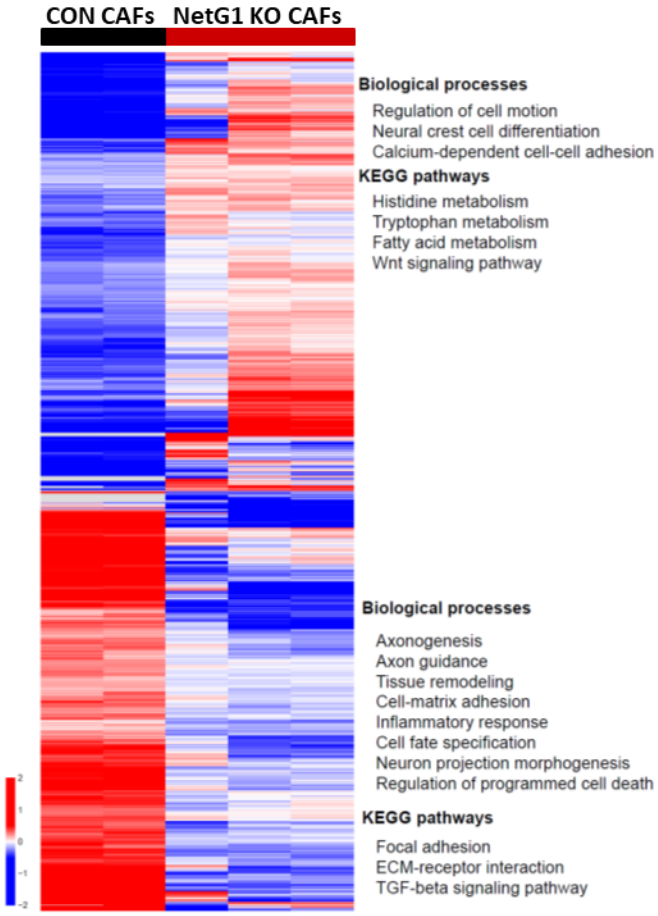

B.

C.

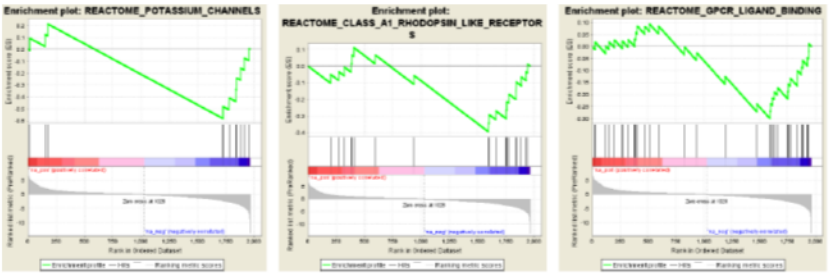

D.

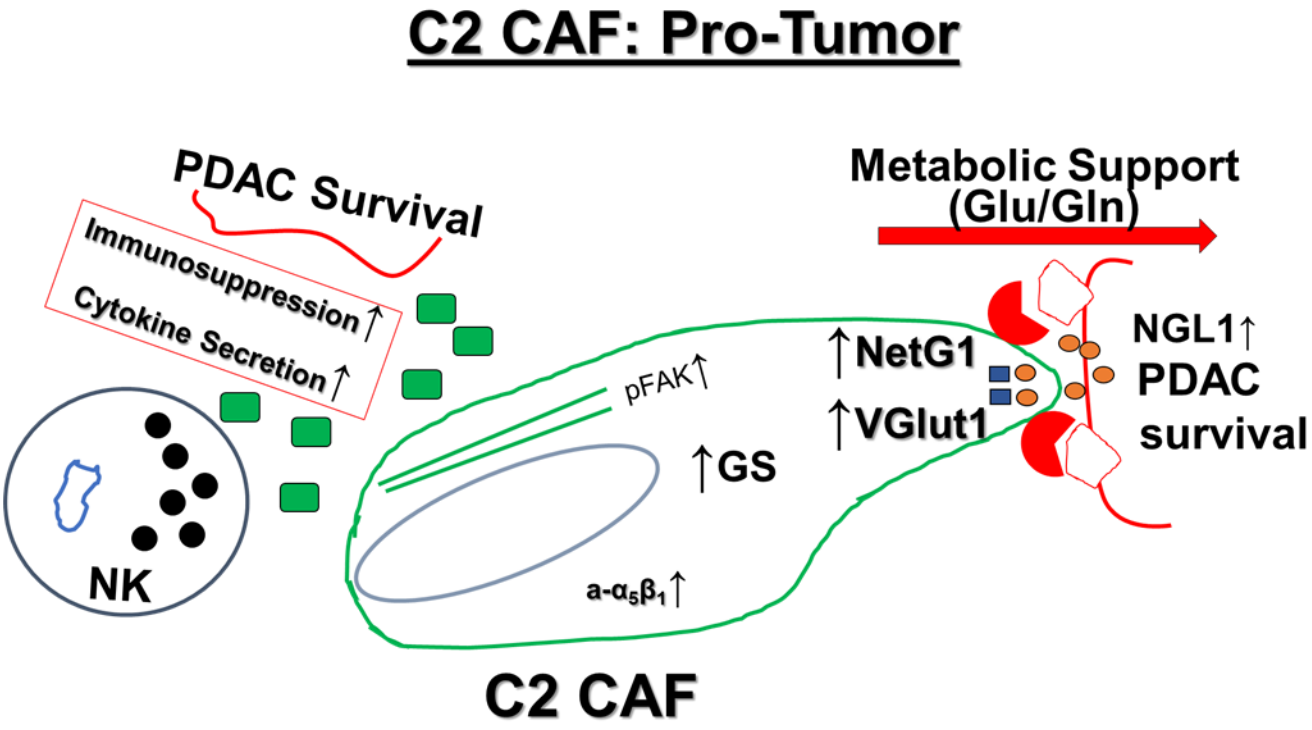

Figure 8